2nd International Symposium on

Light Alloys and Composite Materials

IMPORTANT DATES

Abstract submission deadline
01 March 2022

Announcement of Program
02 March 2022

Conference Dates
31 March - 02 April 2022

uhaks@karabuk.edu.tr
uhaks.karabuk.edu.tr

Karabuk University
Karabuk / Turkey

UHAKS'22

The Proceedings Book of 2nd International Symposium on Light Alloys and Composite Materials 31 March - 02 April 2022 Karabük University, Karabük, TURKEY.

Edited by

Prof. Dr. Bilge Demir

Assoc. Prof. Dr. Fatih Aydın

Assist. Prof. Dr. Safa Polat

Copyright

ISBN 978-605-9554-67-1

© 10 May 2022, UHAKS'22 Karabuk University
Karabuk, Turkey
https://uhaks.karabuk.edu.tr
uhaks@karabuk.edu.tr

These proceedings include the original papers submitted to UHAKS'22. It is accessed in free of charge. All scientific and linguistic responsibilities of the published articles belong to their authors.

2nd International Symposium on Light Alloys and Composite Materials

31 March - 02 April 2022
Karabük University, Karabük, TURKEY.

HONORARY COMMITTEE

Prof. Dr. Refik POLAT	Karabuk University
Prof. Dr. Mustafa YAŞAR	Karabuk University

UHAKS22' CHAIR

Prof. Dr. Bilge Demir	Karabuk University
Prof. Dr. Yavuz Sun	Karabuk University

ORGANIZATION COMMITTEE

Prof. Dr. Burak DİKİCİ,	Atatürk University
Assoc. Prof. Dr. Muhammet Emre TURAN,	Karabuk University
Assoc. Prof. Dr. Fatih AYDIN,	Karabuk University
Assoc. Prof. Dr. Nermin DEMİRKOL,	Kocaeli University
Assoc. Prof. Dr. Mevlüt GÜRBÜZ,	Ondokuz Mayıs University
Assist. Prof. Dr. Engin ÇEVİK,	Karabuk University
Assist. Prof. Dr. Safa POLAT,	Karabuk University

SCIENTIFIC COMMITTEE

Prof. Dr. Pradeep K. Rohatgi,	University of Wisconsin-Milwaukee, USA
Prof. Dr. Anton Ficai,	Politehnica University of Bucharest, Romania
Prof. Dr. Jufu Jiang,	Harbin Institute of Technology, China
Prof. Dr. Rasim İPEK,	Ege University
Prof. Dr. Ayşe AYTAÇ,	Kocaeli University
Prof. Dr. İhsan EFEOĞLU,	Ataturk University
Prof. Dr. Hüseyin Çimenoğlu,	Istanbul Technical University
Prof. Dr. Nuri Ersoy,	Bogazici University
Prof. Dr. Ali Kalkanlı,	Middle East Technical University
Prof. Dr. Mustafa BOZ,	Karabuk University
Prof. Dr. Sakin Zeytin,	Sakarya University
Prof. Dr. Yusuf ÖZÇATALBAŞ,	Gazi University
Prof. Dr. Halil ARIK,	Gazi University
Prof. Dr. Mustafa ACARER	Selçuk University

Prof. Dr. Fevzi Bedir,	Gebze Technical University
Prof. Dr. Mehmet Gavgali,	Necmettin Erbakan University
Prof. Dr. Hayrettin Ahlatçı,	Karabuk University
Prof. Dr. Ali Güngör,	Karabuk University
Prof. Dr. Burhanettin İnem,	Gazi University
Prof. Dr. Ramazan Çıtak,	Gazi University
Prof. Dr. Serkan Subaşı,	Düzce University
Prof. Dr. Nuri Ersoy,	Bagazici University
Prof. Dr. Bülent Kurt,	Nevsehir Haci Bektas Veli University
Prof. Dr. Melik Çetin,	Karabuk University
Prof. Dr. Fatma MEYDANERİ TEZEL,	Karabuk University
Prof. Dr. Harun MİNDİVAN,	Bilecik Şeyh Edebali University
Assoc. Prof. Mohamed Abdel-Hady Gepreel,	Egypt-Japan University of Science and Technology (E-JUST)
Assoc. Prof. Dr. Masaaki Nakai,	Kindai University, Japan
Assoc. Prof. Dr. Xiaojun Yan,	Dalian University, China
Assist. Prof. Dr. Ajay Kumar,	Indian Institute of Science Bangalore, India
Assoc. Prof. Dr. Sinan Kandemir,	Izmir Instutute of Technology
Assoc. Prof. Dr. Hakan Yılmazer,	Yildiz Technical University
Assoc. Prof. Dr. Yunus Türen,	Karabuk University
Assoc. Prof. Dr. Derya Dışpınar,	Istanbul University
Assoc. Prof. Dr. Mehmet Ünal,	Karabuk University
Assoc. Prof. Dr. Ayşe KALEMTAŞ,	Bursa Technial University
Assoc. Prof. Dr. Okan Ünal,	Karabuk University
Assoc. Prof. Dr. Ulaş Matik,	Karabuk University
Assoc. Prof. Dr. Erkan Koç,	Karabuk University
Assoc. Prof. Dr. Cemal Çarboğa,	Nevsehir Haci Bektas Veli University
Assoc. Prof. Dr. Arif Uzun,	Kastamonu University
Assoc. Prof. Dr. Abdullah Cahit Karaoğlanlı,	Bartın University
Assoc. Prof. Dr. İsmail ESEN,	Karabuk University
Assoc. Prof. Dr. Erkan KOÇ,	Karabuk University
Assoc. Prof. Dr. Kubilay KARACİF,	Hitit University
Assoc. Prof. Dr. Gökhan SUR,	Karabuk University
Assoc. Prof. Dr. Uğur Çalıgülü,	Fırat University
Assoc. Prof. Dr. Nurettin ELTUĞRAL,	Karabuk University
Assoc. Prof. Dr. Yasin KANBUR,	Karabuk University
Assoc. Prof. Dr. Hüseyin ZENGİN,	Karabuk University
Assoc. Prof. Dr. Yüksel Akınay,	Van Yuzuncu Yıl University
Assist. Prof. Faruk Mert,	Yıldırım Beyazıt University
Assist. Prof. Muhammed Elitaş,	Bilecik Şeyh Edebali University
Assist. Prof. Alper İncesu,	Karabuk University
Assist. Prof. Yasin Akgül,	Karabuk University
Assist. Prof. Süleyman YAŞIN,	Karabuk University
Assist. Prof. İsmail Hakkı KARA,	Karabuk University
Assist. Prof. Betül ERCAN,	Karabuk University
Assist. Prof. Ahmet Mustafa ERER,	Karabuk University
Dr. Ali Ramazani,	Massachusetts Institute of Technology, MIT
Dr. Martin Tauber,	CRM Alliance, Belgium
Dr. Tugçe Köden Yıldız,	Karabuk University
Dr. Hatice Yakut PEKTÜRK,	Kırklareli University

SECRETARY

Ece Duran,	Karabuk University
Esma Keskin,	Karabuk University
Hasan Durmaz,	Karabuk University

2nd International Symposium on Light Alloys and Composite Materials

31 March - 02 April 2022
Karabük University, Karabük, TURKEY.

PREFACE

The 2nd International Light Alloys and Composite Materials (UHAKS'22) was held by Karabuk University Iron-Steel Institute and KBU congress coordination center between 31 March - 02 April 2022 in the Iron-Steel Institute Conference Hall and online.

Thanks to the symposium, which we organized for the second time this year, universities and industrial organizations come together, leading to the emergence of new ideas and new collaborations on behalf of the current situation and future goals. A total of 86 papers were sent to the symposium. Most of the submitted papers were prepared by engineers, R&D personnel working in our industrial establishments and academic personnel at universities.

We would like to thank my colleagues who contributed greatly to the preparation of this symposium, and all our sponsors (Sağlam Metal, Mak Elektronik, Marzinc, and Ünal Mühendislik), and most importantly, I would like to express my gratitude to our University Rector Prof. Dr. Refik POLAT. We would like to see you again at the 3rd International Light Alloys and Composite Materials Symposium.

Chairs

Prof. Dr. Bilge DEMİR

Prof. Dr. Yavuz SUN

SPONSORS

2nd International Symposium on Light Alloys and Composite Materials

31 March - 02 April 2022
Karabuk University, Karabuk, Turkey

MARZINC

SAGLAMMETAL

MAK ELEKTRONİK
Malzeme Analiz ve Kalite Kontrol Cihazları Dış Tic. Ltd. Şti.

ünal®
mühendislik

UHAKS’22 Full Programme

	31.03.2022	LOCATION
Zoom Link: https://us02web.zoom.us/j/9107633276?pwd=M2VUL3RNWGMvMFZCU1Zuemt6QnU3Zz09 Meeting ID: 910 763 3276 Passcode: 12345		
10:00-10:05	Saygı Duruşu ve İstiklal Marşı	Karabük Üniversitesi Mühendislik Fakültesi Hamit Çepni Konferans Salonu
10:05-10:15	Tanıtım Filmlerinin Gösterimi	
10:15-11:15	Açılış ve Protokol Konuşmaları	
11:15-11:45	Sempozyum Davetli Konuşmacı Prof.Dr.Burak DİKİCİ, Atataürk Üniversitesi ‘‘ Metalik biyomalzemelerde yeni trend uygulamalar ve gelecek beklentileri ’’	
11:45-12:00	Dış Ticaret Elçileri Uyum Programı Sertifika ve Plaket Töreni	
12:00-13:30	Öğle Arası	

DAY 1	31.03.2022	LOCATION
Session Chair: Dr. M. Emre TURAN Zoom Link: https://us02web.zoom.us/j/9107633276?pwd=M2VUL3RNWGMvMFZCU1Zuemt6QnU3Zz09 Meeting ID: 910 763 3276 Passcode: 12345		
14:30-15:00	Invited Speker Dr. Martin Tauber, Chairman of the European Committee of the IMA ‘‘The Global Magnesium Market - Challenges & Opportunities ’’	Karabük Üniversitesi Demir Çelik Enstitüsü, ZOOM
15:05-15:35	Invited Speker Prof. Dr. Nakai Masaaki, Kındai University ‘‘ Effect of dimple texture on wear behaviors of β-type Ti-Nb-Ta-Zr and (α+β)-type Ti-6Al-4V ELI alloys in contact with zirconia for biomedical applications’’	
15:40-16:10	Invited Speker Prof. Dr. Mohamed A.H. Gepreel, Egypt-Japan University of Science and Technology ‘‘Recent Progress in the Development of Novel Low-Cost Ti Bio-Implants’’	
16:15-16:45	Invited Speker Assoc. Prof. Dr. Nermin Demirkol, Kocaeli University ‘‘Ceramics as a reinforcement material and a case study’’	
16:50-17:20	Invited Speker Assoc. Prof.Dr.Mevlüt GÜRBÜZ, Ondokuz Mayıs University ‘‘New Light Metal Alloy Composites and Entrepreneurship Case’’	

ORAL PRESENTATIONS

SESSION 1

	Room: 31.03.2022 -(14:00-15:40) Session Chair: Dr. İsmail Hakkı KARA	
Microsoft Teams: https://teams.microsoft.com/l/channel/19%3aTqb3pQNCZFyL381ktgu0pzIUnKwBUDNBioA6Ev8LxMQ1%40thread.tacv2/Genel?groupId=bf4960a7-bda5-4a34-a9ad-1fbdcf5766a9&tenantId=d348f9ab-4879-4a60-ab50-5c420b11470c Team Code: 32c7hnk		
Paper ID	Title	Authors
1	ABD matrix material models help in the efficient 3D study of laminate structures using Laminator	Mansingh Yadav
2	Numerical simulation of CH3NH3GeI3 based perovskite solar cell	Assiya Haddout
3	The Effect of Internal Stresses in Coated Fiber Composite Materials: Numerical Analysis.	Sara Ramdoum
4	Roll-Over Analysis of Commercial Vehicles	Osman Aydemir, Ahmet Sinan Öktem and Ahmet Semih Ertürk
5	Shot Peening Effect on Reduced Graphene Oxide-based AA1070 Alloys Produced by Stir Casting Technique	İremnur Bülbül, Remzi Varol and Mehmet Fahri Saraç
6	Particle size evolution of NiO/Al powders during high-energy ball milling	Nor El-Houda Berramdan, Hafida Boutefnouchet and Mosbah Zidani

	Room: 31.03.2022 -(16.00-17:20) Session Chair: Dr. Alper İNCESU	
Microsoft Teams: https://teams.microsoft.com/l/channel/19%3aTqb3pQNCZFyL381ktgu0pzIUnKwBUDNBioA6Ev8LxMQ1%40thread.tacv2/Genel?groupId=bf4960a7-bda5-4a34-a9ad-1fbdcf5766a9&tenantId=d348f9ab-4879-4a60-ab50-5c420b11470c Team Code: 32c7hnk		
Paper ID	Title	Authors
7	The evaluation of the force vs time graphics of punching process of AZ31 Mg alloy as shearing steps via experiment and Finite element analysis	Fadell Said Ahmed Aboshba, Bilge Demir, Hakan Gürün and Khalil Belras Ali
8	Mechanical Behaviour of the Auxetic Tubular Structure under High-speed Loading Conditions	Shao-Ho Huang and Fevzi Bedİr
9	The effect of particle type on wear and corrosion behaviour of MAO coatings on AZ31 alloy	Abubaker Ibrahım Elsadawi and Fatih Aydin
10	Investıgatıon Of Bıodegradabılıty Of Mechanıcal Alloyed Mg-Zn Powders Produced By Powder Metallurgy	Keriman Melis Halıcı and Rasim İpek
11	Wear Rate of Aged Mg-2.5Al-1.0Sn-0.3Mn-0.4La-0.66Gd Alloy	Esra Özsoy and İsmail Hakkı Kara

SESSION 2

	Room: ZOOM-01.04.2022 -(09:00-10:15) Session Chair: Dr.Engin ÇEVİK	
Zoom Link: https://us02web.zoom.us/j/9107633276?pwd=M2VUL3RNWGMvMFZCU1Zuemt6QnU3Zz09 Meeting ID: 910 763 3276 Passcode: 12345		
Paper ID	Title	Authors
12	Wear Behavior of Homogenized Mg-2.5Al-1.0Sn0.3Mn-0.4La-0.66Gd Mg Alloy	İsmail Hakkı Kara
13	POLYPROPYLENE MATRIX E-GLASS REINFORCED THERMOPLASTIC COMPOSITES AS AN ALTERNATIVE MATERIAL FOR LIGHT WEIGHT APPLICATIONS	Halenur Konbul, Aylin Altınbay Bekem and Ahmet Ünal
14	CORROSION PERFORMANCE OF CHROMIUM (III) COATED ON AA2024 USED IN AEROSPACE INDUSTRY	Cansel Pehlivanoglu, Emir Zafer Hosgun and Mustafa Ozgur Oteyaka
16	Selection of Aluminium Used as Heating Element Tube Material in Resistance Production	Mehmet Sahin, Fikri Negis, Sİnan Akbas, Salih Bektaş and Yunus Emre Dervis
17	Atomistic insight into the density effect on dynamic properties in 45S5 Melts	Youssef Ouldhnini, Achraf Atila, Said Ouaskit and Abdallatif Hasnaoui

	Room: ZOOM-01.04.2022 -(10:30-12:15) Session Chair: Dr.Safa POLAT	
Zoom Link: https://us02web.zoom.us/j/9107633276?pwd=M2VUL3RNWGMvMFZCU1Zuemt6QnU3Zz09 Meeting ID: 910 763 3276 Passcode: 12345		
Paper ID	Title	Authors
18	The wear behavior of SiC reinforced waste aluminum matrix composites	Özgür Yılmaz and Mevlüt Gürbüz
19	Fabrication of Ti6Al4V Composite Foams and Their Characterization	Ömür Ekrem Güntürk and Mevlüt Gürbüz
21	Investigating the Dynamic Compression Response of a Novel Lattice Topology via Finite Element Analyses	Hubannur Seremet and Nazim Babacan
22	Effects of La addition to Mg-2Zn-1Mn alloys	Halil Ahmet Gören, Mehmet Ünal, Yunus Türen and Hayrettin Ahlatçi
23	Investigation of Stress Distribution and Deformation Zones in Composite Sleepers by Finite Element Method	Mustafa Dursunlar, Musa Yılmaz, Ozan Yazar and İsmail Aykut Karamanlı
24	Cryogenic treatment effect on the mechanical and corrosion properties of 2024 aluminum alloy	Kamil Burak Göçmen and Mustafa Özgür Öteyaka

	Room: ZOOM-01.04.2022 -(14.30-16.00) Session Chair: Dr.Fatih AYDIN	
Zoom Link: https://us02web.zoom.us/j/9107633276?pwd=M2VUL3RNWGMvMFZCU1Zuemt6QnU3Zz09 Meeting ID: 910 763 3276 Passcode: 12345		
Paper ID	Title	Authors
27	Production and Characterization of Ti-Al Alloys by Powder Bed Electron Beam Melting	Emre Kocakusakli, Ozkan Gokcekaya, Burak Dikici, Faiz Muhaffel, Murat Baydogan, Takayoshi Nakano and Hakan Yilmazer
28	Design and Manufacture of Dual Asymmetric Centrifuge Homogenizer	Fatih Huzeyfe Öztürk and Özkan Öz
29	Comparative Microstructure of Additively Manufactured Ti-6Al-4V Alloy by Electron Beam Melting and Selective Laser Melting	Yusuf Atilla Sadıkoğlu, Şeyma Küçük, Hakan Yılmazer, Özkan Gökçekaya and Takayoshi Nakano
30	A Review for Weight Reduction in Automobiles: Lightening the Center Floor Panel	Ali Karafakıoğlu, Mustafa Kocaman, Fevzi Bedir, Sevil İnan Öz and Burak Dikici
31	The production method of titanium-based biocomposite scaffolds reinforced with hydroxyapatite-zirconia: A patent analysis	Mehmet Topuz, Mehmet Gavgali and Burak Dikici
32	Investigation of nano hydroxyapatite composite doped with nano zinc oxide in terms of bioactivity and mechanical properties	Büşranur Yildirim and Nermin Demirkol

	Room: ZOOM-01.04.2022 -(16.30-18:15) Session Chair: Dr.Yasin AKGÜL	
Zoom Link: https://us02web.zoom.us/j/9107633276?pwd=M2VUL3RNWGMvMFZCU1Zuemt6QnU3Zz09 Meeting ID: 910 763 3276 Passcode: 12345		
Paper ID	Title	Authors
34	INVESTIGATION ON THE EFFECT OF LEATHER SAWDUST ON MECHANICAL PROPERTİES OF EPOXY MATRIX COMPOSITES	Abdullah Dagdeviren, Muhammet Mevlüt Karaca and Yasin Akgül
36	Experimental Investigations on the Mechanical Properties, Wear analysis and Microstructure of CuAlNi/B4C Composites Synthesized Using Powder Metallurgy Route	Berhan Şahin, Tayfun Çetin, Muhammet Emre Turan and Mustafa Yaşar
38	INVESTIGATION OF HYDROXYAPATITE COATED MAGNESIUM AND TITANIUM ALLOYS BY SOL-GEL METHOD	Ece Duran, Hasan Durmaz, Esma Keskin, Bengü Akin, Hayreddin Boztaş, Aysun Işıkgül, Hayrettin Ahlatci, İsmail Esen and Yunus Türen

ORAL PRESENTATIONS (FACE TO FACE)

	Room: 01.04.2022 -(14:30-16:00) Session Chair: Dr. M. Emre TURAN	Location: Karabuk University Iron and Steel Institute
Paper ID	Title	Authors
15	Production and morphological investigation of Al6xxx-10Bi-3Mn alloy	Bünyamin Çiçek
20	Particle-reinforced multi-hybrid aluminium composite production and morphological analysis	Tuna Aydoğmuş
35	INFLUENCE OF TOOL ROTATION SPEED AND RATE ON THE CHARACTERIZATION OF FRICTION STIR WELDED DISSIMILAR SHEETS	Emir Tabanlioglu, Emre Yigitoglu and Mehtap Hidiroglu
39	Theoretical modelling of the Mg-Dia interface with nitride compounds for high thermal conductivity	Safa Polat, Muwafaq Mashrah

Poster Presentations

	31.03.2022	Location: Iron and Steel Institute
Paper ID	Title	Authors
33	An Investigation on PMMA-PC Composite Transparencies	Rıfat Yapıcı, Damla Köroğlu and Özlem Eker
37	An investigation The Effect of Cure Temperature on Carbon Fibre Composites	Damla Köroğlu, Engin Yörük and Yusuf Önalan

Roll-Over Analysis of Commercial Vehicles

Osman Aydemir*, Ahmet Sinan Öktem+, Ahmet Semih Ertürk#

*Department of Mechanical Engineering, Gebze Technical University, Kocaeli, Turkey,
osmanaydemir@gtu.edu.tr
+Department of Mechanical Engineering, Gebze Technical University, Kocaeli, Turkey,
sinan.oktem@gtu.edu.tr
#Department of Industrial and Materials Science, Chalmers University of Technology, Gothenburg, Sweden,
erturk@chalmers.se

***Abstract*— Nowadays, the use of commercial vehicles has been increasing day by day to reduce environmental pollution. Therefore, a significant increase is observed in the number of accidents and injuries caused by commercial vehicles. This increase in the world has led to the emergence of various regulations in order to ensure passenger safety in commercial vehicles. The ECE-R66 regulation has been published and become mandatory by European Commission for rollover accidents that cause death and injury. The requirements of this regulation can be provided by experiments. However, as it is known, there are various disadvantages such as high test costs and time-consuming procedures. Thanks to the development of technology, by using virtual analysis and finite element method, regulation conditions can be controlled in a faster and cheaper way than an experiment. Material models used in finite element simulations are of great importance and directly affect the simulation results. In addition, yield strength, strain, and strain-rate hardening parameters defined in the material model are crucial for the analysis to be carried out as close to the real experiment results. In this study, the finite element model was validated by performing a roll-over test for a section of a commercial vehicle. By using the tensile test results of the material, the material model was calibrated and implemented in the simulation. Furthermore, the strain-rate effects are investigated. As a result of the study, it is observed that values closer to the test data are obtained as a result of the simulations containing the material model calibrated using the tensile test. When the strain-rate effect is added to the material model, the simulation results are further improved and values quite close to the test data.**

***Keywords*— Finite element method; calibration; material model; strain-rate; hardening parameters**

Shot Peening Effect on Reduced Graphene Oxide-based AA1070 Alloys Produced by Stir Casting Technique

İremnur Bülbül[#], Remzi Varol[#], Mehmet Fahri Saraç[+]

[#]*Department of Mechanical Engineering, Faculty of Engineering, Suleyman Demirel University, Isparta, Turkey*
bulbul.irem09@gmail.com, remzivarol@sdu.edu.tr

[+]*Department of Automotive Engineering, Faculty of Engineering, Suleyman Demirel University, Isparta, Turkey*
fahrisarac@sdu.edu.tr

***Abstract*— The shot peening effects of reduced graphene oxide (rGO) additive on the structural, residual stress, hardness and surface roughness of AA1070 composites were investigated and reported in detail for the first time. It can be said that with increasing amounts of rGO added into AA1070 alloy, rGO is randomly distributed into the Al matrix with increasing amounts. The XRD analysis shows that there is no trace of carbon in the Al matrix, showing the the carbon structure did not diffuse into Al matrix during casting. However, in the EDS analysis, it was determined that the carbon value increased due to the increased presence of rGO. Although it has been studied according to the differences in ball diameters, it has been observed that the relative differences between the ball forging times affect the surface roughness changes in the samples. It was also observed that the hardness values were directly related to the ball forging times. On the other hand, the surface area of the forged matrix decreases in the presence of increasing rGO. While the hardness should increase after shot peening, cold deformation is not expected on the surface with the increase in the presence of rGO, and therefore, a decrease in the hardness value of the shot peened surface occurs. This is compatible with the residual stress results as well.**

***Keywords*—** reduced graphene oxide, AA1070, stir casting, severe shot peening

I. INTRODUCTION

Graphite oxides as reinforcement material in different composite structures has become very popular in recent years [1,2]. Due to its high surface area and superior mechanical properties make the use of this structure for aluminium matrix composites much more interesting. It is also of great importance for applications in the automotive components where excessive motion is occurred, such as cylinder liners, crankshaft, tappets, pistons in order to increase the desired properties such as lightweight surface hardness and mechanical strength in aluminium matrix composites (AMC) using a very small amount of reinforcement material [3].

Due to the structural dissimilarity of graphene oxide in the aluminium matrix, there are difficulties in its homogeneous distribution in the matrix. For that reason, the studies on surface strengthening of graphene oxide added AMC have been carried out by using techniques such as stirred casting, liquid metal impregnation, sprayed deposition casting and so on [4-8]. However, no study has been found on the rGO-added AMCs with stirred casting so far using surface hardening processes like shot peening [9-12].

With the shot peening process, the surface of the reduced graphene oxide structured AMC will be hardened by a massive amount of high hardness and high-speed kinetic energy projectiles [13-15]. After shot peening, residual stress field and microstructure enhance its fatigue, surface hardness, resistance to stress corrosion cracks or high temperature oxidation resistance. However, residual stress distribution, microstructure and surface roughness will also differ depending on shot peening properties such as diameter of balls, Almen intensity, time and projectile material [16,17]. In this study, the effect of shot peening with increasing graphene oxide (0.25%, 0.5% and 1% wt.) on AA1070 composites were empirically investigated by scanning electron microscopy, microhardness, residual stress and surface roughness.

II. MATERIAL AND METHOD

A. Material

AA1070 was purchased from ISM Foreign Trade, Turkey and its chemical composition of the AA1070 alloy is presented in Table 1. The main reason for choosing the specified alloy is to examine the interaction of aluminum with the highest possible purity against graphene oxide. In the synthesis of graphene oxide, graphite (<20 μm powder), sulfuric acid (H_2SO_4.98%), sodium nitrate ($NaNO_3$), hydrogen peroxide (H_2O_2,30%) and potassium permanganate ($KMnO_4$, 98%) were obtained from Sigma Aldrich.

TABLE I
CHEMICAL COMPOSITION OF AA1070 ALLOY, % WEIGHT

Element	**Al**	**Cu**	**Fe**	**Mg**	**Mn**	**Si**	**Ti**	**V**	**Zn**
% wt	rmn	0.04	0.25	0.03	0.03	0.2	0.03	0.05	0.04

B. Method

Reduced graphene oxide was produced by the modified Hummers method [18]. To explain shortly, 3 g of natural graphite was mixed with sodium nitrate (1.2 g) for 30 minutes in a beaker placed in an ice bath at 1°C, and 150 mL of sulfuric acid was then added. Afterwards, potassium permanganate (12 g) was added to oxidize the graphite. After the resulting solution was removed from the ice bath, it was subjected to magnetic stirring at 35°C for 90 minutes. So, it was observed that a rapid increase in temperature occurred with the addition of ultrapure water. The temperature was kept below 100°C. After these procedures, the solution, which is stirred for another 30 minutes, is diluted with 300 mL of ultrapure water and the reaction is terminated by adding 20 mL of 30% hydrogen peroxide. Finally, the mixture is washed sequentially with HCl and H_2O, then centrifuged at 4000 rpm for 10 minutes to separate the solid and dried under vacuum at 80°C overnight to yield graphene oxide powder.

Reduced graphene oxide with 0.25%, 0.5% and 1% (wt.) was separately added to the melted AA1070 alloy in a graphite crucible with a graphite probe, and after mixing at 4000 rpm for 5 minutes. Afterwards, a melted sample poured into the mold of a tubular shape of 10 mm in diameter and 10 cm in length and waited for cooling. Afterwards, each sample with a length of 10 mm was cut and made ready for structural and mechanical tests.

Severe shot peening process were applied with three Almen intensities of A10-12, A14-16 and A16-18 with other parameters remain constant. Severe shot peening treatment was conducted in accordance with MIL-13165 standard under the conditions shown in Table 2.

TABLE III
SEVERE SHOT PEENING PARAMETERS

Almen Intensity	Ball type and related hardness	Air pressure (bar)	Flow rate (kg/dk)	Saturation rate	Shot peening time (sn)
A10-12	S110, 45-52 HRc	4.5	5.0	100%	35
A14-16	S170, 45-52 HRc	5.5	5.5	100%	31
A16-18	S230, 45-52 HRc	5.5	5.0	100%	42

III. RESULTS AND DISCUSSION

The average shot peened layer under three different Almen intensity was illustrated in Fig 1. The shot peened layer is increased gradually from 0.74mm to 1.08mm. Almen intensity depends on the shot peening parameters. Ball or called projectile diameter, air pressure, saturation rate and shot peening time especially affect shot peening intensity. In this study, Almen intensity values were determined using A strips. As the Forging Intensity values increase, the shot peened layer thickness increases. As the Almen intensity increases, the kinetic energy value transferred to the forged material by the balls used in forging increases. Therefore, the forged or shot peened layer thickness increases. This result is compatible with the literature.

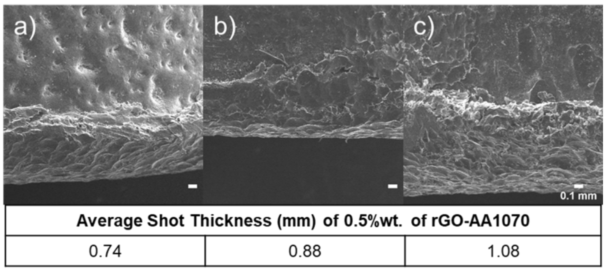

Average Shot Thickness (mm) of 0.5%wt. of rGO-AA1070		
0.74	0.88	1.08

Fig. 1 Average Shot Peened Microstructure of a)0.25%, b)0.5% and c) 1% wt. of rGO added AA1070 samples after shot peening

For selected 0.25%wt. of rGO added AA1070 samples, the surface roughnesses with four different shot peening treatments were shown in Fig 2. The surface roughness of sample at unpeened condition was 2.8 and gradually is increased gradually from 7.5 to 9.2µm. Afterwards, the surface roughness suddenly decreases to 8.8 µm under A16-18 Almen instensity. At the A16-18 Almen intensity, the forging time was 42 seconds. By using S230 ball, the increase in this time causes the improvement of the surface quality. In the case of using S170 ball, since the applied air pressure value is the same, the impact speed was lower because the mass of the S230 ball was higher. As a result, the surface quality was obtained better than the surface quality obtained under forging conditions using S170 ball diameter.

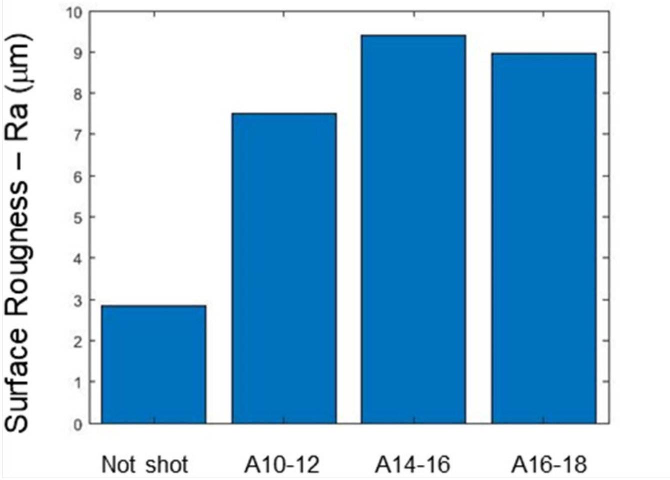

Fig. 2 Average surface roughness of selected 0.25%wt. of rGO added AA1070 samples under different Almen intensity

As seen in Fig 3., xrd analysis of pure and rGO added AA1070 matrix composite shows a single-phase structure of pure aluminium phase identification (JCPDS card no. 04-0787) which are present at 2θ equal to 38.47°, 44.74° and 65.13°, 78.23° and 82.43°. There is no trace of carbon in the Al matrix, so it is an evidence that there is no second phase such as Al3C in the matrix. So, the rGO has not enough time to react with Al matrix during stir casting.

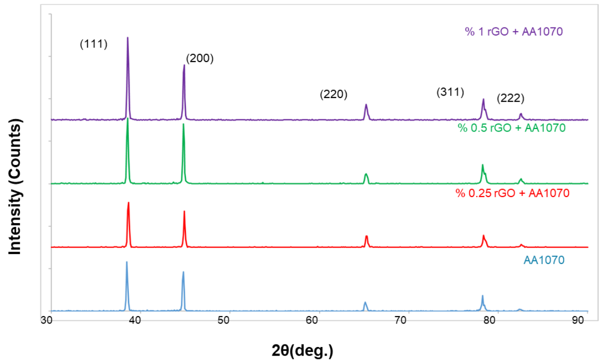

Fig. 1 XRD analysis of pure and rGO added AA1070 composites

SEM images and SEM-EDS analysis of pure and rGO added AA1070 samples were shown in Fig 4. It is clearly seen that rGO particles were randomly distributed into Al matrix and the presence of rGO increases with increasing amount of rGO into the Al matrix. It is also seen at the EDS analysis that carbon is observed even at 0.25%wt. of rGO added AA1070 samples and gradually increases from 1.78 %wt to 8.88 %wt of carbon. Apart from AA1070 sample, rGO particles are clearly visible (marked as red circle) on the Al matrix which is compatible with the EDS analysis.

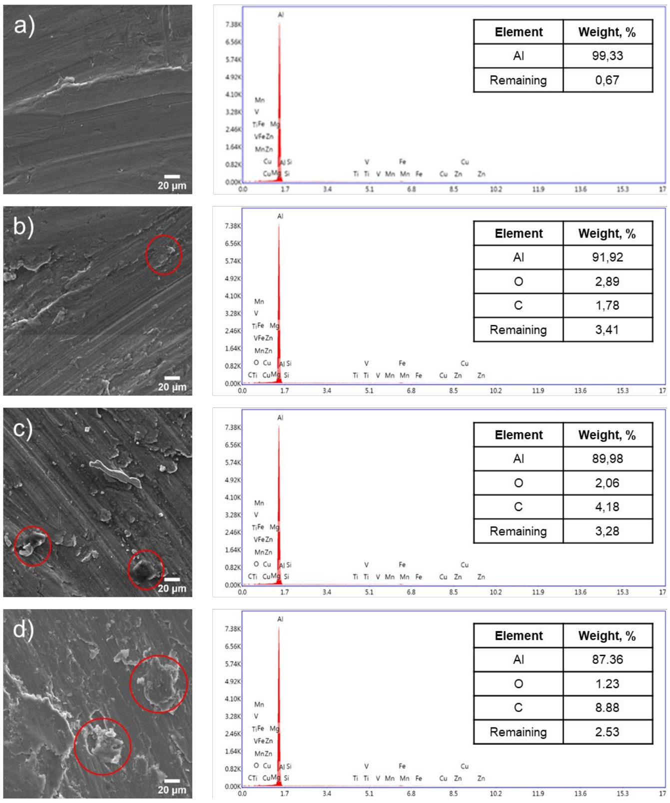

a)

Element	Weight, %
Al	99,33
Remaining	0,67

b)

Element	Weight, %
Al	91,92
O	2,89
C	1,78
Remaining	3,41

c)

Element	Weight, %
Al	89,98
O	2,06
C	4,18
Remaining	3,28

d)

Element	Weight, %
Al	87.36
O	1.23
C	8.88
Remaining	2.53

Fig. 4 SEM and EDS analysis of pure and rGO added AA1070 samples

As it seen in Fig 5., the hardness values were decreased with increasing amount of rGO under various shot peening intensity. This observation can be concluded that even 0.25%wt. of rGO amount is still higher because it is not closer to pure AA1070 sample. It could be interpreted that rGO particles were agglomerated during the casting process and lower the hardness at the end. During the shot peening treatment, at least 99% of the surface is struck by the balls. However, as the amount of rGO added into the matrix material (AA1070) increases, the surface area of the forged material decreases. Essentially, it is the hardening that occurs during cold deformation of the surface of the shot peened material that reveals the increase in hardness. However, hardening of rGO should not be expected. Therefore, as the amount of rGO increases, the decrease in the hardness value of the shot peened surface is considered for this situation.

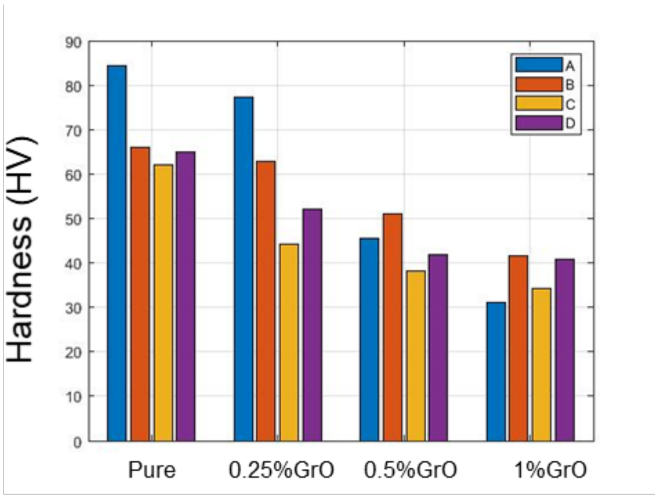

Fig. 5 XRD analysis of pure and rGO added AA1070 composites

X-ray diffraction residual stress measurements was applied to all samples under different shot peening treatments, as seen in Table 3. 0.25%wt. of rGO added AA1070 with increasing shot peening intensity decreases the residual stress which verify that surface area of rGO over 0.25% addition did not make any distinctive change against other samples. Residual stress results match exactly with the hardness values. This shows that the hardening effect is highly dependent on the residual stress as well.

TABLE IIIII
RESIDUAL STRESS OF REDUCED GRAPHENE OXIDE ADDED AA1070 SAMPLES UNDER THREE DIFFERENT ALMEN INTENSITY

Almen Intensity	Residual Stress (MPa)			
	Pure	%0.25GrO	%0.5GrO	%1GrO
A10-12	-37.3±1.8	-44.7±1.6	-37.2±1.1	-36.3±1.9
A14-16	-41.1±1.1	-38.5±2.0	-41.0±1.7	-30.3±4.0
A16-18	-32.7±1.5	-35.5±0.9	-32.6±1.2	-30.3±1.8

IV. CONCLUSIONS

Pure and three different ratios (0.25, 0.5 and 1%wt.) of rGO added AA1070 composites were produced by stir casting and afterwards, severe shot peening applied for all samples. Under three different Almen intensity, the shot thickness and surface roughness increase up to A14-16 and then decreases. These phenomena are also observed at the hardness and residual stress values. Depending on the various Almen intensity and relative shot time differences, it can be interpreted that A14-16 Almen intensity is the optimum shot intensity value should be used for rGO added AA1070 samples. On the other hand, there is no trace of carbon reacted with Al matrix which is verified by xrd analysis. For SEM observation, rGO is randomly distributed into Al matrix and increases with increasing amount of rGO added into AA1070. Finally, residul stress of 0.25 %wt. of rGO added AA1070 was gradually decreased with incrasing Almen intensity while other samples show drastic change. This is a similar situation observed in the change of hardness and surface roughness due to the hardening phenomena observed in presence of rGO added into Al matrix.

ACKNOWLEDGMENT

We would like to specifically thank Suleyman Demirel University Scientific Research Projects Coordination Unit for financially supporting our work with the project numbered SDU BAP FYL-2021-8294.

REFERENCES

[1] Z. Zheng, S. Zhong, X. Zhang, J. Li, L. Geng, "Graphene nano-platelets reinforced aluminum com tropic compressive properties," *Materials Science and Engineering: A*, vol. 798: 140234, Nov. 2020.

[2] A. Naseer, F. Ahmad, M. Aslam, B. Guan, W. Harun, N. Muhamad, M. Raza, R. German, "A review of processing techniques for graphene-reinforced metal matrix composites," *Materials and Manufacturing Processes,* vol.34, pp. 957–985, Jun. 2019.

[3] A. Naseer, F. Ahmad, M. Aslam, B. H. Guan, W. S. W. Harun, N. Muhamad, M. R. Raza and R. M. German, "A review of processing techniques for graphene-reinforced metal matrix composites," *Materials and Manufacturing Processes*, vol. 34, pp. 957-985, Jun. 2019.

[4] Z. Zheng, X. Zhang, J. C. Li and L. Geng, "High-content graphene nanoplatelet reinforced aluminum composites produced by ball milling and hot extrusion," *Science China Technological Sciences, vol.* 63, pp. 1426–1435, Jul. 2020.

[5] Y. Wu, K. Zhan, Z. Yang, W. Sun, B. Zhao, Y. Yan and J. Yang, "Graphene oxide/Al composites with enhanced mechanical properties fabricated by simple electrostatic interaction and powder metallurgy," *Journal of Alloys and Compounds*, vol. 775, pp. 233-240, Feb. 2019.

[6] A. Fadavi Boostani, S. Yazdani, R. Azari Khosroshahi, Z.Y. Jiang and D. Wei, "A novel graphene-stimulated semi-solid processing to fabricate advanced aluminium matrix nanocomposites," *Materials Science and Engineering: A*, vol. 736, pp. 316-322, Oct. 2018.

[7] F. Toptan, A. Kilicarslan, A. Karaaslan, M. Cigdem, I. Kerti, "Processing and microstructural characterisation of AA 1070 and AA 6063 matrix B_4Cp reinforced composites," *Materials & Design*, vol. 31, pp. 87-91, Jun. 2010.

[8] Z.O. Pehlivanlı and M. Pul "Investigation of the effect of B_4C amount and sintering temperature on the thermal properties of the material in Al 1070–B4C composites," *Proceedings of the Institution of Mechanical Engineers, Part L: Journal of Materials: Design and Applications*, vol. 235, pp. 2746–2761, Aug. 2021.

[9] K. Zhu, Z. Li, C. Jiang, "Surface mechanical properties of shot-peened CNT/Al–Mg–Si alloy composites," *Journal of Alloys and Compounds*, vol. 773, pp 1048-1053, Jan. 2019.

[10] F. A. R Rozhbiany and S.R. Jalal, "Influence of reinforcement and processing on aluminum matrix composites modified by stir casting route," *Advanced Composites Letters,* vol.28, pp. 1-8, Dec. 2019.

[11] K.S.K. Sasikumar, K. Dineshkumar, K. Deeban, M. Sambathkumar and N. Saravanan, "Effect of shot peening on surface properties of Al7075 hybrid aluminum metal matrix composites," *Materials Today: Proceedings*, vol 33, pp. 2792-2794, Apr. 2020.

[12] Q. Sun, X. Liu, Q. Han, J. Li, R. Xu, K. Zhao, "A comparison of AA2024 and AA7150 subjected to ultrasonic shot peening: Microstructure, surface segregation and corrosion," *Surface and Coatings Technology*, vol. 337, pp. 552-560, Mar. 2018.

[13] K. Zhan, Y. Wu, J. Li, B. Zhao, Y. Yan, L. Xie, L. Wang and V. Ji, "Investigation on surface layer characteristics of shot peened graphene reinforced Al composite by X-ray diffraction method," *Applied Surface Science*, vol. 435, pp. 1257-1264, Mar. 2018.

[14] K. Zhu, C. Jiang, Z. Li, L. Du, Y. Zhao, Z. Chai, L. Wang, M. Chen, "Residual stress and microstructure of the CNT/6061 composite after shot peening," *Materials & Design*, vol. 107, pp. 333-340, Oct. 2016.

[15] K. Zhan, Y. Wu, J. Li, B. Zhao, Y. Yan, and L. Wang, "Analysis of recrystallization behavior of shot peened graphene reinforced Al composites during isothermal annealing by X-ray diffraction method," *Journal of Alloys and Compounds*, vol. 765, pp. 862-868, Oct. 2018.

[16] J. Venumurali , G. Bhanodaya Reddy, "Shot Peening Effect on Surface Characteristics and Mechanical Properties of Aluminum Matrix Composite," *Manufacturing Technology Today,* vol. 18, pp. 3-9, Oct. 2019.

[17] K.S.K. Sasikumar, K. Dineshkumar, K. Deeban, M. Sambathkumar, N. Saravanan, "Effect of shot peening on surface properties of Al7075 hybrid aluminum metal matrix composites," *Materials Today: Proceedings*, vol. 33, pp. 2792-2794, Apr. 2020.

[18] Z. Ciğeroğlu, A. Haşimoğlu, and O.K. Özdemir, "Synthesis, characterization and an application of graphene oxide nanopowder: methylene blue adsorption and comparison between experimental data and literature data," *Journal of Dispersion Science and Technology*, vol. 42, pp. 771-783, Jan. 2020.

Particle size evolution of NiO/Al powders during high-energy ball milling.

Nor-El-houda Berramdan*, Hafida Boutefnouchet+, Mosbah Zidani#

* *Department of Materials Science and Engineering, National Higher School of Mining and Metallurgy 'ENSMM' Amar Laskri, EX CIFOS chaiba BP 233 RP Annaba W129, Sidi Amar, Algeria*

+ *Department of Metallurgy, University of Badji Mokhtar, 17 hassen chaouche, 23000 Annaba, Algeria*

Department of Metallurgy, University of Mohamed khider, BP 145 RP 07000 Biskra, Algeria
Faculty of Technology, University of Batna 2, N 3 RN3, Batna, Algeria
nor-el-houda.berramdane@ensmm-annaba.dz
hafida.boutefnouchet@univ-annaba.dz
m.zidani@univ-batna2.dz

***Abstract*— This paper investigates the particles size evolution during high-energy ball milling of the NiO/Al system. Starting powders were milled under air for different milling times and speeds. All samples were characterized using scanning electron microscopy (SEM) and X-ray diffraction. However, XRD results show that with increasing milling time and/or speed NiO and Al peaks intensities were reduced, and their peaks width became larger. Furthermore, the broadening of XRD peaks is related to the decrease in particles size and lattice strain enhancement. The calculations of products particle size were done using the Williamson hall plot method. Scanning electron microscopy (SEM) of pure and milled powders was investigated.**

***Keywords*— Particle size, high-energy ball mill, NiO-Al system, Williamson Hall Plot.**

Mechanical Behaviour of the Auxetic Tubular Structure under Low-Speed Loading Conditions

Shao-Ho HUANG*, Fevzi BEDIR*
Gebze Technical University Dept. Mechanical Eng. Gebze/ Kocaeli-Turkey

***Abstract*—Auxetic structure or material that obtains negative Poisson's ratio(NPR) gives us a great opportunity to manufacture more fascinating products. When Auxetic structure bearing compressive loading auxetic structure would contract rather expand and acts oppositely under tensile. This behavior performs differently from normal structures and because of this specialty, auxetic structure applies spectacular ability for enduring compacts, good indentation resistance, energy absorption capability, and shear resistance. To achieve improved properties for engineering submissions, there are plenty existed pieces of articles that demonstrated the possibility of auxetic structures. Different material-based specimens, providing subtle differences in composition or combining different types are the most common methodologies. However, most research only mentioned the behaviors that occur under loading in beam shape or 2D sketches. In real applications, tubular structures are also essential for building significant products. As a result, the two most studied geometries; re-entrant structure and tetrachiral structure are selected as the unit cell configuration to build the auxetic tubular structure. The main idea in this paper is to observe the kinematics of the auxetic tubular structure when bearing different loadings, the result complies with the research which studied the in-plane properties under the impact of auxetic structures, however, when the loading exceeds significant quantity, the behaviors of auxetic tubular structure gives a unique result.**

***Keywords*—auxetic structure, NPR, tubular structure, re-entrant, tetrachiral**

I. INTRODUCTION

The first time that the noun of auxetic structure can be traced back to 1991 was written by Evans[1]. This kind of structure introduces opposite physical behaviour from normal materials due to its negative Poisson ratio (NPR). Auxetic structure expands when being pulled and contracts under pressure[2] which gives a certainly unlike physical performance. Based on our knowledge, Poisson's ratio v is the negative ratio of transverse strain to axial strain. When normal material is applied compression stress axial strain reduces, the meanwhile transverse strain increases, and when normal material is applied tensile stress, axial strain increases then transverse strain reduces. The auxetic structure however obtains an opposite characteristic from normal materials. People have noticed this special structure due to engineering needs for over 30 years, however, there is still not much investigation in this area, which means this topic is still quite new. Yet the topic is new, there are plentiful natural auxetic materials exist in nature for a long time. For example, the auxetic structural skin of salamander gives it a good ability to escape from its predators[3]. This feature also appears on the skin of cats, snakes, and cow teats which helps them behaving some abnormal motion.

NPR specialty gives us a promising opportunity to produce products with lighter weight and better performance when bearing force which is because many material properties are related to the value of v. For example, The indentation resistance had been discussed that enhanced with an auxetic structure based on the theory that the indentation resistance is proportional to $[(1 - v^2)/E]^{-1}$[4], [5]. since v is a value which only performs between -1 and 0.5, and most normal materials only obtain positive Poisson's ratio which means generally this fact can slightly affect material properties. The auxetic structure however through subtle adjustment might meet Poisson's ratio between -1 to -1/2, which leads $(1 - v^2)$ to approach 0 when v approaching -1, as a result, it can lead to indentation resistance infinity. Under loading makes normal material density reduce, however, for auxetic structure loading causes contraction which can enhance the indentation of the structure. The NPR specialty can also increase the toughness under compression in re-entrant foam[6], [7], which introduced auxetic structure into foam shape through ejecting foam into the preheated metallic cube and under compression then heat for a determined time. The result that had been shown indicated the auxetic structure can promise a good application. Enhancing the localized impulsive loads has also been confirmed that can be achieved in auxetic structures(Xiao, Chen, Li, Wu, &Fang, 2019).

There are numerous forms of auxetic structure[10]. First of all, the auxetic structure can be divided into two types according to the source: natural and synthetic or we can call it man-made. Natural auxetic material has two forms: biological and mineral. As for synthetic auxetic structure, according to deformation way when bearing loads may be split into two main assemblies: two-dimensional and three-dimensional. Though natural auxetic materials are also important for many aspects, this paper's focus will be on synthetic structure introduction rather natural one. Synthetic structures can be divided into two groups: 2-dimensional and 3-dimensional structures. The 2-dimensional structure contains the missing-rib type[11], perforated plates[12], rotating units[13], and composites[14]. As for 3-dimensional structure, open-cell foams[15], crumpled sheets[16], Miura-ori folded structure[17], and entangled single wire model[18] are included. Except for the structures that are mentioned above, re-entrant[19], and chiral[20] which are widely researched both in 2-dimensional structure and 3-dimensional structure are the main unit cell geometries in this paper. The re-entrant construction is labelled as a tension functioned on a side of the solid in a way that outcomes in the extension of the adjacent edges[21]. The re-entrant structure is a basic geometry that has an angle in a polygon, larger than 1800, or a negative angle. The re-entrant structure is one of the most studied auxetic structures. To improve the structure strength, there are many different types had been implemented. For re-entrant structure, one of the methods that are applied to strengthen the structure's stiffness is to add firming up rib into regular auxetic unit cells in a direction vertical to the re-entrant direction [22], this article indicated that it is possible to enhance Young's modulus and shear modulus through adjusting the range of relative density. Another research also presented that changing the gap geometry is also a methodology to improve energy absorption capability[23]. Or some other subtle differences between cells are implemented such as angle adjustment may have a chance to advance the performance when bearing loads[24], [25]. Furthermore, the thickness of the re-entrant structure also plays an important role to affect the NPR behaviour[26]. Both thick-walled and thin-walled re-entrant structures exhibit NPR behaviour, however, the thickness of the re-entrant structures can affect the deformation mode of it, which may influence the structure's performance. If a structure or geometry after rotating translating cannot be superposed to its mirror image, we can call it has chirality[27]. Many different design concepts of the chiral type have been introduced since the first designed chiral geometry came out[28]. The chiral structure can illustrate the relationship between local rotation, substance deformation, and bending, therefore providing that explanation for the derivation of many uncommon performances such as NPR of chiral materials The chiral unit cell is consisting of an arrangement of spherical cross-section cylinders of alike radius connected by ligaments of identical measurement, ligaments are tangentially connected in the end. this kind of auxetic structure is the same as the re-entrant structure that can both be applied to 2D and 3D applications. Even in the natural, there are plenty sorts of chiral structures that exist for instance: human left-hand and right-hand, DNA, etc. The chiral structure is like a re-entrant structure, lots of variations are proposed such as hexachiral, trichiral, anti-trichiral, tetrachiral, and anti-tetrachiral[29]. The chiral structure can be divided into three main groups: anti-chiral, chiral, and meta-chiral[27]. The re-entrant and chiral structures are proved to have significant mechanical behaviour in many literary works, however, the properties exhibited in written papers are mostly focused on in-plane behaviours in beam shape.

In this paper, the tubular structure which is relatively little studied specimen form in auxetic structure area is applied low impact to observe the kinematics of the structures. The two base geometries, re-entrant and tetrachiral are designed as the unit cell to become tubular constructions that exhibit no dangling ends. With no dangling ends efficiently allows every unit cell affects one another.

II. DESIGN AND BOUNDARY CONDITIONS

A. *Geometry of Specimens*

In this paper, there are two kinds of auxetic being discussed, Re-entrant and tetrachiral tubular structures. Two structures are in the same thickness height, radius. the model will be manufactured in 60 mm to trial the mechanical properties. Re-entrant and tetrachiral cells shown in Fig. 1 are selected to be the base geometry. The asymmetrical graph is adopted to achieve the most similar magnitude of both re-entrant and tetrachiral tubular structures. The radius ratio of the tetrachiral unit cell is 0.33 [30]. Each tubular structure consists of 5 layers[26]. These two geometries are designed by SOLIDWORK 2020, and the simulation process is executed by LS-DYNA with explicit dynamic simulation to understand the kinematic of structures.

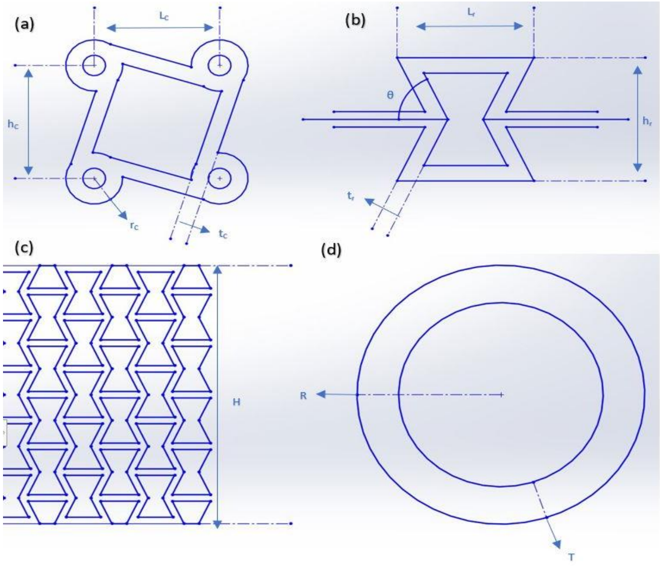

Fig. 1. 2D schemes of (a) Tetrachiral unit cell (b) Re-entrant unit cell (c) Tubular structure front view (d) Tubular structure top view.

B. *LS-DYNA Pre-Post*

In this chapter numerical simulations which are made from LS-DYNA software and the result of specimens under impulsive test will be discussed. The main purpose is to observe the structural behaviours under impact. The following contents describe the steps of setting data for the simulation. Specimens with the parameters shown in Table 1 are employed with the ABS-M30 of material. A solid part made plate in 128 elements and 243 nodes which is set by MAT_003-PLASTIC_KINEMATIC provides the impact to the specimens. The velocities that are provided to the plate through the VELOCITY_GENERATION card dominate the desired velocities to provide specimens impact. The velocities are changed in VY, which is the longitudinal direction along with the specimen. The velocities of the plate are used to be the numerical analysis with 277 mm/s, 833 mm/s, 1388 mm/s, 1944 mm/s, 2500 mm/s respectively, and the bottom nodes of the specimens are set displacement in VY. The determination time is set as 0.04 seconds to observe the structural changes in this duration, and the procedure is divided into 10 pieces when progressing the simulation as shown below.

Table 1.

Parameters of specimens.

Structure category	Height (mm)	Length (mm)	Radius (mm)	Strut angle	Thickness (mm)
Tetrachiral unit cell	11	11	2.5		1.5
Re-entrant unit cell	12	12		65^0	1.5
Tetrachiral tubular structure	60		28		10
Re-entrant tubular structure	60		28		10

III. SIMULATION ANALYSIS

A. Re-entrant Structure Analysis

In this section, the results that are obtained from the simulations are compared by different applied velocities. The analysis is focused on the stress distribution, deformation state, and the NPR behaviour of the auxetic tubular structure. The Poisson's ratio is calculated by the following formula[31]

$$v_i = -\frac{\varepsilon_{xz}}{\varepsilon_y} = -\frac{\Delta d_i/D}{\Delta y_i/Y_i} \quad (1 \le i \le 5)$$

$$\bar{v} = \frac{1}{5} \times \sum_{1}^{5} v_i \quad (1 \le i \le 5)$$

Where $\Delta d_i = \frac{d_i + d_{i+1}}{2} - D$, $,\Delta y_i = y_i - Y$. D is the diameter of the auxetic tubular structure before deformation, d_i is the ith layer diameter of the auxetic tubular structure after deformation, Y is the height of the unit cell before deformation, and y_i is the height of ith layer after deformation.

The following content is discussing the stress distribution of the re-entrant structure, Fig. 3 shows the strain-stress curve, and Fig. 4 shows the schemes of the re-entrant structure under various loading when the loading is applied to the structure, the upper layers bear the most stress at the beginning, and after a few moments later, the stress is concentrated to the lower part, due to the amount of velocity is not very big, there is no obvious deformation. However, through the stress distribution figure can find that the structural behaviour follows the beam shape auxetic structure under the impact, and because of the tubular structure, the stress concentrates to the center rather than expansion. When the loading that applied on the re-entrant structure gradually increased, the deformation mode of the bulking structure starts to become not harmonious due to the bending of horizontal struts affecting the longitudinal struts plastically.

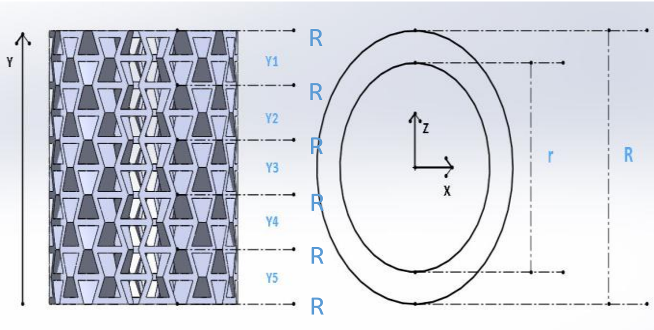

Fig 2. Calculating Poisson's ratio using an imaging processing method from two perspective views: (a) top view; (b) front view.

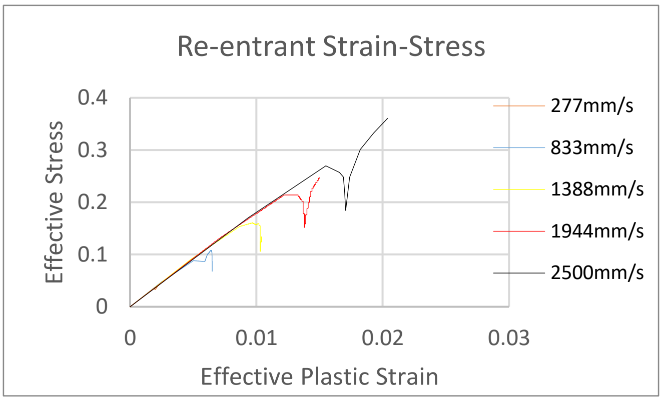

Fig 3. Strain-stress curves of the re-entrant structure under loadings.

The stress distribution indicates the NPR behaviour does not occur in each layer on separate timing, this reaction mode perfectly meets the result of sandwich beam form auxetic structure under impulsive loadings[9]. The impulsive wave affects the top layers of the auxetic structure, and the number of affected layers is depending on the amount of velocity. Initially, the loading applies stress on the inclined struts, which causes the longitudinal deformation then the inclined struts bring the horizontal struts to concentrate toward the central part of the structure and behave the NPR specialty. According to the expansion stress mode, the stress gradually distributes from the upper layers to the lower layers, and from the outer face to the interface. This bulking mode gives promising agreement with the re-entrant structural behaviour of thick thickness type[26]. From the horizontal deformation extent of the re-entrant structure, the NPR behaviour can be observed, except the 2500 mm/s of velocity loading which makes an excessive deformation inside the structure and makes unit cells behave abnormally. Due to the malformation of the re-entrant structure, the most stressed top layer, and bottom layer display differently from smaller velocity loading. The next section is about to discuss the Poisson's ratio which is the most important part of the auxetic structure. As shown in Fig. 5, except for the 2500 mm/s of loading velocity cure, the NPR behaviour does not appear at the initial time point, and the amount of velocity decides the NPR behaviour during the middle of the time frame, after a certain duration the increasing rapidity of the Poisson's ratio become slower.

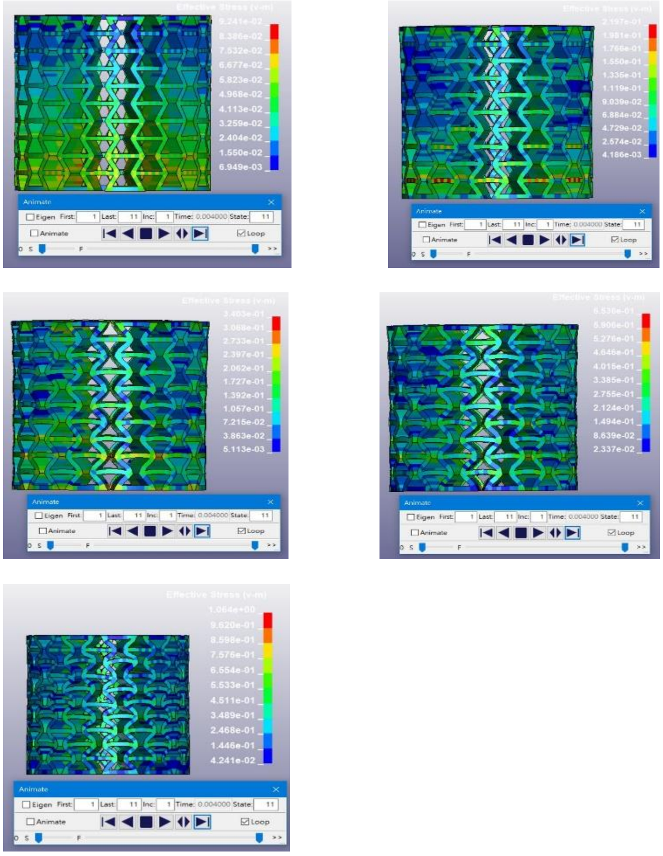

Fig. 4. Schemes of the re-entrant structure under (a)277 mm/s (b) 833 mm/s (c) 1388 mm/s (d) 1944 mm/s (e) 2500 mm/s velocity loading.

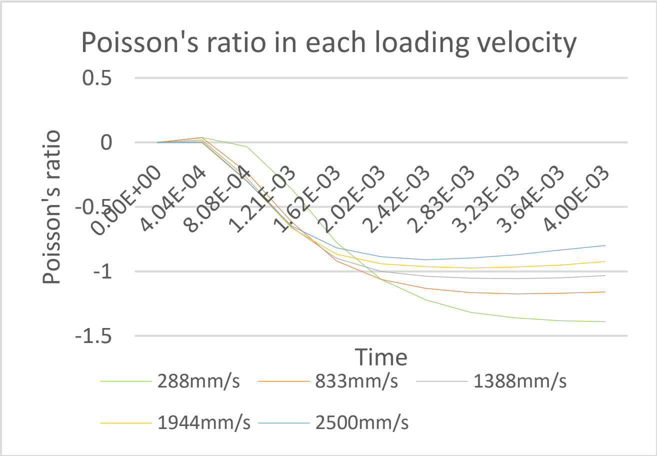

Fig. 5. Poisson's ratio in each loading velocity during impact.

The result indicates that Poisson's ratio is inversely proportional to the loading velocity. Through the stress distribution figures, a small amount of loading velocity conducts stress to the bottom part averagely, and until the end of the time frame, the stress remains in the lower parts and the most severe stress occurs on inter structure which is the path of central concentration. Increasing velocities lead to additionally abnormal deformation of unit cells when the structure condenses to the limitation of the unit cell which means the horizontal part of the unit cells squeezes and interferes with the deformation mode of each unit cell. The interference of unit cells as shown in Fig. 6 leads to the Poisson's ratio reduction of the bulking structure.

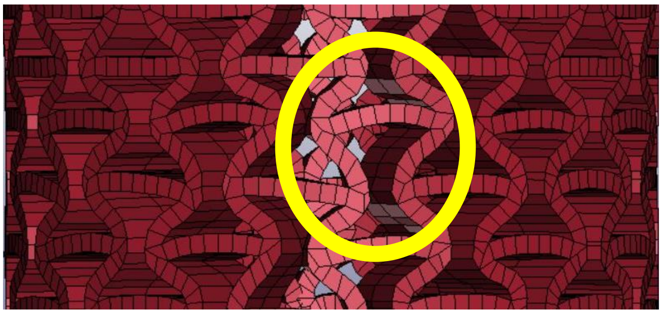

Fig. 6. Scheme of re-entrant structure with abnormal deformation.

B. *Tetrachiral Structure Analysis*

Tetrachiral structure is the main subject that is discussed in this part, as the same as re-entrant structure, tetrachiral structure is also a well-known auxetic structure that has been proved to perform NPR behaviour under loading. In this part, the stress distribution, deforming mode, and the Poisson's ratio it obtains are discussed. Fig. 7 shows the Strain-Stress curve of the tetrachiral structure and Fig. 8 shows the schemes of the tetrachiral structure under various loading, the figures display a different performance of stress distribution from re-entrant structure, and the deformation pattern meets the in-plane deformation pattern. The stress distribution figures that are presented below showing when the stress is applied to the structure, the first layer which is the first contacted layer enduring the most stress at the initial moment, however, different from the re-entrant structure, tetrachiral structure transfers stress through inter part to the lower layer, which is related to the unit cell deformation pattern. Tetrachiral structure deforms under loading with "Z" mode which has a good agreement with in-plane crushing deformation mode[30], the tubular structure however rotates rather squishes. The upper layer and the bottom layer rotate in an opposite direction which leads the middle layers to contract toward the central part and it helps to perform NPR behaviour. Fig. 8 also indicates except for the first layer; other layers deform to a certain extent the deformation ceases. Which is also meeting

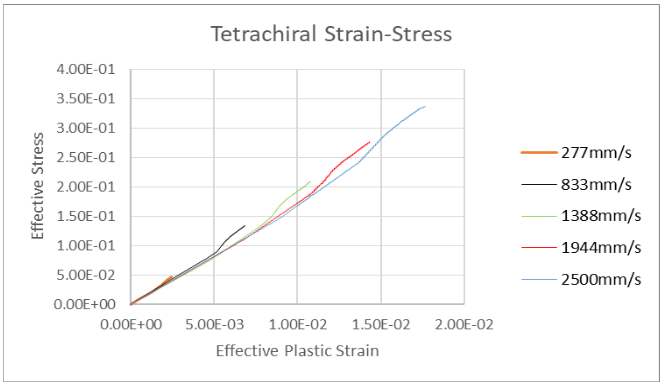

Fig. 7. Strain-stress curves of the re-entrant structure under loading

the in-plane crushing behaviour of the tetrachiral structure. According to the figures shown above, the deformation pattern of the tetrachiral structure shows the first layer constantly undertake stress, the deformation mode is regardless of applied stresses, even if the loading amount becomes larger, the unit cell deformation patterns maintain a specific mode and last until a specific range then the first layer is the only layer deforms which can be observed more clearly through figures below.

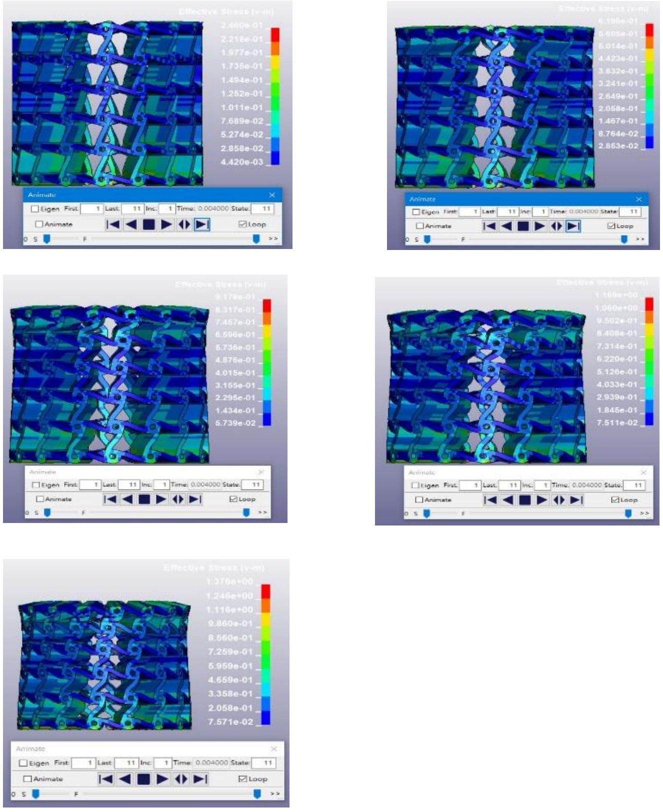

Fig. 8. Schemes of the tetrachiral structure under (a)277 mm/s (b) 833 mm/s (c) 1388 mm/s (d) 1944 mm/s (e) 2500 mm/s velocity loading.

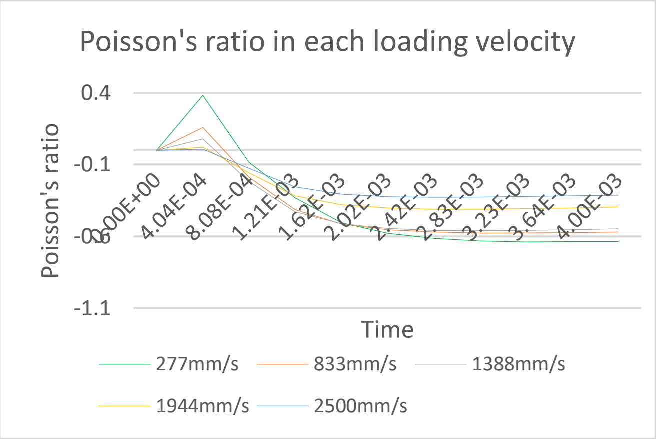

Fig. 9. Poisson's ratio in each loading velocity during impact.

As Fig. 9 shows, tetrachiral structure performs positive Poisson's ratio at the initial time frame no matter how large the loading is, which indicates tetrachiral structure requires a certain amount of loading to bend the longitudinal struts which leads the bulking structure contracts to the central part. Furthermore, according to its horizontal deformation data, the tetrachiral structure obtains a limitation of NPR behaviour. Once the loading reaches critical speed, unit cells are hindered and stop shrinking. At this moment, the bulking mode starts expanding rather than contracting as shown in Fig. 10.

Fig. 10. Scheme of tetrachiral structure with expending layer.

IV. *CONCLUSION REMARKS*

In this study, two auxetic tubular structures with different unit cell structures are made to simulate the mechanical behaviour that occurs under different compulsive loading conditions. The same parameter and same loading velocities are applied to investigate the kinematics of the structures.

a) Both re-entrant and tetrachiral structures are complying with the in-plane mechanical behaviours that have been studied when the specimens endure lower-speed impulsive loadings.

b) An explicit difference of deformation mode occurs when the re-entrant structure bearing a loading velocity exceeds 1944 mm/s, as for tetrachiral structure, the lower parts stop to deform in the horizontal direction.

c) NPR behaviour of re-entrant structure displays worse due to the abnormal deformation of the unit cell which leads to the expansion of the central part when the loading speed exceeds the limitation that the structure can accept.

d) NPR behaviour of the tetrachiral structure performs of poorer quality because of the stationary horizontal deformation of the lower parts and the longitudinal deformation deforms constantly. When the tetrachiral structure bears excessive loading speed, the deformation mode is opposite to the re-entrant structure, when the loading speed occurs too large, the bulking structure expands the top and bottom layer rather than the central part.

The auxetic tubular structure exhibits a distinct mechanical behaviour compared to the beam shape or other researched papers, the results show a good NPR behaviour when the auxetic structures sustain loadings, though the NPR behaviour decreases when the loadings increase, it is possible to improve the performance of the auxetic tubular structure through the thickness or radius of the bulking structure.

ACKNOWLEDGMENTS

This work was supported by Gebze Technical University and Akim Metal Sanayi ve Ticaret A.Ş.

REFERENCES

[1] K. E.Evans, "Auxetic polymers: a new range of materials,"

Endeavour, vol. 15, no. 4, pp. 170–174, Jan.1991.

[2] M.Mir, M. N.Ali, J.Sami, andU.Ansari, “Review of Mechanics and Applications of Auxetic Structures,” vol. 2014, pp. 1–18, 2014.

[3] C.Santulli andC.Langella, “Study and development of concepts of auxetic structures in bio-inspired design,” *Int. J. Sustain. Des.*, vol. 3, no. 1, p. 20, 2016.

[4] V. L.Coenen andK. L.Alderson, “Mechanisms of failure in the static indentation resistance of auxetic carbon fibre laminates.”

[5] I. I.Argatov, R.Guinovart-Díaz, andF. J.Sabina, “On local indentation and impact compliance of isotropic auxetic materials from the continuum mechanics viewpoint,” *Int. J. Eng. Sci.*, vol. 54, pp. 42–57, 2012.

[6] J. B.Choi andR. S.Lakes, “Non-linear properties of polymer cellular materials with a negative Poisson’s ratio,” 1992.

[7] K. E.Evans andA.Alderson, “Auxetic materials: Functional materials and structures from lateral thinking!,” *Adv. Mater.*, vol. 12, no. 9, pp. 617–628, 2000.

[8] A.Remennikov, D.Kalubadanage, T.Ngo, P.Mendis, G.Alici, andA.Whittaker, “Development and performance evaluation of large-scale auxetic protective systems for localised impulsive loads,” 2019.

[9] D.Xiao, X.Chen, Y.Li, W.Wu, andD.Fang, “The structure response of sandwich beams with metallic auxetic honeycomb cores under localized impulsive loading-experiments and finite element analysis (a) (b),” *Mater. Des.*, vol. 176, p. 107840, 2019.

[10] I. O. P. C.Series andM.Science, “Auxetics materials : classification , mechanical properties and applications,” 2020.

[11] C. W.Smith, J. N.Grima, andK. E.Evans, “Novel mechanism for generating auxetic behaviour in reticulated foams: Missing rib foam model,” *Acta Mater.*, vol. 48, no. 17, pp. 4349–4356, 2000.

[12] L.Mizzi, K. M.Azzopardi, D.Attard, J. N.Grima, andR.Gatt, “Auxetic metamaterials exhibiting giant negative Poisson’s ratios,” *Phys. Status Solidi - Rapid Res. Lett.*, vol. 9, no. 7, pp. 425–430, 2015.

[13] J. N.Grima andK. E.Evans, “Auxetic behavior from rotating squares,” *J. Mater. Sci. Lett.*, vol. 19, no. 17, pp. 1563–1565, 2000.

[14] A.Alderson andK. L.Alderson, “Auxetic materials,” *Proc. Inst. Mech. Eng. Part G J. Aerosp. Eng.*, vol. 221, no. 4, pp. 565–575, 2007.

[15] B. D.Caddock andK. E.Evans, “Microporous materials with negative Poisson’s ratios. I. Microstructure and mechanical properties,” *J. Phys. D. Appl. Phys.*, vol. 22, no. 12, pp. 1877–1882, 1989.

[16] O.Bouaziz, J. P.Masse, S.Allain, L.Orgéas, andP.Latil, “Compression of crumpled aluminum thin foils and comparison with other cellular materials,” *Mater. Sci. Eng. A*, vol. 570, pp. 1–7, 2013.

[17] M.Schenk andS. D.Guest, “Geometry of Miura-folded metamaterials,” *Proc. Natl. Acad. Sci. U. S. A.*, vol. 110, no. 9, pp. 3276–3281, 2013.

[18] D.Rodney, B.Gadot, O. R.Martinez, S. R.DuRoscoat, andL.Orgéas, “Reversible dilatancy in entangled single-wire materials,” *Nat. Mater.*, vol. 15, no. 1, pp. 72–77, 2016.

[19] M.Shokri Rad, Y.Prawoto, andZ.Ahmad, “Analytical solution and finite element approach to the 3D re-entrant structures of auxetic materials,” *Mech. Mater.*, vol. 74, pp. 76–87, 2014.

[20] and R. S. L.Chan Soo Ha, Michael E. Plesha, “Physica Status Solidi b - 2016 - Ha - Chiral three-dimensional isotropic lattices with negative Poisson s ratio.pdf.” .

[21] L. J.Gibson andM. F.Ashby, “The mechanics cellular materials of three-dimensional cellular materials,” *Proc. R. Soc. L.*, vol. A382, pp. 43–59, 1982.

[22] Z.Chen, X.Wu, Y.Min, Z.Wang, andS.Zhou, “International Journal of Mechanical Sciences Re -entrant auxetic lattices with enhanced stiffness : A numerical study,” *Int. J. Mech. Sci.*, vol. 178, no. December 2019, p. 105619, 2020.

[23] H.Wang, Z.Lu, Z.Yang, andX.Li, “A novel re-entrant auxetic honeycomb with enhanced in-plane impact resistance,” *Compos. Struct.*, vol. 208, no. May 2018, pp. 758–770, 2019.

[24] K.Cai, J.Luo, Y.Ling, J.Wan, andQ.Qin, “Effects of size and surface on the auxetic behaviour of monolayer graphene kirigami,” *Nat. Publ. Gr.*, pp. 1–10, 2016.

[25] K.Meena andS.Singamneni, “A new auxetic structure with significantly reduced stress concentration effects,” *Mater. Des.*, vol. 173, p. 107779, 2019.

[26] Z.Dong, Y.Li, T.Zhao, W.Wu, D.Xiao, andJ.Liang, “Experimental and numerical studies on the compressive mechanical properties of the metallic auxetic reentrant honeycomb,” vol. 182, 2019.

[27] W.Wu, W.Hu, G.Qian, H.Liao, X.Xu, andF.Berto, “Mechanical design and multifunctional applications of chiral mechanical metamaterials : A review,” *Mater. Des.*, vol. 180, no. June, p. 107950, 2019.

[28] K. W.Wojciechowski, “Two-dimensional isotropic system with a negative poisson ratio,” *Phys. Lett. A*, vol. 137, no. 1–2, pp. 60–64, May1989.

[29] A.Alderson *et al.*, “Elastic constants of 3-, 4- and 6-connected chiral and anti-chiral honeycombs subject to uniaxial in-plane loading,” *Compos. Sci. Technol.*, vol. 70, no. 7, pp. 1042–1048, 2010.

[30] C.Qi, F.Jiang, C.Yu, andS.Yang, “International Journal of Impact Engineering In-plane crushing response of tetra-chiral honeycombs,” *Int. J. Impact Eng.*, vol. 130, no. December 2018, pp. 247–265, 2019.

[31] X.Ren, J.Shen, A.Ghaedizadeh, H.Tian, andY. M.Xie, “A simple auxetic tubular structure with tuneable mechanical properties,” *Smart Mater. Struct.*, vol. 25, no. 6, 2016.

The effect of particle type on wear and corrosion behaviour of MAO coatings on AZ31 alloy

Abubaker Ibrahım ELSADAWI and Fatih AYDIN[1]

Department of Metallurgical and Materials Engineering, Karabuk University, Karabuk, TURKEY

*Corresponding author: fatih.aydin@karabuk.edu.tr

ABSTRACT

The micro-arc oxidation is widely used to improve the wear and corrosion performance of magnesium alloys. In this study, the surface layers were formed by micro-arc oxidation in the electrolyte containing nano-sized particles of TiO_2, TiC and TiN. The surface morphology, phase analysis and chemical composition of the coatings were examined by Scanning electron microscopy, Fourier transform infrared spectroscopy, X-ray diffraction, X-ray photoelectron spectroscopy and Raman analyses. It was seen that the pore size and diameter of the coatings reduced with the addition of nanoparticles. The wear performance of the samples was studied by reciprocating wear tests under different loads for dry sliding conditions. The electrochemical corrosion performance (potentiodynamic polarization and electrochemical impedance spectroscopy) was also studied in 3.5 wt.% NaCl solution. The worn and corroded surfaces were investigated by SEM to reveal dominant failure mechanisms. As a result, the nanoparticle providing the best performance was determined.

Keywords: AZ31 alloy, wear, corrosion, micro-arc oxidation

ACKNOWLEDGMENT

This work was financially supported by the Scientific Research Projects Coordination Unit of Karabük University, Project Number: KBÜBAP-21-YL-087

Wear Rate of Aged Mg-2.5Al-1.0Sn-0.3Mn-0.4La-0.66Gd Alloy

Esra Özsoy*, İsmail Hakkı Kara+

* *Metallurgy and Materials Engineering Department, Karabük University*
Karabük, Turkey
esra_ozsoy1998@hotmail.com

+*Metallurgy and Materials Engineering Department, Karabük University*
Karabük, Turkey
ihakkikara@karabuk.edu.tr

Abstract— **The hazardous greenhouse gases are the extreme threat around the world originated from mainly automotive and aerospace like vehicles consuming fossil fuel. The lightweight metals can be the best choice for restricting the unhealthy gases emissions. Mg-Al-Sn (AT) base Mg alloy is a candidate for solving the mentioned threat due to their low density (1.74 g/cm^3) and excellent specific strength (strength/density). This study targeted the development of the AT31 Mg alloys room temperature wear properties by using the light Lanthanum (La) and Gadolinium (Gd) elements. Aging heat treatment has been exposed at 200°C during 2,4,6 and 8 hours. The wear tests were applied at 25°C temperature. Three different loads (10,20 and 30 N) have been applied to obtain the wear behavior of investigated specimens.**

Keywords— **Mg-Al-Sn (AT), La, Gd, Wear, Aging.**

I. INTRODUCTION

Recently, magnesium (Mg) alloys are increasingly being used in the automotive, aerospace, and electronic and energy industries because of their low density, high specific strength-stiffness, and castability [1]. The AT(Mg-Al-Sn) series mostly is utilized in industry, although the elevated temperature applications of AT series were inhibited that could relate to the poor wear properties at room temperatures [2]. Because the Mg17Al12 type secondary phase is coarsening during high temperature wherein the solving of this difficulty was suggested as fully removing the Mg17Al12 secondary phase from the matrix or reducing the volume fraction of it [3]. The rare earth elements (REEs) are known as the suppressing formation of Mg17Al12 phase and they positively affect the mechanical properties and corrosion resistance of Mg alloys wherein the stable Al11Re3 type secondary phases were introduced to diminish the Mg17Al12 phase or removing all of them from matrix [3]. Moreover, it is reported that Lanthanum (La) suppress the Mg17Al12 phase formation by replaced the highly stable Al11La3 phase that results from the solubility of La in Mg is low in this way La including secondary phases introduce in matrix [4]. Further, the La was used to improve the mechanical properties or corrosion resistance of Mg alloys like Mg-Zn, Mg-Zn-Al [5]. Nevertheless, the systematic approach by adding the amount in the range of 0.4La+0.66 Gd wt.% is needing for learn how the effect of the La and Gd amount on wear properties both at room temperature at room temperature of AT31 Mg alloys. The aim of this study is to investigate the critical La and Gd amount to clarify the effect on wear properties at room temperature of AT31 Mg alloys.

II. EXPERIMENTAL STUDIES

Experimental materials were prepared in an electric resistance furnace under protection of Ar gas. Pure Mg, Al and Zn metals and Mg-30wt%La and Mg-10wt%Mn master alloys were melted at 775°C. The melted alloys were injected into the steel mold with a temperature of 350°C in low 2-3 atm pressure under protection CO2+1vol% SF6 mixed gas. Chemical compositions of alloys were determined by X-ray fluorescence (XRF- Machine: Rigaku ZSX Primus II) and were obtained as Mg-2.5Al-1.0Sn-0.3Mn-0.4La-0.66Gd. The homogenization treatment was conducted at 350°C for 12 hours. Aging heat treatment has been employed at 200°C during 2,4,6 and 8 hours.

According to ASTM G-133 standard, reciprocating wear tests (UTS-Tribometer Tester) in a dry environment were performed under 1,2 and 3 kg loads. The stroke distance of 8mm was adjusted and the samples were subjected to the abrasion test for a total of 100 m. The volumetric loss after wear was determined using a profilometer device. Five measurements were taken from each sample in the direction perpendicular to the wear track. The amount of eroded volume was found by multiplying the 2D dimensional profilometer curves with the total trace length [6].

III. RESULTS

The dry wear test results are given in Fig.1 and Table 1. As to applied load, the wear rate of specimens is similar for all, where the rising of load resulted in decreasing of wear rate. However, the lowest wear rate has been obtained with the specimen of 2 hours aged one under 10N load. The rising of applied loads changed the lowest wear rate to 4 hours specimen.

Table 1. The wear rate values of specimens (mm³/N.m).

Aging Time	10N	20N	30N
2	0,001656	0,001270	0,001036
4	0,001676	0,001054	0,000940
6	0,002060	0,001328	0,001065
8	0,001836	0,001186	0,000984

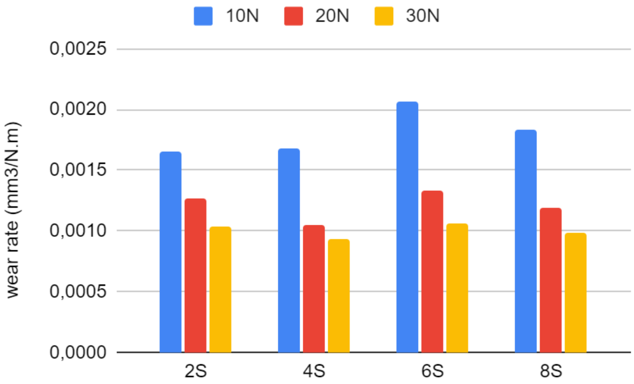

Fig.1. The wear results of specimens.

ACKNOWLEDGMENT

This work was financially supported by the Scientific Research Projects Coordination Unit of Karabük University, Project Number: KBÜBAP-22-YL-014

REFERENCES

[1] İ. H. Kara, H. Ahlatcı, Y. Türen ve Y. Sun, «Microstructure and corrosion properties of lanthanum-added AZ31 Mg alloys,» *Arabian Journal of Geosciences,* cilt 11, p. 535, 2018.

[2] I. Kara ve A. Incesu, «Microstructural, Mechanical, and Tribological Properties of Mg-3Al-1Sn-1Nd-Mn Alloy,» *Journal of Materials Engineering and Performance* , cilt 30, pp. 1674-1682, 2021.

[3] A. Prasad, Y. Chiu, S. Singh, N. Gosvami ve J. Jain, «Role of La addition for enhancing the corrosion resistance of Mg–Dy alloy,» *The International Journal of Corrosion Processes and Corrosion Control,* cilt 56, no. 6, pp. 575-583 , 2021.

[4] A. Kumar, G. Meenashisundaram, V. Manakari, G. Parande ve M. Gupta, «Lanthanum effect on improving CTE, damping, hardness and tensile response of Mg-3Al alloy,» *Journal of Alloys and Compounds,* cilt 695, pp. 3612-3620, 2017.

[5] C. Wang, L. Zeng, W. Ding ve T. Liang, «ffects of minor RE (Y, La) on microstructure and corrosion behavior of TX31 alloys,» *J. Mater. Res. Technol.,* cilt 14, pp. 69-80, 2021.

[6] ASTM, Evaluation of Wear Testing, San Francisco: American Society for Testing and Materials, 1968.

Wear Behavior of Homogenized Mg-2.5Al-1.0Sn-0.3Mn-0.4La-0.66Gd Mg Alloy

İsmail Hakkı KARA*

* *Metallurgy and Materials Engineering Department, Karabük University*
Karabük, Turkey
ihakkikara@karabuk.edu.tr

***Abstract*— Interest in magnesium alloys is increasing day by day. The most important reason for this is the low density and high special strengths of magnesium alloys. However, the use of magnesium alloys is very limited. Poor wear performance reduces the use of magnesium products. Alloying is a preferred method to increase the wear resistance of magnesium alloys. In recent years, rare earth elements have been used as alloying elements in magnesium alloys, and as a result, both mechanical properties and corrosion resistance have been improved. Mg17Al12 secondary phase in the Mg-Al binary system has found a wide usage area due to its contribution to strength and corrosion. In this study, Mg-2.5Al-1.0Sn-0.3Mn-0.4La-0.66Gd alloys were produced using an induction melting casting method. After casting, homogenization heat treatment was applied at 350°C for 4,8, and 12 hours. Microstructure of homogenized alloys examined by using light optical microscopy (LOM) and EDS-assisted scanning electron microscopy (SEM). Dry wear test carried out by reciprocating wear at 25°C with the load of 1kg, 2kg, and 3kg according to ASTM-G133. The hardness measurement of the samples was made according to the Brinell method using a universal hardness device (2.5 mm diameter steel ball, 187.5 kg load - 10 sec. dwell time).**

***Keywords*— Mg-Al-Sn- La-Gd, Microstructure, Wear, Homogenization.**

I. INTRODUCTION

Interest in magnesium alloys is increasing day by day. The most important reason for this is the low density and high special strengths of magnesium alloys [1]. However, the use of magnesium alloys is very limited [2]. Poor wear performance reduces the use of magnesium products. Alloying is a preferred method to increase the wear resistance of magnesium alloys. In recent years, rare earth elements have been used as alloying elements in magnesium alloys, and as a result, both mechanical properties and corrosion resistance have been improved. Mg17Al12 secondary phase in the Mg-Al binary system has found a wide usage area due to its contribution to strength and corrosion [3]. but the Mg17Al12 phase is unstable at high temperatures. Tin was added to obtain a phase resistant to high temperatures and positive results were obtained. High temperature strength and creep studies focused on Mg-Al-Sn alloy. However, studies on rare earth element added Mg-Al-Sn alloys are very scarce [4]. The corrosion resistance of lanthanum added magnesium alloys is quite good [5]. The addition of gadolinium improves the strength properties of magnesium alloys [6]. Especially in the literature, there is almost no study on the wear resistance of La and Gd modified Mg-Al-Sn alloys.

In this study, Mg-2.5Al-1.0Sn-0.4La-0.66Gd alloy was produced by low pressure permanent mold casting technique. Then homogenization heat treatment was applied at 350°C for 4, 8 and 12 hours. Hardness measurements were made from the samples using the Brinell hardness method. Dry wear test carried out by reciprocating wear at 25°C with the load of 1kg, 2kg, and 3kg. The effect of homogenization heat treatment on microstructure was investigated by LOM, SEM and XRD methods. The wear mechanisms of the alloys, whose wear rates are compared, depending on the changing load were investigated.

II. EXPERIMENTAL STUDIES

Mg-2.5Al-1.0Sn-0.3Mn-0.4La-0.66Gd alloy was produced by low pressure die casting (LPDC) method using an electric resistance furnace. Pure Mg, Al and Sn were first loaded into the furnace. Mg-Mn, Mg-La and Mg-Gd master alloys were added to the materials melted at 750 °C for 1 hour. 1-2 atm. into stainless steel molds preheated to 350 °C. The molten metal was injected by means of pressure. The chemical composition of the produced alloy (2.5%Al, 1.0%Sn, 0.3%Mn, 0.4%La and 0.66% Gd remaining Mg (wt.)) was determined by XRF device. Samples with dimensions of 10x10x10 mm were subjected to homogenization heat treatment in a heat treatment furnace at 350 °C for 4, 8 and 12 hours. Expired samples were cooled by quenching. Before microstructural characterization, sanding (600-2500 grit), polishing (1µm diamond suspension) and etching (picral) processes were performed and metallographic processes were completed. Optical microscopes (LOM- Carl Zeiss light optical microscope) and electron microscope (Carl Zeiss Ultra Plus scanning electron microscope) were used to reveal the change of grains and secondary phases, respectively. XRD was used to identify the secondary phases. Average grain sizes were calculated from optical microscope images according to ASTM E112 standard. According to ASTM G-133 standard, back and forth wear tests (UTS-Tribometer Tester) in a dry environment were performed under 1,2 and 3 kg loads. The stroke distance of 13 mm was adjusted and the samples were subjected to the abrasion test for a total of 100 m. The volumetric loss after wear was determined using a profilometer device. Five measurements were taken from each sample in the direction perpendicular to the wear track. The amount of eroded volume was found by multiplying the 2D dimensional profilometer curves with the total trace length [7].After the wear test, the changing alloy element amount and the wear mechanism depending on the wear load were found using EDX (energy distribution X-ray spectrometry) supported SEM device. The hardness measurement of the samples was made according to the Brinell method using a universal hardness device (2.5 mm diameter steel ball, 187.5 kg load - 10 sec. dwell time).

III. RESULTS

Fig. 1 demonstrates the LOM micrographs of homogenized Mg-2.5Al-1.0Sn-0.4La-0.66Gd specimens. The non homogenous equiaxed grains were characterized after homogenization heat treatment. However, the average grain size was measured by different values of 42, 33 and 27μm for 4, 8 and 12 hours duration of Mg-2.5Al-1.0Sn-0.4La-0.66Gd alloy, respectively.

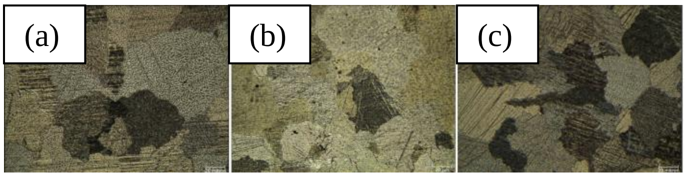

Fig.1. The LOM micrographs of homogenized specimens for a)4h, b)8h and c)12h.

Fig.2 illustrates the SEM micrographs of Mg-2.5Al-1.0Sn-0.4La-0.66Gd specimens which were homogenized during 4, 8 and 12 hours at 350°C. The SEM images enable to see secondary phases containing oval, acicular and complex shapes. Oval secondary phases were introduced on the microstructure of all specimens. However, the size of them is altered when the duration of homogenization is changed. The 4 hours homogenized sample includes finer sized oval secondary phases (4.2μm) that distributed homogeneously on the microstructure. Moreover, the thin short acicular secondary phases were placed in different locations of 4 hours homogenized sample. When the duration is 8 hours, the coarse oval (2.7μm) and longer and thicker acicular secondary phases occupy the microstructure densely. However, the 12 hours homogenization time influenced the acicular secondary phases which were observed as thinner but as well as longer.

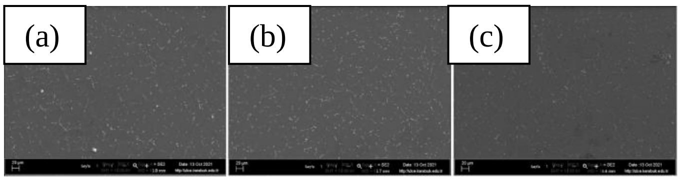

Fig.2. The SEM micrographs of homogenized specimens for a)4h, b)8h and c)12h.

Fig. 3 shows the HBW values of homogenized Mg-2.5Al-1.0Sn-0.4La-0.66Gd specimens. The lowest hardness is obtained at 4 hours homogenized specimen as 51.8 HBW. 8 hours homogenized specimen is following the 4 hours one with the 52.1 HBW value. The highest hardness is measured as 54.6 HBW in 12 hours homogenized specimen. The hardness properties of investigated specimens is different based on the microstructure properties such as average grain size or secondary size types. As seen from hardness results and SEM micrographs, the size of secondary phases is influenced by the hardness values, where coarse and thicker ones imparted to lower hardness. However, the finer size oval shaped and short acicular type secondary phases give rise to highest hardness values.

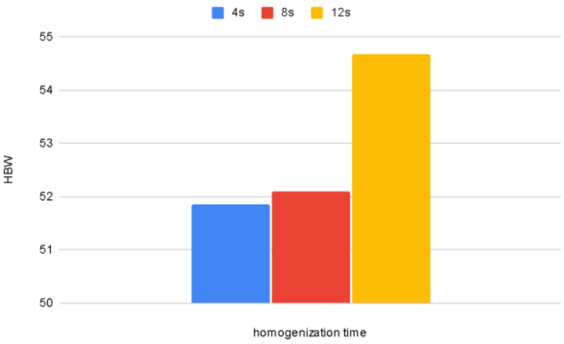

Fig.3. The Brinell Hardness values of homogenized specimens for a)4h, b)8h and c)12h.

Dry wear test was performed at room temperature and under load of 1kg, 2kg and 3kg, and volumetric losses for samples applied with different homogenization times are given in Fig.4. The metal loss values of investigated specimens is not confirmed with the hardness values in 1 kg load, where the highest metal loss was obtained by 12 hours homogenized specimen followed by 8 and 4 hours with decreased values. This is probably the secondary phase that demonstrated that the matrix was collected by a steel ball thus resulting in more metal loss [8]. 2 kg and 3 kg loads conditions give rise to close similarity with 4 and 8 hours homogenized specimens which showed hardness values of 51.8 and 52.1 HBW, respectively. However, the 12 hours homogenized specimen imparted the highest metal loss at 2 kg load and the intermediate value at 3 kg load. The reason probably was obtained by occurring difference wear mechanisms which enable to diverse wear behavior during wear test [1].

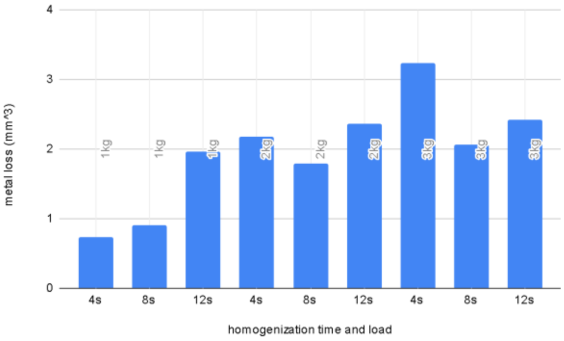

Fig.4. Metal loss of homogenized specimens for a)4h, b)8h and c)12h at 1,2 and 3 kg loads.

IV. CONCLUSIONS

The metal loss of homogenized Mg-2.5Al-1.0Sn-0.4La-0.66Gd alloy is diverse based on the homogenization time, where different type secondary phases and grains were formed. The hardness and wear resistance of studied specimens is not confirm due to probably different wear mechanisms such as oxidation, abrasive and delamination during wear test.

REFERENCES

[1] Z. A., G. H.M. ve M. R., «Effect of rare earth elements addition on the tribological behavior of AZ91D magnesium alloy at elevated temperatures,» Wear, cilt 303, no. 1-2, pp. 98-108, 2013.

[2] H. Çuğ ve H. Ahlatçı, «Effect of Zn and Mn Additions on the Wear Resistance of Cast Alloy Mg–5% Al–1% Si,» Metal Science and Heat Treatment, cilt 59, no. 3-4, pp. 161-167, 2017.

[3] E. Ilanaganar ve S. Anbuselvan, «Wear mechanisms of AZ31B magnesium alloy during dry sliding condition,» Materials Today: Proceedings , cilt 5, pp. 628-635, 2018.

[4] Y. Türen, «Effect of Sn addition on microstructure, mechanical and casting properties of AZ91 alloy,» Materials & Design, cilt 49, pp. 1009-1015, 2013.

[5] A. Kumar, G. Meenashisundaram, V. Manakari, G. Parande ve M. Gupta, «Lanthanum effect on improving CTE, damping, hardness and tensile response of Mg-3Al alloy,» Journal of Alloys and Compounds, cilt 695, pp. 3612-3620, 2017.

[6] R. Arrabal, E. Matykina, A. Pardo, M. Merino, K. Paucar, M. Mohedano ve P. Casajús, «Corrosion behaviour of AZ91D and AM50 magnesium alloys with Nd and Gd additions in humid environments,» Corrosion Science, cilt 55, pp. 351-362, 2012.

[7] ASTM, Evaluation of Wear Testing, San Francisco: American Society for Testing and Materials, 1968.

[8] M. Nouri, X. Sun ve D. Li, «Beneficial effects of yttrium on the performance of Mg–3%Al alloy during wear, corrosion and corrosive wear,» cilt 67, pp. 154-163, 2013.

POLYPROPYLENE MATRIX E-GLASS REINFORCED THERMOPLASTIC COMPOSITES AS AN ALTERNATIVE MATERIAL FOR LIGHT WEIGHT APPLICATIONS

H. Konbul*, A. Altınbay Bekem*, A. Unal*

Department of Metallurgical and Materials Engineering, Yildiz Technical University Davutpasa, Istanbul, Turkey

hkonbul@gmail.com, abekem@yildiz.edu.tr, ahunal@yildiz.edu.tr

***Abstract*—Thermoplastics composites usage is increasing day by day because its low production cycle, easy to storage, low cost and reusable features. In this study, E-glass/PP prepreg laminates were tested to search an alternative other thermoplastics which using aircraft industry.**

***Keywords*— Polypropylene composites, PP/E-glass prepregs, mechanical characterization**

I. INTRODUCTION

Polypropylene (PP) is the third largest polyolefin material by volume and is one of the largest plastic families in the world [1]. It has one of the lowest density of all thermoplastics. This condition also, combined with strength, hardness and excellent fatigue and chemical resistance properties make this material attractive for many situations. [2] On the other hand, glass fibre has been used both in the past and today in high performance applications such as non-structural areas in aircraft, rocket engine cases and pressure vessels, due to its affordability, high strength, and ease of processing. The most widely used fiberglass is known as E-glass, a fiberglass that has a beneficial balance of mechanical, chemical and electrical properties at a very reasonable cost. [3]

Thermoplastic composites first entered the aviation world with semi-crystalline PEEK in the 1980s. This initiative was followed by PEI in the 1990s, PPS in the late 1990s, and PEKK in 2005. PEEK, PEI, PPS, PEKK and PAEK widely used in aviation industry and their properties shown in Table I.

TABLE I
AVIATION TERMOPLASTICS AND THEIR PROPERTIES [4] [5], [6], [7], [8]

	PEEK	**PEI**	**PPS**	**PEKK**
Structure	Crys.	Amorph.	Crys.	Crys.
Mechanical Properties	++	+	+	++
Material Price	-	+	+	o
Melting Temp., ℃	343	310	280	331
Process Temp., ℃	370-400	315	330	380
Glass Transition Temp., ℃	143	210	90	162
Chemical Resistance	+	-	++	+
Adhesion	-	+	-	+
Place of use	Primary structure	Cabin interior	Secondary Structure	Primary structure
Density, g/cm³	1.30	1.27	1.35	1.31

List of Advantages: 0 < - < + < ++

In Table II, the properties of polypropylene resin are given. Although melting and processing temperatures are lower in PP than other aviation thermoplastics, it's density is relatively lower. So this made PP a good candidate for non-structural aircraft parts.

TABLE II
PP RESIN PROPERTIES [9][10][11]

Properties	Values
Melting Temperature, ℃	162 – 165
Process Temperature, ℃	200 – 298
Glass Transition Temperature, ℃	106
Density, g/cm³	0.90

While air transport is increasing day by day, fast production technologies and lighter aircrafts are required to respond to this situation [4]. Based on this situation, compared to the resins which are used in aviation industry, polypropylene has a lower density and a lower processing temperature than others.

On the other hand, galvanic compatibility is very important in aerospace applications. Glass fibre is galvanically compatible with many metals and their surface finishes.

Considering all this information, determined to investigate glass fibre/PP (GFPP) composites because better galvanic compatibility, lower cost and lower density compare with other thermoplastic resins.

In this study, GFPP laminate were produced and mechanical performance was determined via tensile testing. Results were evaluated considering fibre direction.

II. EXPERIMENTAL

A. *Materials*

The GFPP prepregs were provided by Baycomp Inc. The fibre content was measured according to ISO 1172 and determined as ~35 vol%. The prepreg rolls were 165 mm wide. The nominal thickness was 350 µm.

B. *Sample Preparation*

The GFPP prepregs at 165 mm long with 0° and 0°/90° fibre directions were placed in Teflon films. Depending on the stacking sequence of lamina or laminate, stacks were placed in the 165x165 cavity of single or double 0.36 mm Teflon films to prevent the spreading of fibres in the prepreg. Stacks, as seen in Figure 1, were pressed for 5 minutes at 180°C and 80 bar.

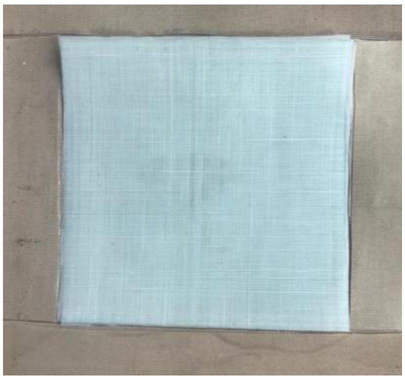

Figure 1. Stacks in the cavity of Teflon films before pressing.

C. *Testing*

Tensile tests were performed according to ISO 527-4 on an Instron 3369. The load cell was 50 kN and the rate applied was 5mm/min. To cut off specimens from lamina/laminate, cutting mould in the shape of dog-bone was used.

Four types of specimens were taken as seen in Figure 2. These were neat prepreg (NP), processed prepreg (PP), cross-ply (CP), angle-ply (AP). At least 5 specimens were tested for each type.

Figure 2. Various types of tensile specimens.

III. RESULTS AND DISCUSSIONS

Fibre volume fractions were determined for all specimens to control if there was any change with processing. However, not a significant change was detected, which proved the processing did not harm the orientation of the prepreg.

Lamina at 0° and laminate at 0°/90° were obtained after pressing as seen in Figure 2. Thanks to the polypropylene matrix being transparent, fibre distribution visually could be observed. It seems that the fibre orientation was homogenous in NP. After the processing, the orientation of fibres in PP seems to be good and there was no distortion in the shape of the specimens. However, some buckling and slight misalignments were also detected. In CP (0/90) laminate (Figure 3.b), curvature distortion was observed. Due to anisotropic structure, 0° and 90° laminas had different linear thermal expansion coefficients, which forced the well-bonded laminate to bend towards the lamina with the lower coefficient of expansion [12]. A similar case was seen AP (±45) laminate, where specimens were taken from CP laminate at 45°. As seen in Figure 3, AP specimens had twisted shapes, again stresses occur due to differences in thermal expansion coefficients. These were inherent results for non-symmetrical laminates that ensure good bonding between laminas.

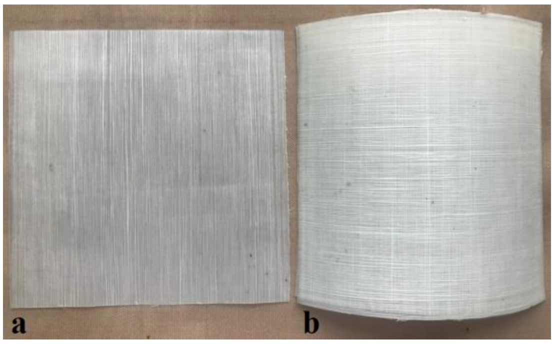

Figure 3. a) 0° lamina, b) 0°/90° laminate after pressing.

Tensile curves for NP, PP, CP and AP were shown in Figure 4-7. Three important results with standard deviations that were calculated from the stress-strain curves were given in Table III. The ultimate tensile stress (UTS) was the peak stress, which could also be called the strength value of the specimens. The strain at which this UTS occurred was "ε at UTS". The third result was the modulus of Elasticity (E), which was regarding the stiffness of composites.

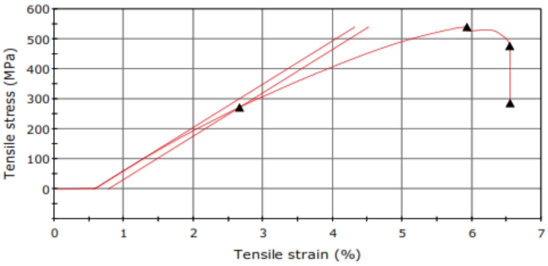

Figure 4. Tensile curve of NP.

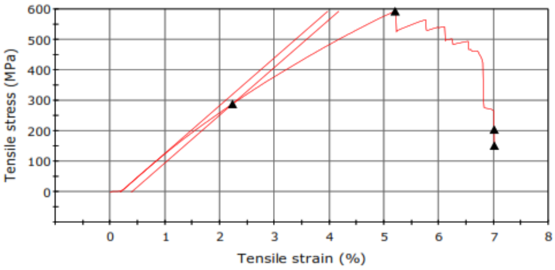

Figure 5. Tensile curve of PP.

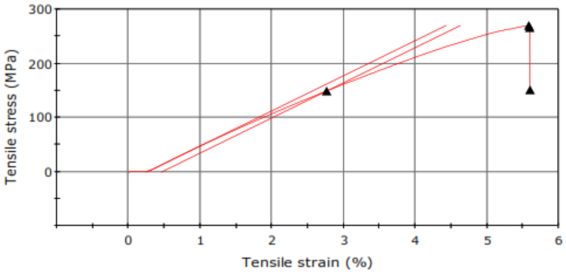

Figure 6. Tensile curve of CP.

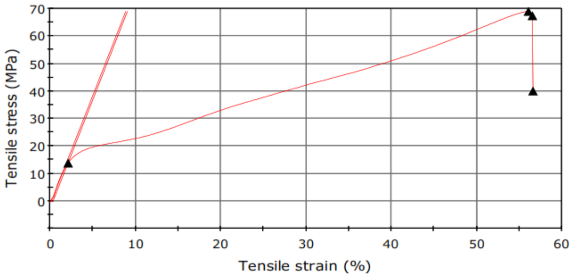

Figure 7. Tensile curve of AP.

All the results of PP were slightly higher than NP, although some disorders in fibre orientation were observed with processing. A higher degree of impregnation had possibly occurred during processing which caused improvement in fibre/matrix bonding. The strength and modulus were decreased significantly in CP because the half-section consisted of non-loading carrier 90° fibres. That is why strength decreased to almost half. However, the decrease in strain values was not high as other results which was an indicator of well-bonding between fibre and matrix. A sharp decline in strength and stiffness was seen in AP, while an extensive strain increase occurred.

TABLE III
TENSILE TEST RESULTS

	UTS (MPa)	ε at UTS (%)	E (GPa)
NP	472.12±44.81	5.10±0.62	14.38±0.28
PP	532.53±61.23	5.37±1.53	14.61±4.12
CP	245.54±17.12	4.97±0.43	6.49±0.22
AP	72.18±3.68	54.93±3.09	0.88±0.12

The fracture in NP and PP occurs gradually. As seen in Figure 4 and 5, specimens continued to elongate after UTS. However, some of the fibre bundles had already been damaged. At the final fracture, a multi-partial fracture was observed in these samples For CP and AP, the tensile stress drops vertically after the UTS has been reached and a two-piece fracture was obtained in both types. The fracture was realized at 90° in CP, while it was at ±45° in AP. Also, huge elongation was observed in AP. The final appearance for each type of specimen were seen in Figure 8.

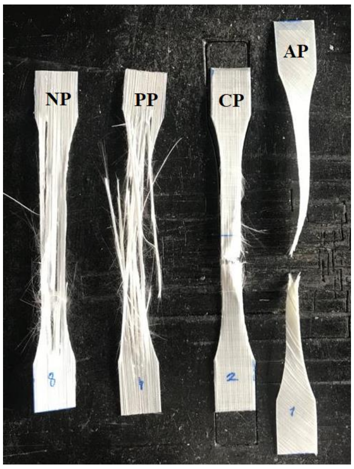

Figure 8. Various types of specimens after test.

IV. CONCLUSIONS

The aim of the study was to research and develop a cheap alternative with high galvanic compatibility to most used thermoplastics. With this aim, GFPP is a good candidate with moderate performance, lower density and lower price. In this study, mechanical performance via tensile testing of various lamina and laminate was determined. As received prepreg was first tested as a single unidirectional lamina and it was compared with processed lamina to see whether processing damaged the structure. Although some misalignment was observed on fibres, better results were taken from the processed lamina. Then 0/90 cross-ply and ±45 angle-ply were produced to examine the directional behaviour of laminate. As expected, UTS and modulus decreased almost to half in CP, and the maximum decline was obtained in AP. However, a significant increase in elongation was seen in AP, which gains in toughness and ductility.

REFERENCES

[1] J. R. Fried, Polymer Science and Technology. Upper Saddle River, NJ: Prentice Hall, 2014.
[2] Crawford, R.J. (Roy J.), (1998). Plastics engineering, Third Edition, Butterworth-Heinemann, Suffolk
[3] ASM Handbook Volume 21: Composites - ASM International, 2021
[4] Özel D, Temiz AS (2018) An overview of thermoplastic composites from the world of aviation. pp. 1-19.
[5] "Peek 1000 technical properties data sheet - theplasticshop." [Online]. Available: https://www.theplasticshop.co.uk/plastic_technical_data_sheets/peek_1000_technical_data_sheet.pdf. [Accessed: 20-Feb-2022].
[6] "Polyetherimide PEI 1000 Technical Properties Data Sheet-theplasticshop."[Online]. Available: https://www.theplasticshop.co.uk/plastic_technical_data_sheets/polyetherimide_pei_1000_technical_data_sheet.pdf [Accessed: 20-Feb-2022].
[7] Polyphenylene sulphide (PPS). [Online]. Available: https://www.plastena.lv/en/engineering-plastics-for-industry-polyphenylene-sulfide-pps. [Accessed: 20-Feb-2022].

[8] "The Online Materials Information Resource," MatWeb. [Online]. Available: http://www.matweb.com/search/datasheet.aspx?matguid=1bdfd4b5a72143c680ba1e94390ac844&ckck=1. [Accessed: 20-Feb-2022].

[9] D. Nwabunma and T. Kyu, Polyolefin composites. Hoboken: Wiley-Interscience, 2008.

[10] J. Grebowicz, S.-F. Lau, and B. Wunderlich, "The thermal properties of polypropylene," Journal of Polymer Science: Polymer Symposia, vol. 71, no. 1, pp. 19–37, 2007.

[11] "Polypropylene Processing Guide," [Online]. Available: https://www.ineos.com/globalassets/ineos-group/businesses/ineosolefins-and-polymers-usa/products/technical-information-patents/ineos_polypropylene_processing_guide.pdf [Accessed: 20-Feb-2022].

[12] D. Hull, An Introduction to Composite Materials, Cambriidge University Press, 1981.

CORROSION PERFORMANCE OF CHROMIUM (III) COATED ON AA2024 USED IN AEROSPACE INDUSTRY

Cansel PEHLİVANOĞLU[1], Mustafa Özgür ÖTEYAKA[2], Emir Zafer HOŞGÜN[1]

1 Department of Chemical Engineering, Eskişehir Technical University
2 Eskişehir Vocational School, Eskisehir Osmangazi University, Eskişehir, Turkey

Abstract

The aluminum alloy AA2024-T3 was widely employed in the aerospace industry because of its lightweight, good mechanical properties, and corrosion properties. To enhance the corrosion properties of aluminum alloy, the chromium (VI) coating conversion was applied to the surface of produced parts. However, the toxicity of the chromium (VI) limit their usage and chromium (III) conversion began to replace the previous coating. In this study, the AA202-T3 was coated with both coating Cr^{+3} and Cr^{+6}, and their corrosion performance were evaluated in the 3.5 wt % NaCl solution. For this purpose, electrochemical tests such as free corrosion potential measurement, potentiodynamic test, and electrochemical impedance spectroscopy (EIS). The findings showed that a passivation zone and the protective zone finished around at – 500 mV were observed for all samples. However, the corrosion potential measured was -1000 mV for Cr^{+3} coated sample which was more anodic compared to Cr^{+6} and the original sample. Moreover, the free corrosion potential behavior also confirmed that the Cr^{+3} coating was more anodic compared to other samples after 1 h of immersion. On the other hand, the EIS analysis showed that the uncoated sample had higher impedance resistance compared to coated samples followed by Cr^{+3} with double semi-circle and Cr^{+6}.

Keywords: Aluminum alloy, AA2024, Chromium (III) coating, Corrosion.

Production and morphological investigation of Al6xxx-10Bi-3Mn alloy

Bünyamin ÇİÇEK*

* *Hitit University*
Technical Sciences School, Corum. Turkey
cicekbunyamin78@gmail.com

***Abstract*— In this study, an alloying was done in vacuum arc melting furnace. For the Al6xxx-10Bi-3Mn ternary alloy, the powder materials were subjected to a basic mixing process. After a simple pressing, the powders held together were melted 4 times in a mini arc furnace. After solidification, homogenization heat treatment was applied. Microstructural analysis was performed on the obtained sample under a scanning electron microscope (SEM). Energy Dispersive X-Ray (EDX) was applied to different phase regions detected in the sample and their elemental ratios were determined. As a result, the production and basic microstructural evolution of an Aluminium alloy with a different production method were investigated.**

***Keywords*— Aluminium, bismuth, manganese, alloy, arc melting.**

I. INTRODUCTION

Aluminium; it is a metal that is frequently used in applications where lightness is important. It is an indispensable element for tribology, mechanical and corrosive industries. However, when Al is used purely, it cannot show sufficient experimental resistances. Therefore, it gives better results as a result of alloying with some elements. In addition, it gives very successful experimental results with Mg, Si, Zn and Mn elements [1-4].

Considering its surface central cubic atomic structure, Al can form solid solutions with many elements. Thus, the matrix can be found in the secondary phases as well as the Al phase. β phases can be formed by providing sufficient amount of elements at the atomic level. Experimental resistances improve with intermetallic phases formed after alloying. In addition to binary alloy groups, ternary alloy groups are also frequently used. Thus, the structure becomes more usable with the help of secondary phases formed as a result of alloying [1, 5-7].

In this study, Al6xxx-10Bi-3Mn ternary alloy was prepared in a mini arc furnace. Besides the production details, the basic microstructure of the alloy was taken with the help of SEM. The elemental balances of the observed phases were examined by EDX analysis. As a result, an Al-Bi-Mn ternary alloy with α-β phase equilibrium was obtained.

II. MATERIALS AND METHODS

SEM images of the powders used in the alloying process under 100 microns and with a purity of 99.5% are given in Figure 1. Al, Mg, Si elements were used for Al6xxx alloy and Bi and Mn elements were used for this study. The powders were first prepared as a total of 5 g. The powders were mixed for 5 minutes in a mini-cabinet with a simple rotational motion. It was subjected to basic compression at a load of 20 MPa/mm^2 under a 16 mm diameter press.

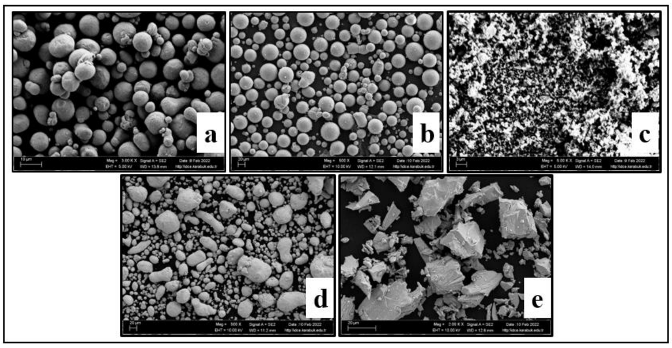

Fig. 1. Basic powder metals;
(a) Al, (b) Mg, (c) Si, (d) Bi, and (e) Mn

The powders compressed in the Buhler Arc Melting MAM-1 arc furnace (Figure 2) were subjected to repeat melting at least 4 times. Before the process, the arc chamber was vacuumed and melting was done in an Ar gas atmosphere. After solidification, homogenization heat treatment was applied to the sample at 350C/12h conditions.

After the classical metallographic preparation after the heat treatment, the sample was examined in the SEM device. EDX analysis of the phases was performed on the obtained microstructure. For the Al6xxx+10Bi+3Mn alloy, the pre-production wt% ratios are given in Table 1.

Table 1. Elements rate pre-production

Al6xxx	**Si**	**Mg**	**Bi**	**Mn**	**Al**
% wt	0,6	1,1	10	3	balance

Fig. 2 Mini arc melting furnace

III. RESULTS AND DISCUSSIONS

The basic SEM microstructure obtained from the Al6xxx-10Bi-3Mn ternary alloy is given in Figure 3.

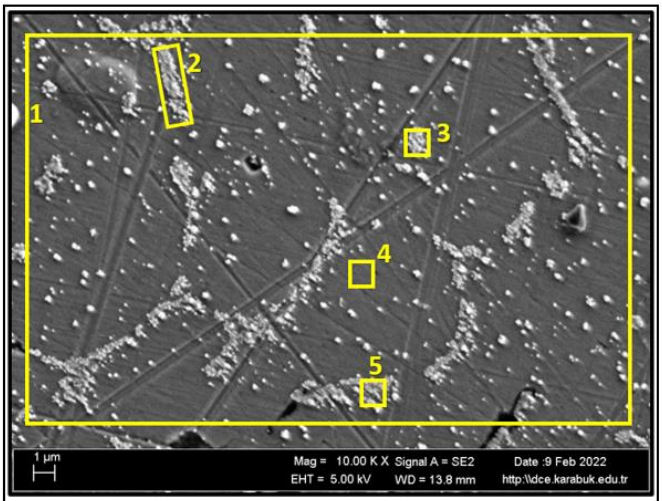

% wt	Al	Mg	Si	Bi	Mn
1	85,01	1,25	1,65	9,24	2,85
2	77,63	2,12	0,85	15,15	4,25
3	77,71	2,09	1,21	14,85	4,14
4	94,78	1,01	1,75	1,21	1,25
5	81,02	2,01	1,52	11,01	4,44

Fig. 3 SEM microstructure and EDX analyses

When the basic microstructure is examined, dispersed intermetallic structures appear in the α-Al matrix. Intermetallic structures were found at grain boundaries, revealing grain appearance. The accumulation of secondary β phases at grain boundaries is a known result in the literature [1, 3, 5, 6, 8, 9].

Elements added to the Al matrix were detected in the EDX analysis of the intermetallic formations at the grain boundaries. With the support of the literature [1, 3, 5, 6, 8-12], it can be said that these secondary phases are Al_6Mn, Mg_2Si, Mg_3Bi_2 and AlBi compounds.

As a result, the manufacturability of Al-Bi-Mn alloy in mini arc furnace is discussed in this study. The basic microstructure of the alloy was investigated. The phases that may occur in the triple equilibrium of Al-10Bi-3Mn have been examined.

IV. CONCLUSIONS

The alloy formed between Al-Bi-Mn was produced in a mini arc furnace and the following results were obtained.

1- The alloy has been successfully formed in the mini arc furnace with the required parameters.

2- In the microstructure examination, intermetallic phases dispersed in the matrix phase were observed.

3- It was observed that the intermetallic phases formed in the alloy accumulated at the grain boundaries.

4- Intermetallic phases were interpreted as Al_6Mn, Mg_2Si, Mg_3Bi_2 and AlBi with the support of the literature.

REFERENCES

[1] Somerday, M., Humphreys, F. "Recrystallisation Behaviour of Supersaturated Al–Mn Alloys Part 1–Al–1.3 Wt-% Mn," *Materials science and technology*, vol. 19, pp. 20-29, 2003.

[2] Adeosun, S., Balogun, S., Sekunowo, O., Usman, M. "Effects of Heat Treatment on Strength and Ductility of Rolled and Forged Aluminum 6063 Alloy," *Journal of Minerals & Materials Characterization & Engineering*, vol. 9, pp. 763-773, 2010.

[3] Li, H.-Y., Zeng, C.-T., Han, M.-S., Liu, J.-J., Lu, X.-C. "Time–Temperature–Property Curves for Quench Sensitivity of 6063 Aluminum Alloy," *Transactions of Nonferrous Metals Society of China*, vol. 23, pp. 38-45, 2013.

[4] Liu, Y., Zhang, J., Jia, G., Zhang, X., Ren, Z., Li, X., Jing, C., Cao, S., Deng, K. "Magnetic Anisotropy Properties and Spin Reorientation for Textured Bi− Mn Alloys Fabricated by a Field-Inducing Technique," *Physical Review B*, vol. 70, pp. 184424, 2004.

[5] Savitsky, E., Torchinova, R., Turanov, S. "Effect of Crystallization in Magnetic Field on the Structure and Magnetic Properties of Bi-Mn Alloys," *Journal of Crystal Growth*, vol. 52, pp. 519-523, 1981.

[6] Cao, C., Liu, W., Liu, Z., Xu, J., Hwang, I., De Rosa, I., Li, X. "Scalable Manufacturing of Immiscible Albi Alloy by Self-Assembled Nanoparticles," *Materials & Design*, vol. 146, pp. 163-171, 2018.

[7] Fan, M.-Q., Xu, F., Sun, L.-X., Zhao, J.-N., Jiang, T., Li, W.-X. "Hydrolysis of Ball Milling Al–Bi–Hydride and Al–Bi–Salt Mixture for Hydrogen Generation," *Journal of Alloys and Compounds*, vol. 460, pp. 125-129, 2008.

[8] Zamin, M. "The Role of Mn in the Corrosion Behavior of Al-Mn Alloys," *Corrosion*, vol. 37, pp. 627-632, 1981.

[9] Li, W., Jiang, H., Zhang, L., Li, S., He, J., Zhao, J., Ai, F. "Solidification of Al-Bi-Sn Immiscible Alloy under Microgravity Conditions of Space," *Scripta Materialia*, vol. 162, pp. 426-431, 2019.

[10] Zajac, S., Hutchinson, B., Johansson, A., Gullman, L.-O. "Microstructure Control and Extrudability of Al–Mg–Si Alloys Microalloyed with Manganese," *Materials science and technology*, vol. 10, pp. 323-333, 1994.

[11] Silva, A. P., Spinelli, J. E., Garcia, A. "Thermal Parameters and Microstructure During Transient Directional Solidification of a Monotectic Al–Bi Alloy," *Journal of alloys and compounds*, vol. 475, pp. 347-351, 2009.

[12] Chen, Z., Hou, Y., Xie, B., Zhang, Q. "Dendrite Morphology Evolution of Al6mn Phase in Suction Casting Al–Mn Alloys," *Materials*, vol. 13, pp. 2388, 2020.

Atomistic insight into the Density Effect on Dynamic Properties in 45S5 Melts

Youssef Ouldhnini[1], Achraf Atila[2], Said Ouaskit[3] and Abdellatif Hasnaoui[1].

1. LS3M, Faculté Polydisciplinaire Khouribga, Sultan Moulay Slimane University, B.P 145, 25000 Khouribga, Morocco, ouldhniniyoussef@gmail.com

2. Materials Science and Engineering, Institute I, Friedrich-Alexander-Universität Erlangen-Nürnberg (FAU), Martensstr5, Erlangen 91058, Germany,

3. Laboratoire de Physique de la Matière Condensée, Faculté des Sciences Ben M'sik, Université Hassan II de Casablanca, B.P 7955, Av Driss El Harti, Sidi Othmane, Casablanca, Maroc

Bioactive glasses liberate ions when they are inserted into the human body. Regardless, a surplus of the released ions can produce anomalies related to cytotoxicity. Controlling ion release is considered one of the main challenges in developing new bioactive glasses. In this work, we use molecular dynamics (MD) simulations to investigate the effect of density on the dynamics of soda-lime phosphosilicate (45S5) systems. The diffusion coefficient illustrates three regimes as the density increases. The modifiers' mobility is significantly correlated with the increase of the density, especially Na atoms, in comparison to other elements. We use a modified Arrhenian equation to evaluate the complex dynamic behaviour of 45S5 melts and correlate it to the changes in the structural features by evaluating the network connectivity and pair-excess entropy.

Investigation of wear behavior of SiC reinforced waste aluminum matrix composites

Özgür YILMAZ[1*], Mevlüt GÜRBÜZ[2]

*[*1]Buharkent Vocational School, Aydın Adnan Menderes University, Aydın, Turkey*
ozgur.yilmaz@adu.edu.tr

[2]Mechanical Engineering, Ondokuz Mayıs University, Samsun, Turkey
mgurbuz@omu.edu.tr

***Abstract*— In the study; SiC reinforced (1-9 wt. %) aluminum matrix composites from waste beverage cans were fabricated by stir casting method. The effect of reinforcement ratio on the experimental density, hardness, the compressive and tensile strength of the composites was investigated. The crystal structures and microstructure of the composite materials were analyzed by X-ray diffraction (XRD) method and scanning electron microscopy (SEM). From the results, the hardness of composites increased from 70,81 HV (pure Al alloy) to 89,80 HV (for 9 wt. % SiC). When the wear test results of SiC reinforced composites under different loads are evaluated, the least mass loss ($\Delta m=11$ mg) and the lowest wear rate ($W= 4.22\times10^{-5}$ mm^3/Nm) were obtained for AlSiC9 composite under the same load (20 N).**

***Keywords*— SiC; waste aluminum; stir casting; composite; wear**

I. INTRODUCTION

Depending on today's technological developments, composite materials have been started to be produced in order to meet the desired material properties. Composite materials have been developed from their superior properties such as low density, high mechanical properties, high wear and corrosion resistance [1-3]. Composite materials are divided into three main classes depending on the matrix type: polymer matrix composite (PMC), ceramic matrix composite (CMC) and metal matrix composite (MMC)[4]. MMCs are composites that use metal as matrix material and ceramic or organic material as reinforcing element. Metals and alloys such as Al, Ti, Mg, Ni, Cu, Co and Zn are generally used as matrix materials in MMC [5].

Aluminum and its alloys, which are widely used in the aerospace industry, automotive industry, construction industry, and transportation, are important matrix materials in MMC. These alloys are preferred because of their low densities, low melting temperatures, easy forming and wetting of many ceramic reinforcement elements. [6]. Aluminum and its alloys are close to 100% and one of the most preferred metals because they can be recycled more easily than other metals. Beverage cans are one of the most widely used areas of aluminum and a cornerstone of the aluminum recycling market. Aluminum beverage cans are widely used around the world and can be recycled. While the collection rate of aluminum beverage cans is 69.1% in the world, it is 70% in Europe. This rate is 54.7% in America, 52% in England, 91% in Germany, 99.5% in China, 75% in Japan and 92.7% in Turkey[7],[8] .

The reinforcement element is one of the most important elements that make up the composite material. In a composite material, the reinforcing element carries the load, increasing the stiffness and strength of the matrix. Particulate reinforcement elements such as SiC, B4C, TiC, Si3N4 and carbon-based (graphene, carbon nanotube) are generally used to improve the mechanical properties of the matrix material [9],[10]. SiC provides composites with higher hardness, pressure behavior and tribology properties due to its high wear resistance, low coefficient of friction, high thermal shock resistance, adequate thermal expansion and thermal conductivity coefficient [11]-[13]. Although MMC is usually produced by solid or liquid phase methods, particle reinforced aluminum matrix composites (AMC) are more easily produced with the liquid phase. Mixed casting, which is one of the most used methods in liquid phase production techniques, is preferred because of its low cost and simple method[6].

Manufacturing and characterization of SiC reinforced (1-9% by weight) aluminum matrix composites from waste beverage cans were carried out. The effect of the reinforcement ratio on the experimental density, hardness and wear of the composites was evaluated in detail.

II. EXPERIMENTAL

In this study, instead of primary aluminum materials or aluminum powders, waste beverage cans and SiC (44 µm in average size from particle size analyzer with laser diffraction) have been used as Al matrix and reinforcement element. SiC reinforced aluminum composites with 1%, 3%, 5%, 7% and 9% ratios by weight have been produced by stir casting method. The schematic representation of the method is given in Fig. 1. The codes of casted composites are given in Table 1.

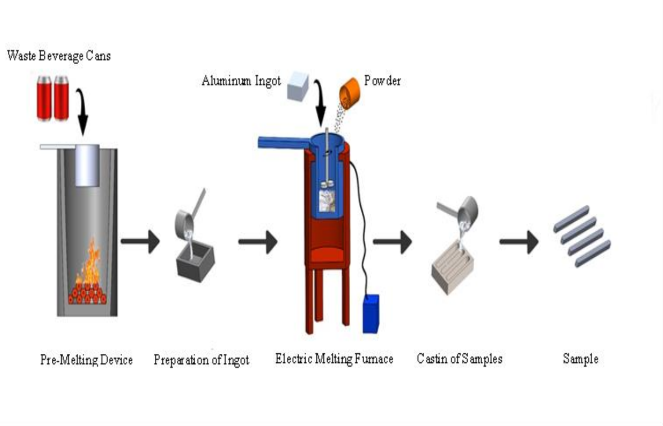

Figure 1. The schematic illustration of composite fabrication

Table 1. Sample code of the materials

Material	**Code**
Pure Al	Al-0SiC
Al- 1% SiC	Al-1SiC
Al- 3% SiC	Al-3SiC
Al- 5% SiC	Al-5SiC
Al- 7% SiC	Al-7SiC
Al- 9% SiC	Al-9SiC

The manufactured composites and SiC microstructures have been analyzed by scanning electron microscope (SEM, Leol JSM-6610LV) and X-Ray diffraction (XRD, Rikagu Rint 2200) device. Densities of the specimens have been measured by using Archimedes' principle. Harnesses of the unreinforced matrix material and aluminum composites with SiC reinforced specimens determined by using TMTECK-HV-1000B device with principles Vickers hardness test. For doing that, 1.96N (200g) load has been applied for 20 seconds for every one of each specimen for five times and for every specimen, average hardness value has been calculated. In addition, wear test was applied to determine the wear resistance of matrix material and SiC reinforced composites under dry conditions.

III. RESULTS AND DISCUSSION

A. Density

In Fig. 2, the highest experimental density (2.66 g/cm^3) among Al-SiC composites were measured for 5 wt. % SiC content. The improvement of experimental density with SiC addition can be explained that homogeneous dispersion of the powder, higher experimental density of SiC particles than aluminum alloy. Increasing experimental density can be explained with homogeny distributed SiC for low content, the higher experimental density of SiC particles.

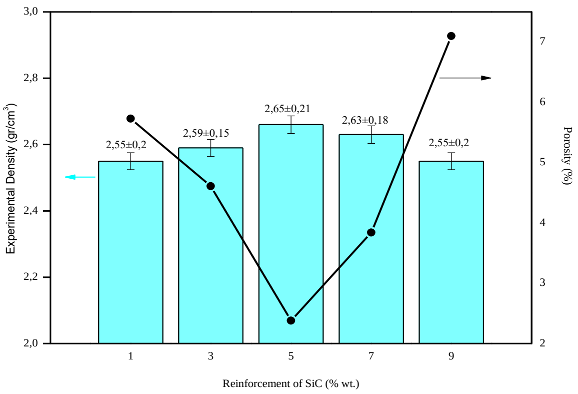

Figure 2. Experimental density and open porosity results of SiC reinforced composites

B. Hardness

Fig. 3 gives the micro Vickers hardness of Al-SiC composites. The highest hardness (89.8 HV) is observed for Al-9SiC composites. Increasing SiC content has a positive effect on hardness due to its homogeny particle dispersion in a matrix and its outstanding hardness compared al alloy. Theoretically, the hardness increase can be explained with the rule of mixtures by Eq.(1) [14].

$$H_c = H_m f_m + H_r f_r \qquad (1)$$

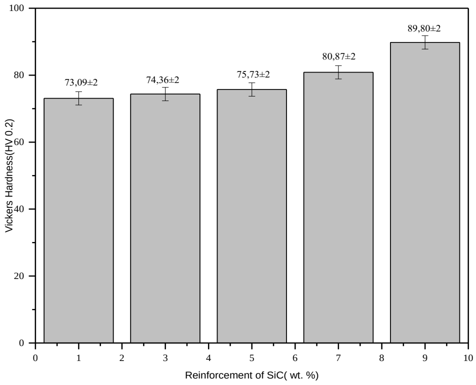

Figure 3. The Vickers hardness of SiC reinforced composites

C. Wear Behavior

In this study, a 20 mm radius disc made of 2379 cold tool steel was used as abrasive disc. The hardness of the abrasive disc is 60-65 HRC. The rotational speed (n) of the disc is 200 rpm. The abrasion test time (t) applied to the samples is 20 minutes. Accordingly, the shear distance (L) is calculated as 500 m using equation 2.

$$L = 2 * \pi * R * n * t \text{ (m)} \qquad (2)$$

The volume of eroded material (ΔV) is given in 3 as the ratio of the mass loss (Δm) of the sample to the composite density (ρ).

$$\Delta V = \Delta m / \rho \ (\text{mm}^3) \qquad (3)$$

Wear rate (W), including the load P (N) applied to the materials, is calculated with equality 4 [14].

$$W = \Delta V \ (P * L) / (\text{mm}^3 / \text{N.m}) \qquad (4)$$

As a result of the wear test performed on SiC reinforced aluminum composite materials, the mass change depending on the load is given in Figure 4. In the wear tests, it was determined that the mass loss (Δm) increased depending on the applied load. The highest mass loss occurred in the 5% SiC reinforced composite material under 20 N load. It has been observed that the least mass loss under the same load is 9% SiC reinforced composite.

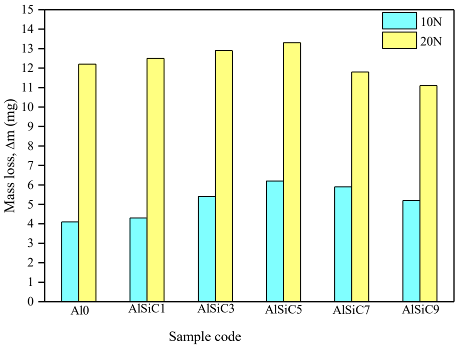

Figure 4. Mass loss variation in Al/SiC composite structures

As a result of the wear test, the wear rates (W) under load (P) for non-reinforced and SiC reinforced composite structures are given in Figure 5. The lowest wear rate under both loads was observed in the 9% SiC reinforced composite. However, the wear rate increased with the increasing reinforcement rate. The reason for this is that the reinforcement element tends to agglomerate and SiC clusters begin to form in the matrix.

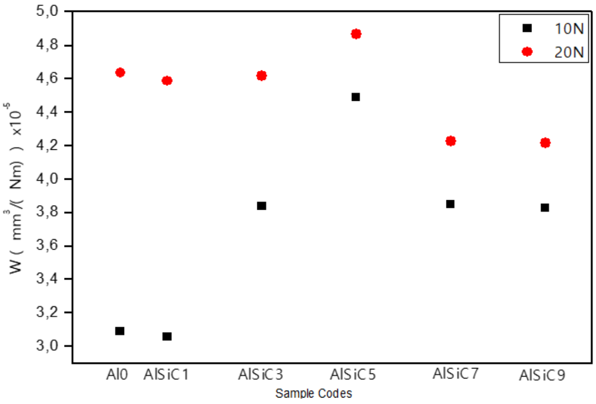

Figure 5. Wear rate change in Al/SiC composite structures

The wear traces of pure Al, Al-Grf composite structures under P=20 N load in dry conditions are given in Figure 6. When the abrasive wear marks were examined, it was observed that the minimum deformation occurred in the AlSiC9 composite structure. Due to the hard structure and abrasive nature of SiC, it has been determined that the wear is reduced with SiC additive, and scanning electron microscopy wear marks confirm the wear tests. When the load is increased based on the same materials, it has been determined that the traces become deeper, in other words, the deformation and wear increase (Figure 5.16).

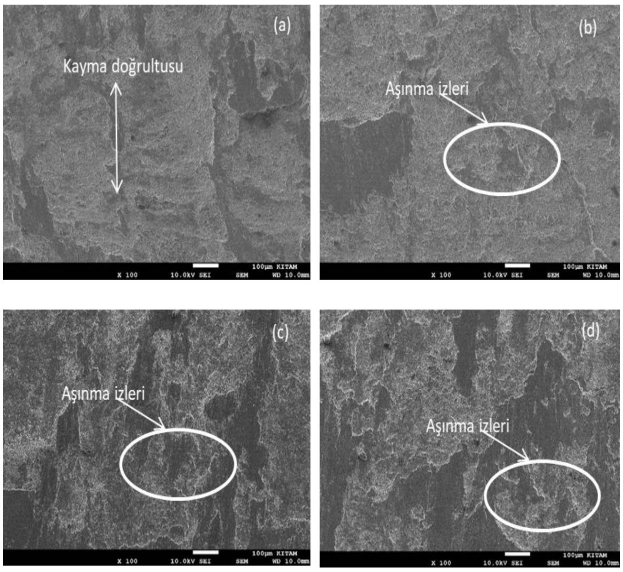

Figure 6. Wear marks of (a) Al0, (b) AlSiC, (c) AlSiC5, (d) AlSiC9 composites (100 X magnification, under P=20N load)

D. Characterization of the composites

Table 2 gives the EDX analyses of the fabricated aluminum alloy ingot from waste aluminum which includes the Si, Mg, Mn instead of Al. These alloying elements positively affect the mechanical properties of the composites.

Table 2. EDX analyses of pure beverage cans and casted aluminum alloy

	Al	Si	Mg	Mn
Pure Beverage Cans (wt.%)	94.72	3.62	0.78	0.88
Casted Samples (wt.%)	93.85	4.18	0.76	1.21

SEM-EDS elemental mapping images of the produced Al-SiC composite structures are given in Figure 7. In these analyzes, each element is shown with a different color, and it can be determined which elements are present in the internal structure and how these elements are distributed. Since Al alloy was used as the matrix material, the presence of Mg and Mn was also seen in the structure in addition to aluminum in the elemental memory images.

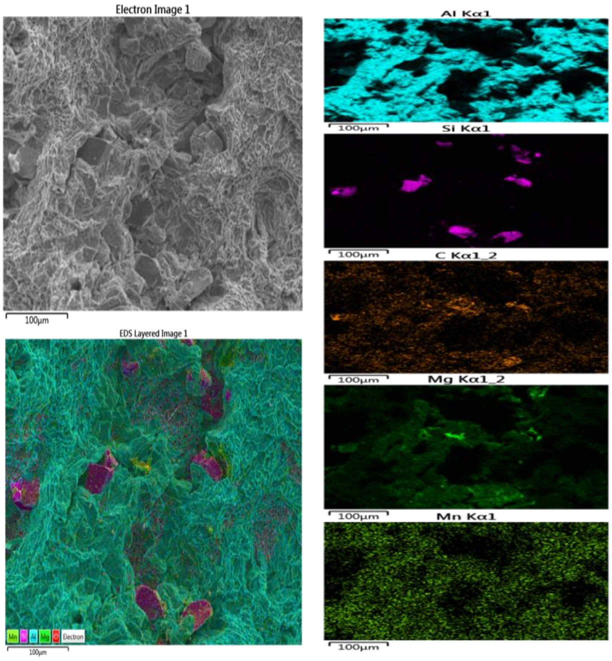

Figure 7. Elemental distribution analysis of Al-SiC composites by SEM-EDS mapping

Also, the XRD patterns of SiC reinforced aluminum composites are given in Fig. 8. As clearly seen, all diffractions possess pure Al and SiC. In addition, second phases such as aluminum carbide (Al_4C_3) peak is not detected for all Al-SiC samples due to the low-temperature casting which is not activated to react Al with Si-C.

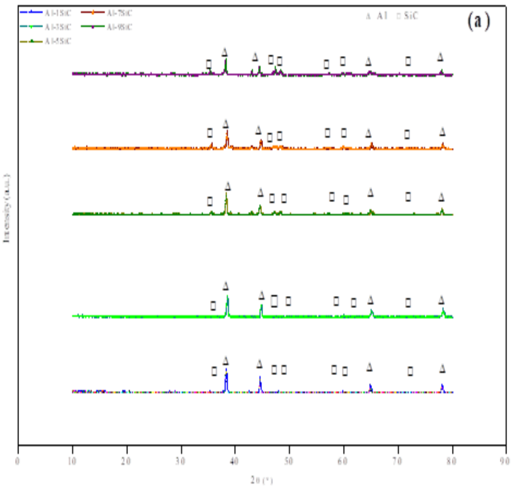

Figure 8. XRD analysis of the SiC reinforced Al composites

IV. CONCLUSIONS

In this study, SiC reinforced aluminum composites were prepared by stir casting method. Experimental density, hardness, tensile/compressive strength and microstructure of the composites were evaluated. According to the results, the highest experimental density (2.66 g/cm3) among Al-SiC composites were measured for 5 wt. % SiC content. The highest hardness (89.8 HV) is found for Al-9SiC composites. The best wear rate (W= $4.22x10^{-5}$ mm^3/Nm for 20N) was measured at 9 wt. % SiC reinforced composites. In SEM and XRD analysis, homogeneously distributed SiC and secondary phases were not formed.

V. ACKNOWLEDGMENTS

The authors are thank to financially support the TÜBİTAK, under the grants (TÜBİTAK 2180677). The authors of this study thank the Black Sea Advanced Technology Research and Application Center (KITAM) in Ondokuz Mayıs University (OMU) for SEM and XRD analysis.

VI. REFERENCE

[1] B. Öztop. and M. Gürbüz, Investigation of Properties of Composites Produced by Reinforcement Graphene Matrix Obtained from Waste Aluminium. International Journal of Multidisciplinary Studies and Innovative Technologies, 2017. 1(1): p. 4-8.

[2] M. Erdoğan., The Production of steel fibre reinforced aluminium composite material and investigation of its mechanical properties experimentally, in Department of Mechanical Engineering. 2005, Dumlupınar University: Kütahya.

[3] E., Işık., The production of Al-12Si matrix composite reinforced with SiC particles by powder metallurgy and analysis of the wear behaviour, in Department of Mechanical Engineering. 2014, Gazi University: Ankara.

[4] M.K. Surappa, Aluminum matrix composites: Challenges and opportunities. Sadhana, 2003. 28(1-2): p. 319-334.

[5] Y. Şahin, Kompozit Malzemelere Giriş. 2006, Ankara: Seçkin Yayınevi.

[6] J. Hashim, L. Looney, M.S.J. Hashmi, Metal matrix composites: production by the stir casting method. Journal of Materials Processing Technology, 1999. 92-93: p. 1-7.

[7] Aluminium Recycling in Europe. [cited 20.12.2021.

[8] Global Aluminium Recycling:A Cornerstone of Sustainable Development. [cited 20.12.2021.

[9] C. Soldano, A. Mahmood.and E. Dujardin., Production, properties and potential of graphene. Carbon, 2010. 48(8): p. 2127-2150.

[10] M. Pul, Al matrisli MgO takviyeli kompozitlerin infiltrasyon yöntemi ile üretilmesi ve işlenebilirliğinin değerlendirilmesi, in Fen Bilimleri Enstitüsü. 2010, Gazi Üniversitesi Ankara.

[11] P. Bajaj, "Mechanical Behaviour of Aluminium Based Metal Matrix Composites Reinforced With SiC And Alumina," Master, Mechanical Engineering, Thapar University, 2007, India.

[12] M.T. Sijo and K.R. Jayadevan, "Analysis of stir cast aluminum silicon carbide metal matrix composite: A comprehensive review," Procedia Technology, vol. 24, pp. 379-385, 2016.

[13] C. M. Şenel, M. Gürbüz, and E. Koç, " New generatıon composıtes wıth graphene reınforced alumınum matrıx," Engineer and Machine, vol. 56, p. 669, 2015.

[14] C. M. Şenel, M. Gürbüz, and E. Koç, Mechanical and tribological behaviours of aluminium matrix composites reinforced by graphene nanoplatelets. Materials Science and Technology, 2018.

Fabrication of Ti6Al4V composite foams and their characterization

Ömür Ekrem GÜNTÜRK[1*], Mevlüt GÜRBÜZ[1]

[1]*Mechanical Engineering, Ondokuz Mayıs University, Samsun, Turkey
ekrem055@hotmail.com

[1]Mechanical Engineering, Ondokuz Mayıs University, Samsun, Turkey
mgurbuz@omu.edu.tr

***Abstract*—In this study; graphene reinforced Ti6Al4V foam matrix composites were produced by powder metallurgy method. Shaping work was carried out using Ti6Al4V foam. Studies were carried out between 50-100 bar as forming pressure. The best forming pressure was determined as 80 bar. Studies were carried out at different sintering temperatures and times using Ti6Al4V powder. According to the obtained results, the best sintering time was determined as 120 minutes and the sintering temperature was 1250°C. According to the results, over 91% and 30% density was obtained for dense and foam materials. The foam wall hardness value increased up to about 405 HV with increasing temperature. Density values over 93% and 30% for dense and foamed sample. The foam wall hardness increased up to 438 HV for graphene reinforced Ti6Al4V foam.**

***Keywords*— Ti6Al4V; graphene; powder metallurgy; composite; foam**

I. INTRODUCTION

Composites consist of a combination of two or more materials, the main phase to which the reinforcement is added and the reinforcement phase. High hardness and strength advantages make composite materials frequently preferred. Composite materials have emerged as a result of our need for materials that are low in cost, light and with better mechanical properties [1-3]. Metal matrix composite materials, which are a kind of composite materials; It is used in many industries such as aviation, health and automotive because it has features such as high strength, good fatigue and wear resistance, high hardness [1]-[4]. Titanium and its alloys are one of the most preferred metal matrix composites. Metals are hard and strong, whereas foam materials are light, inexpensive and have adjustable density [5-7]. The most common technique for preparing metallic foam is to sinter with the spacer method. First, the space-holding material is mixed with the metallic powder to be used, the second operation is compression and finally, it is removed from the structure before or during the sintering process [8]-[9].

Powder metallurgy is the best method for processing titanium foams [10]. Powder metallurgy generally consists of powder preparation, mixing, compression, sintering and final processing steps [11]. When we examine the studies in the literature, we encounter that graphene is used as a reinforcement element to develop titanium and its alloys. Mutuk T. and Gürbüz M. investigated the hardness and compressive strength of hybrid titanium composites reinforced with S3N4 and graphene binary powder in their study. They added 3% by weight silicon nitride (Si_3N_4) powder and varying amounts of graphene to the titanium matrix. At the end of the study, they found improvement in mechanical properties. The highest hardness value (634 HV) and compressive strength (1458 MPa) values were measured in hybrid composites with 0.15 wt% graphene and 3 wt% silicon nitride (Si_3N_4) added [12]. Due to its mechanical, electrical and thermal properties, the demand for graphene has tended to increase in recent years [13]. Graphene, which is very effective in improving the mechanical properties of metals, has a honeycomb-like microstructure [14].

In this study, Ti6Al4V foam samples and Ti6Al4V foam composite samples with graphene at different rates were prepared using the powder metallurgy method. Mechanical tests of the produced samples were carried out. In the study, shaping optimization was performed. Mechanical properties of Ti6Al4V foam composites, both pure and graphene at different rates, were investigated depending on different temperatures and times. In the study, urea was used as spacer to obtain the foam structure. Thanks to the high mechanical properties of graphene, it is aimed to improve the mechanical properties of the composite structure.

II. EXPERIMENTAL

In this study, Ti6Al4V and graphene powders were first mixed in an ultrasonic bath at 25°C for 30 minutes in order to prevent agglomeration. In the next step, it was mixed in a ball mill at 800 rpm for a total of 30 minutes in order to ensure that the powders mix better and become homogeneous. The powders homogenized in the ball mill were filtered and dried. In order to get the final form of the powders, they were sieving and mixed with urea. The powders mixed with urea were shaped and the sintering process was carried out by purifying the urea. The shaping process was done at 80 bar. The sintering process was carried out at 1250°C and 120 minutes under an argon gas atmosphere. The schematic representation of the method is given in Fig. 1. The codes of composites are given in Table 1.

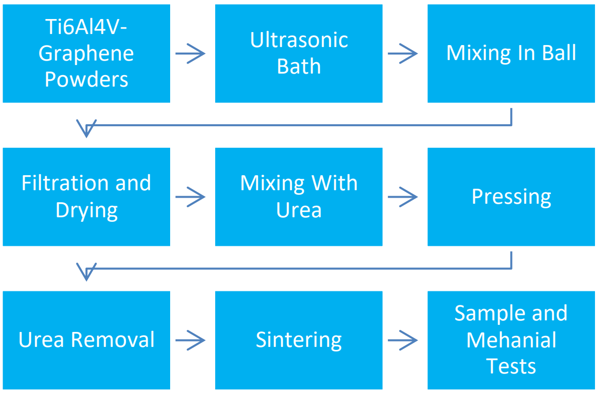

Figure 1. The schematic illustration of composite fabrication

Table 1. Sample Code of The Materials

Material	Code
Pure Ti6Al4V Foam	Ti64-0Gr-F
Ti6Al4V- 0,15% Gr Foam	Ti64-0,15Gr-F
Ti6Al4V- 0,30% Gr Foam	Ti64-0,30Gr-F
Ti6Al4V- 0,45% Gr Foam	Ti64-0,45Gr-F
Ti6Al4V- 0,60% Gr Foam	Ti64-0,60Gr-F

Ti6Al4V properties are given in Table 2.

Table 2. Ti6Al4V Properties

Ti6Al4V Properties	**Value**
Density (g/cm^3)	4,43
Melting Temperature (°C)	1650
Yield Strength (MPa)	820
Hardness (HV)	330-370
Thermal Condutivity (W/mK)	7
Modulus of Elasticity (GPa)	100-130
Tensile Strength (MPa)	960-1270

In the study, forming optimization studies were carried out under 50-60-70-80-100 bar. Shaping work is given in figure 2.

As a result of the studies, it was observed that the urea powder mixture did not form at 60 bar and below. In the experiments carried out between 60-80 bar, it was determined that the desired density could not be reached and at the same time, it was determined that the raw samples obtained were not fully formed. In studies carried out above 80 bar, laminar crack lines were detected in the raw samples. As a result of shaping optimization, it was determined that the most suitable shaping value was 80 bar.

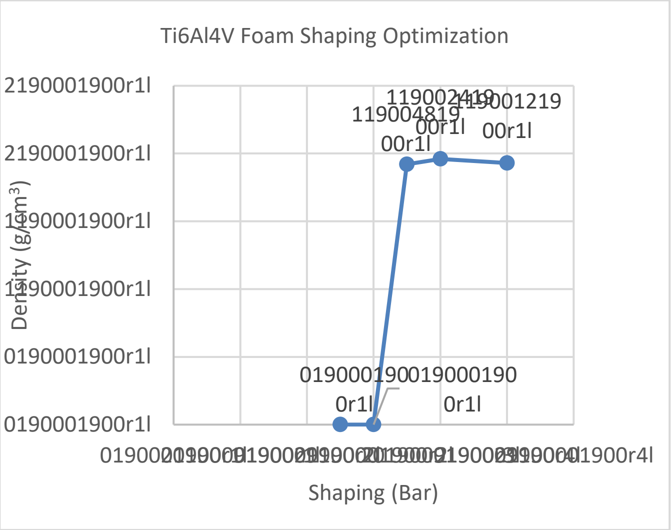

Figure 2. Ti6Al4V shaping work

Sintering process was applied to the shaped samples in an argon gas atmosphere at 1000, 1100, 1200, 1250°C and 60, 120, 180 minutes.

The properties of graphene are given in Table 3.

Table 3. Graphene Properties

Graphene Properties	**Value**
Hybrid shape	sp^2
Number of layers	Single layer
crystal structure	Hexagonal
Actual density (g/cm^3)	2,25
Thickness (nm)	5-8
Surface area (m^2/g)	2600
Thermal conductivity (WK^{-1}/m)	4840-5300
Modulus of elasticity (TPa)	1

III. RESULTS AND DISCUSSION

A. Density

The variation of the density values of the pure and dense samples produced by powder metallurgy method depending on the sinter time (60, 120, 180 minutes) was investigated. The variation of the density for dense samples depending on the sintering time is given in figure 3. The best sintering time was determined as 120 minutes. As a result of the sintering process performed on Ti6Al4V samples in 120 minutes, the best density value was found to be 4.01 g/cm^3.

The results of the study, in which the variation of the density depending on the sinter temperature (1000, 1100, 1200, 1250°C) was examined, is given in figure 4. It was observed that the best sintering temperature was 1250°C and the best density value obtained as a result of the sintering process performed at this temperature was 4.06 g/cm^3.

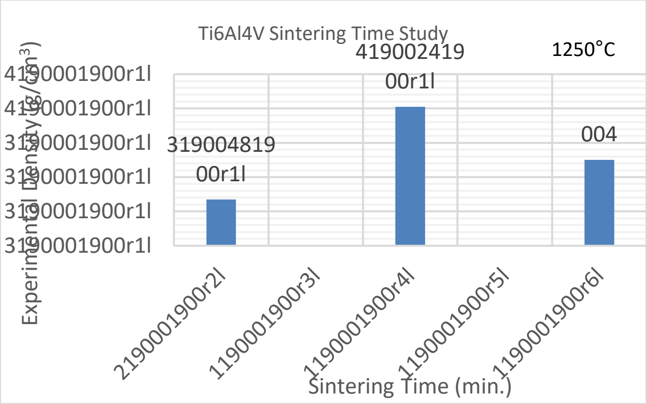

Figure 3. Sintering time study for dense samples

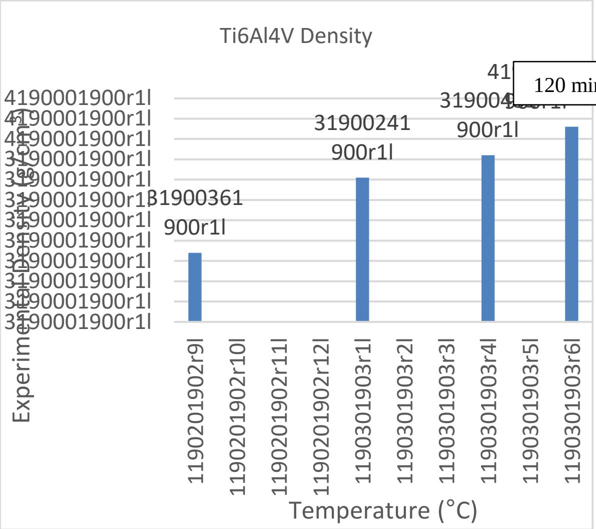

Figure 4. Density variation of Ti6Al4V samples with temperature for dense samples

Density values of Ti6Al4V dense composites without additives and graphene at different rates are given in Figure 5. When the results were examined, it was seen that the best density value (4.14 g/cm^3) was obtained in 0.15% graphene added Ti6Al4V composite composition.

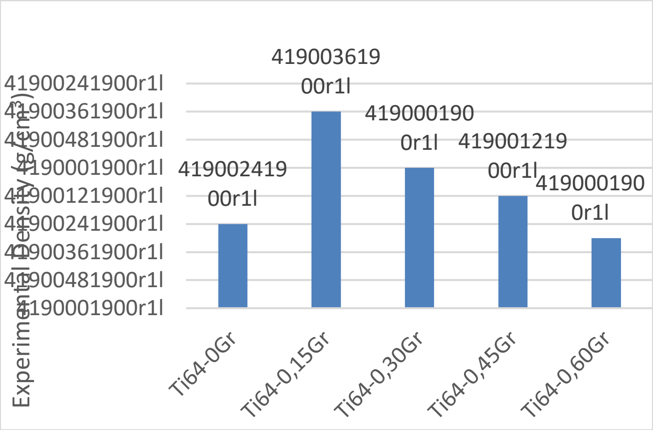

Figure 5. Ti6Al4V density variation without reinforcement and at different graphene ratios

B. Hardness of foam wall

The foam samples is given on the hardness chart. The hardness values of Ti6Al4V foam wall samples, depending on the temperature change (1000, 1100, 1200, 125°C) in a constant time, were investigated. The best hardness value was obtained from the samples sintered at 1250°C (405 HV). The obtained vickers hardness values are given in figure 6. Hardness values are taken from the walls between the gaps.

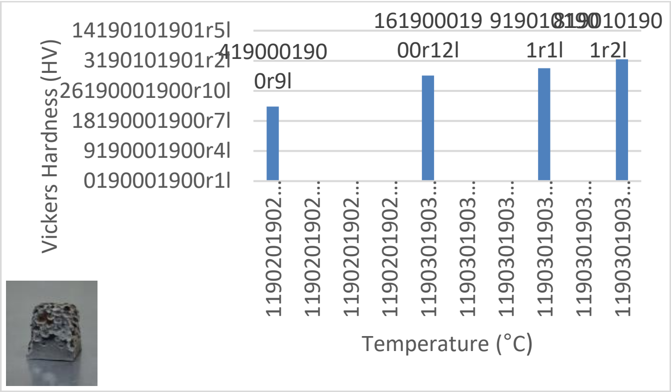

Figure 6. Ti6Al4V foam-wall hardness results

Hardness values of pure Ti6Al4V foam and graphene added Ti6Al4V foam composites at different rates were examined. The best foam wall hardness values (438 HV) were achieved in the composite composition with 0.15% graphene. The obtained values are given in figure 7. The reduction of the properties can be explained with the agglomeration tendency of the graphene. It does not act as reinforcement element for high content graphene. It shifts to solid lubricant materials due to agglomeration which causes the easy sliding during plastic deformation. It led to deterioration of properties of the composites [12,14].

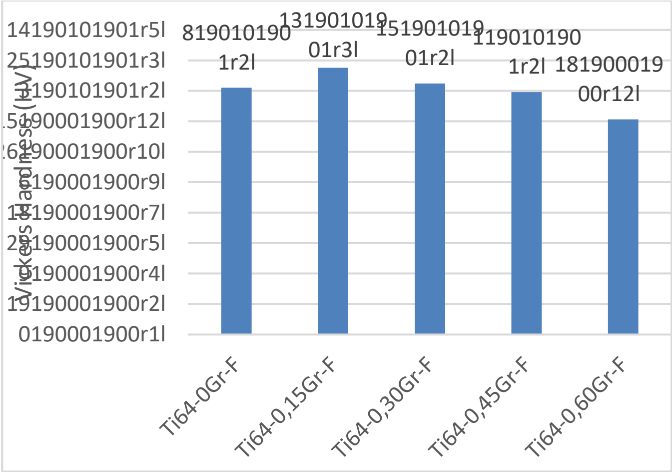

Figure 7. Hardness values of unreinforced Ti6Al4V foam and graphene reinforced Ti6Al4V foam composites at different rates

IV. CONCLUSIONS

In this study, the best forming pressure was determined as 80 bar. For the sintering time, 120 minutes was determined as the best sintering process time. In the sintering processes performed at different temperatures, the best density (4.06 g/cm^3) and the best Vickers hardness value (405 HV) were obtained in the sintering processes at 1250°C.

It has been observed that the composition, in which the best density and hardness value of graphene, which is the reinforcement element, is obtained, is Ti6Al4V foam composite with 0.15% graphene doped. At this additive ratio, the best density dense value of 4.14g/cm3 and the best vickers hardness value of 438 HV were obtained.

V. ACKNOWLEDGMENTS

The authors of this study thank the Ondokuz Mayıs University Faculty of Engineering, Department of Mechanical Engineering and Metallurgy and Materials Sciences for providing the opportunity to use their laboratories.

VI. REFERENCE

[1] A. Kumar, S. Lal, and S. Kumar, "Fabrication and characterization of A359/Al2O3 metal matrix composite using electromagnetic stir casting method," *Journal of Materials Research and Technology*, vol. 2, pp. 250-254, July-Sept., 2013

[2] M. Kumar, R. K. Gupta, and A. Pandey, "A review on fabrication and characteristics of metal matrix composites fabricated by stir casting," IOP Conference Series: Materials Science and Engineering, 2018, paper 377.1, p. 012125.

[3] W. Zhou and Z. Xu, "Casting of SiC reinforced metal matrix composites," *Journal of Materials Processing Technology vol. 63(1-3), pp. 358-363, Jan., 1997*

[4] B. Harris, Engineering composite materials, London, England, 1999

[5] M. F. Ashby, T. Evans, N. A. Fleck, J. Hutchinson, H. Wadley, and L. Ginson, *Metal foams: a design guide, United States of America, 2000*

[6] A. Mansourighasri, N. Muhamad, and A. Sulong, "Processing titanium foams using tapioca starch as a space holder," *Journal of Materials Processing Technology, vol. 212, pp.. 83-89, Jan., 2012*

[7] N. B. Üllen and G. Karabulut, ''Gözenekli metalik malzeme üretiminde gözenek oranı ve küresellik arası ilişkinin incelenmesi,'' *2nd International Eurasian Conference on Science, Engineering and Technology*, EurasianSciEnTech, paper 467-472, October 2020.

[8] T. Imwinkelried, ''Mechanical properties of open-pore titanium foam,'' *Journal of biomedical materials research Part A*, vol. 81.4, pp, 964-970, 2007.

[9] J. Jakubowicz, G. Adamek, and M. Dewidar. ''Titanium foam made with saccharose as a space holder,'' *Journal of Porous Materials,* vol. 20.5, pp. 1137-1141.

[10] M. Sharma, G. Gupta, O. Modi, B. Prasad, and A.K. Gupta. ''Titanium foam through powder metallurgy route using acicular urea particles as space holder,'' *Materials letters*, vol. 65.21-22, pp. 3199-3201.

[11] G. Sudha, B. Stalin, M. Ravichandran, and M. Balasubramanian, Mechanical properties, characterization and wear behavior of powder metallurgy composites-a review, *Materials Today: Proceedings*, vol. 22 pp. 2582-2596, 2020

[12] T. Mutuk, and M.Gürbüz, Si_3N_4/Graphene binary partiles reinforced hybrid titanium composites and their characterization, International Journal of Materials Research, vol. 112 pp. 717-725, 2021

[13] W. Yao, L. Tang, J. Wang, J. Yang, Y. Jiang, H. Shi, and X Wei, Electrically tunable graphene metamaterial with strong broadband absorption, *Nanotechnology, vol. 32, Nov. 2020*

[14] M. C. Şenel, and Ü. Mahmutoğlu, Effect of induction heat treatment on the mechanical properties of Si3N4–graphene-reinforced Al2024 hybrid composites, *Bulletin of Materials Science, vol. 45 pp1-17 March 2022*

Particle-reinforced multi-hybrid aluminium composite production and morphological analysis

Tuna AYDOGMUS*

*Hitit University
Technical Sciences School, Corum. Turkey
tunaaydogmus@hitit.edu.tr

***Abstract* — In this study, a multi-hybrid composite material was produced with 10% SiC and 10% B_4C particles added to the matrix aluminium structure. An Al7075 series alloy was formed by adding Cu, Fe, Mg, Zn and Si to the structure together with pure aluminium. Both Al7075 alloy and multi-hybrid composite were investigated separately in this study. First, the mixing and pressing process of high-purity powder materials has been completed. Then, the tablet powder mixture was melted in a mini arc furnace and a metal matrix composite material was produced. After solidification, the sample was subjected to homogenization heat treatment at 400C/12h conditions. After sample preparation, images were taken in scanning electron microscopy (SEM) and its morphological structure was examined. Finally, Vickers hardness values were taken from the samples and analysed. As a result, it was observed that the hardness value increased by 93% with the production of a multi-hybrid composite material.**

***Keywords*— Aluminium, SiC, B_4C alloy, arc melting.**

I. INTRODUCTION

Al alloys are a material that is frequently used in the industry due to the density difference. However, these alloys have negative aspects against tribological, corrosive and mechanical effects. Therefore, materials using composite structures, in which aluminium alloys are used as matrix, have taken their place in the industry [1-3].

Composites are structures reinforced with particles, fibres, whiskers, etc. within the framework of a metal matrix. In this framework, composite materials are produced with single and/or multiple reinforcement elements added to the matrix Al alloy. Thus, the structure can become more resistant to service conditions without increasing the density [2, 4, 5].

The reinforcement products used in composite materials are selected from materials that give more successful results than the matrix phase. At the beginning of these structures, carbide structures, hard fibres and glassy particles are frequently used. As a result, matrix structure with the support of rigid reinforcement elements gives more successful results in many experiments [6, 7].

In this study, a composite material was produced by adding 10%SiC and 10%B_4C particles to a matrix structure in the Al7075 series. Metal matrix composite material production was completed by melting the compressed powders in a mini arc furnace. Afterwards, the obtained sample was examined in SEM environment and micro hardness tests were carried out.

II. MATERIALS AND METHODS

This study started with the compression of powder raw materials under a simple press and mould. Afterwards, the moulded powders were melted in the form of a mini tablet in a Buhler Arc Melter MAM-1 brand arc furnace for 5 repetitions. Samples were expected to solidify at each melting repetition. The melting processes were completed in a lantern filled with Argon gas by vacuuming. Afterwards, the obtained samples were subjected to homogenization heat treatment at 400C/12h conditions. Thus, the homogeneous distribution of the particles and the processes of possible phases are completed.

Al7075 alloy used during alloy preparation was formed with Al, Cu, Fe, Mg, Zn, and Si elements (Table 1). Powders are carbide materials with a purity of at least 99.5% at the micron level. 10%SiC and 10%B_4C particles were added to Al7075 alloy to form composite. Thus, Al7075 alloy and Al7075 multi-hybrid composite (Al7075MHC) structure were compared. SEM images of all powders and carbides used are given in Figure 1.

Table 1. Al7075 composition

Al7075	Cu	Fe	Mg	Zn	Si	Al
% wt	1,35	0,30	2,3	5,5	0,3	balance

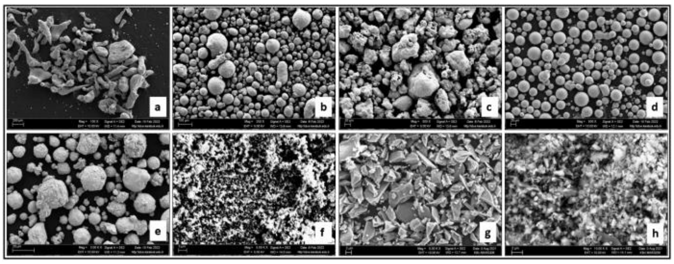

Fig. 1. Powder materials;
(a) Al, (b) Cu, (c) Fe, (d) Mg, (e) Zn, (f) Si, (g) SiC, and (h) B_4C

The prepared samples were taken into SEM analysis after the classical metallographic steps. Afterwards, Vickers micro hardness test was applied under 1000 g load. The average value was used by taking 10 measurement values from the far points of the hardness.

III. RESULTS AND DISCUSSIONS

The basic SEM microstructure obtained from the Al7075 and Al7075MHC is given in Figure 2.

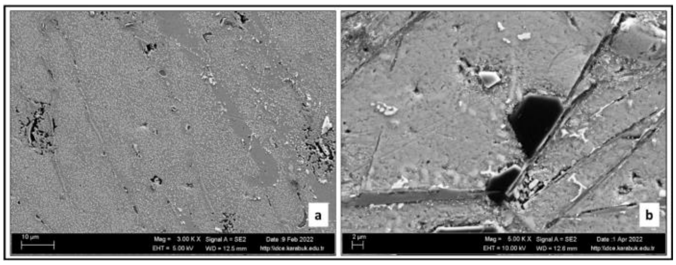

Fig. 2 SEM microstructures (a) Al7075 and (b) Al7075MHC

When the basic microstructures are examined, it is seen that an Al7075 alloy is consistent with the literature [8]. Particles are observed in the matrix phase in the composite sample. It is similar to the studies producing an Al matrix composite material [4]. Thus, the production of alloy and composite materials was completed in an arc melting system from powder materials.

The hardness test was reported as the average of 10 measurements. While the hardness value in the sample without reinforcement particles was 57 HV on average, this value reached an average of 110 HV in the produced composite. Diagonal measurement images obtained during the hardness test are given in Figure 3 [3, 9].

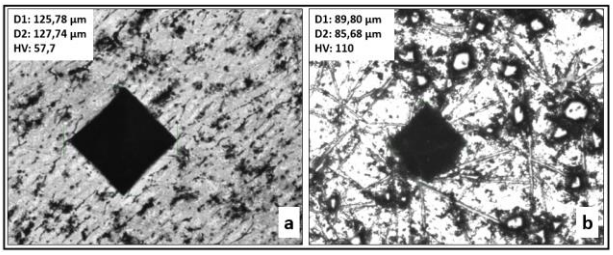

Fig. 2 Hardness test images (a) Al7075 and (b) Al7075MHC

Considering the trace image, the amount of diagonal area in different sizes shows that the hardness value is higher. Thus, the hardness value increased by 93% with the effect of particle reinforcement added to the Al matrix.

Particles added to the matrix structure caused the formation of different phases in the structure at high temperatures in the mini arc furnace. Since the bond energies of the new phases formed with the help of reinforcement particles are higher, the reaction of the hardness stinging tip has changed [10]. Due to this reason, an increase in hardness has occurred [2, 6, 8].

IV. CONCLUSIONS

In this study, a multi-hybrid composite was produced with SiC and B_4C reinforcement materials added to the Al7075 structure and this structure was compared with the base alloy. As a result of the production method and basic investigations, the following conclusions were reached.

1- A composite structure has been successfully formed with reinforcement elements in a mini arc furnace.

2- According to the microstructure images taken from the samples obtained, a composite material in which the particles are homogeneously dispersed was produced.

3- As a result of the micro hardness examination, an increase of 93% was observed in the composite material compared to the basic Al7075 alloy.

REFERENCES

[1] Looney, L., Monaghan, J., O'Reilly, P., Taplin, D. "The Turning of an Al/Sic Metal-Matrix Composite," *Journal of materials processing technology*, vol. 33, pp. 453-468, 1992.

[2] Karvanis, K., Fasnakis, D., Maropoulos, A., Papanikolaou, S., Production and Mechanical Properties of Al-Sic Metal Matrix Composites, IOP Conference Series: Materials Science and Engineering, IOP Publishing, (2016) 012070.

[3] Ravi, B., Naik, B. B., Prakash, J. U. "Characterization of Aluminium Matrix Composites (Aa6061/B4c) Fabricated by Stir Casting Technique," *Materials Today: Proceedings*, vol. 2, pp. 2984-2990, 2015.

[4] Myriounis, D., Hasan, S., Matikas, T. "Microdeformation Behaviour of Al–Sic Metal Matrix Composites," *Composite Interfaces*, vol. 15, pp. 495-514, 2008.

[5] Ozden, S., Ekici, R., Nair, F. "Investigation of Impact Behaviour of Aluminium Based Sic Particle Reinforced Metal–Matrix Composites," *Composites Part A: Applied Science and Manufacturing*, vol. 38, pp. 484-494, 2007.

[6] Muthukrishnan, N., Davim, J. P. "An Investigation of the Effect of Work Piece Reinforcing Percentage on the Machinability of Al-Sic Metal Matrix Composites," *Journal of Mechanical Engineering Research*, vol. 3, pp. 15-24, 2011.

[7] Chen, J.-P., Gu, L., He, G.-J. "A Review on Conventional and Nonconventional Machining of Sic Particle-Reinforced Aluminium Matrix Composites," *Advances in Manufacturing*, vol. 8, pp. 279-315, 2020.

[8] Taleghani, M. J., Navas, E. R., Torralba, J. "Microstructural and Mechanical Characterisation of 7075 Aluminium Alloy Consolidated from a Premixed Powder by Cold Compaction and Hot Extrusion," *Materials & Design*, vol. 55, pp. 674-682, 2014.

[9] Maqbool, A., Hussain, M. A., Khalid, F. A., Bakhsh, N., Hussain, A., Kim, M. H. "Mechanical Characterization of Copper Coated Carbon Nanotubes Reinforced Aluminum Matrix Composites," *Materials Characterization*, vol. 86, pp. 39-48, 2013.

[10] He, H., Rong, Y., Zhang, L. "Molecular Dynamics Studies on the Sintering and Mechanical Behaviors of Graphene Nanoplatelet

Reinforced Aluminum Matrix Composites," *Modelling and Simulation in Materials Science and Engineering*, vol. 27, pp. 065006, 2019.

Investigating the Dynamic Compression Response of a Novel Lattice Topology via Finite Element Analyses

Hubannur Seremet*, Nazim Babacan*,

* *Department of Mechanical Engineering, Sivas University of Science and Technology,*
Sivas 58140, Turkey
hubansrmt@gmail.com; nazimbabacan@sivas.edu.tr

***Abstract*—Selective laser melting (SLM) method, which is among the most popular metal additive manufacturing technologies, is used to fabricate complex lattice structures that are difficult to manufacture with conventional manufacturing technologies. As one of complex structures, lattice geometries have shown great potential in a wide variety of engineering applications due to their high specific strength, rigidity and energy absorbing ability. The unit-cell topology of these structures is one of the main parameters that determine their mechanical performance; hence, it is crucial. In this study a novel unit-cell design, named as BCCZZ was created by adding extra interior vertical struts to BCCZ structure. As a comparison, body-centered cubic (BCC) and BCCZ lattice types were also designed. Ti-6Al-4V alloy, which is a very popular metal alloy produced with SLM was chosen as a material. Finite element analyses were done to simulate the dynamic compressive behavior of selected lattice structures. Resulting stress-strain curves and collapse response of the structures were compared and the findings showed that BCCZZ, the novel design, exhibits the best performance in terms of specific strength compared to BCC and BCCZ samples. Therefore, this geometry could be potential in the load-bearing applications where the lightweight is important.**

***Keywords*— selective laser melting, Ti-6Al-4V, lattice structures, mechanical properties, finite element analysis**

I. INTRODUCTION

Lattice structures with regular cell topologies have attracted significant attention in recent years. Due to their high specific strength, high specific modulus, and energy absorption capabilities, these parts can be a used in many industrial areas such as automobile and aerospace applications [1–4]. Additive manufacturing (AM) technology shows great advantage in fabricating complex three-dimensional (3D) structures, providing an efficient way to prepare and optimize lattice materials [5-8]. Selective laser melting (SLM) or in other terms; laser powder bed fusion (LPBF) technology, as the pioneering in AM, scans the metal powders laid on a construction platform with the laser beam until it creates the designed geometry [9]. Compared to traditional production techniques, it has a higher level of flexibility, higher material usage rate, and a production close to net shape without relying on expensive molds. It also provides excellent control over the internal morphology of the lattice structures, enabling the production of complex geometries and the processing of materials with high hardness and high melting point [10-14]. The most commonly used SLM metallic materials, Ti alloys, or more specifically Ti-6Al-4V, have undergone extensive research due to their low density, high strength and good corrosion resistance [15-18].

Body-centered cubic (BCC) and body-centered cubic with vertical strut structures (BCCZ) are among the most common strut-based cell topologies [19, 20]. Gümrük and Mines [21] studied the behavior of stainless-steel BCC lattice structures under compression and found that a localized deformation occurs at the center of the lattice structure as the surrounding struts gradually crush. In addition, Lei et al. [22] compared the compressive behavior of BCC and BCCZ AlSi10Mg lattice structures and it was seen that the vertical increase the compressive strength. Although the relative density of the BCCZ samples increased slightly, the compressive modulus and initial crush strength increased by 1.7 and 2.5 times, respectively compared to the BCC samples. Therefore, modifications in the cell topology such as adding extra vertical struts could be a good option to provide a significant increase in mechanical strength and stiffness without significantly increasing the weight of these lattice structures.

In addition to experiments, one of the most used methods to examine the mechanical properties of lattice structures is finite element analysis. This numerical method is an alternative and/or supporting tool for predicting the mechanical behavior of the complex structures which is experimentally costly and time-consuming [23]. Johnson-Cook strength and failure model is one of the most popular and frequently used models in order to simulate the dynamical behavior of the materials [24]. This model enables to predict the mechanical behavior of the materials by considering many parameters such as yield strength, strain rate, geometrical features and temperature.

In this study, a novel lightweight lattice structure design (namely; BCCZZ) which could be efficient in terms of specific strength and stiffness was created. Load-bearing capacity of BCCZZ Ti-6Al-4V alloy were evaluated via FE method under dynamic compressive loads by utilizing Johnson-Cook material model. Similarly BCC and BCCZ lattice structures were modelled and analysed as a comparison. Finally, stress-strain curves of these structures as well as deformation behavior were discussed to reveal the efficiency of the novel design.

II. MATERIALS AND METHOD

A. *Design of Lattice Structures*

Three-dimensional models of the BCC, BCCZ and BCCZZ mesh material were developed in Solidworks software. The unit cell dimensions and the strut diameter of all structures were chosen as 5×5×5 mm^3 and 0.8 mm, respectively as seen in Fig. 1. Unit cell repeats periodically along the *x*, *y*, and *z* axes of a cartesian, and the number of cells in each direction is 4. Relative densities (the parameter shows how much dense the structure relative to a fully dense structure) of the designed BCC, BCCZ and BCCZZ structures are 0.119, 0.134 and 0.164, respectively.

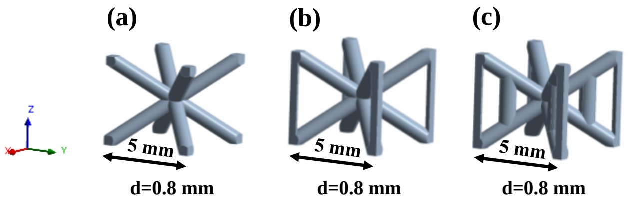

Fig. 1 Unit cell and dimensions of lattice structures (a) BCC, (b) BCCZ, (c) BCCZZ

B. *Finite Element Modelling*

Johnson-Cook materials model parameters of Ti-6Al-4V alloy were adapted from the study of Jin et al. [25]. These parameters are presented in Table 1.

Dynamic numerical analyses were done using Ansys/Explicit Dynamic. Structural steel plates with 0.5 mm thickness were added as bottom and top plates to simulate the compression test response of the lattice structures more realistic. 0.2 frictional coefficient was defined between the plates and the lattice geometry. While linear tetrahedron elements were used to mesh the lattice parts, top and bottom plates were meshed with hexagon elements. Element size was chosen as 0.35 mm after implementing a mesh dependency study. Finite element meshes of whole structures in 2D as well as highlighted models of unit cells are shown in Fig. 2. The bottom plate was fixed in all directions and 6 m/s downward speed was applied to the top plate to simulate dynamic compressive response of the lattice structures as seen in Fig. 3.

TABLE I
Johnson-Cook Strength and Damage Parameters of Ti-6Al-4V used in this study [25]

A	***B***	***C***	***m***	***n***
1288	321	0.0127	0.718	1.184
D_1	D_2	D_3	D_4	D_5
0.116	7.296	-8.692	0.0111	1.53

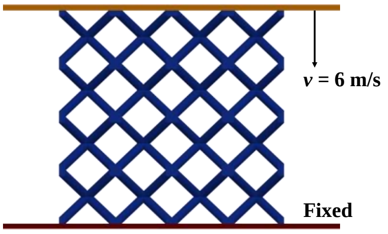

Fig. 3 Applied boundary conditions in the dynamic compression tests

III. RESULTS AND DISCUSSIONS

Firstly, a validation study was done to see the effectiveness of the model used for this study. Therefore, stress-strain curves obtained from the numerical dynamic compression tests were compared with the experimental and numerical results (Ls-Dyna) obtained by Jin et al. [25] as seen in Fig. 4. It should be noted that the geometrical parameters of BCC lattice and the boundary conditions used in this study are exactly same with the aforementioned work.

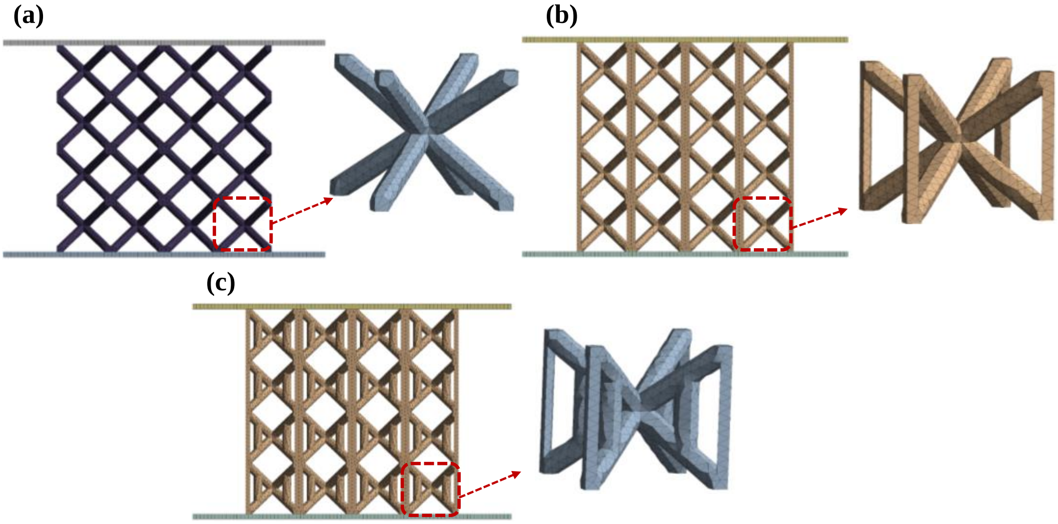

Fig. 2 2D view of meshed structures of each model (a unit cell was highlighted in each model) (a) BCC, (b) BCCZ, (c) BCCZZ

While the maximum stress value achieved in this work and the numerical study in [25] are almost same, initial slopes are slightly different. On the other hand, the maximum experimental stress values in [25] are lower compared to both numerical results. This discrepancy was attributed to the rough surfaces and pore defects occurred by SLM. Nevertheless, it is seen that our model more successfully simulated the near-constant progression of the stress after reaching the highest value. As a conclusion, it has proven that the trend of the numerically estimated stress-strain curve is consistent with the experimental results and the FE model used in this model is reliable.

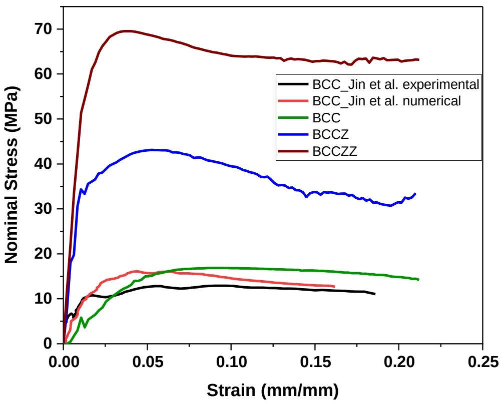

Fig. 4 Nominal stress-strain curves obtained from the numerical dynamic compression tests of BCC, BCCZ and BCCZZ lattice structures. (The numerical and experimental curves belong to study of [25] are also added for comparison.)

The elastic modulus and initial peak stress values of BCCZ structure are higher compared to BCC as expected. The most interesting result of this study is the high mechanical properties belong to the novel BCCZZ design. While the initial peak stress is close to 70 MPa which is almost 1.7 times of that of BCC, a higher elastic modulus was obtained compared to counterparts. Although the relative density of BCCZZ is 1.22 times higher than BCCZ, the strength ratio is much larger. Thus, BCCZZ lattice design has the highest specific strength capability among all three lattice structures.

In order to better understand the dynamic compressive response of these lattice structures, their deformation behavior under 10% and 20% applied strain values are compared by considering equivalent von Mises stress distribution as seen in Fig. 5 and 6, respectively. BCC lattice sample deformed more homogenously without exhibiting any localized failure different than the BCCZ and BCCZZ samples. The main failure mode of BCC sample is the collapse of the top and bottom cells However, BCCZ structure show localized buckling during the deformation through its vertical struts of and shear bands occurred at the angle of 45° as the strain was increased as highlighted with red rectangles in Fig. 6 (b). In other terms, local buckling in the BCCZ structure results in global buckling at 20% strain along the diagonal line of the specimen. Similar collapse response was also observed in the studies of Smith et al. [26] and Maconachie et al. [27]. Although local buckling of the vertical struts is present in BCCZZ sample, it is not as prominent as in BCCZ sample by showing the strengthening effect of additional vertical struts in the novel design. The highest collapse is seen in the vertical struts at very right and left of the structure.

The highest stress values are seen at the node intersections of BCC sample as evidenced in Figs. 5 and 6 (a). Stress values at the side node intersections are higher compared to middle ones. However, von Mises stress values at the vertical struts are the highest in BCCZ lattice structure and difference in the stress between vertical and oblique struts is more prominent especially at 10% strain value. As the strain progress, local buckling becomes more dominant and stress values decrease which is also observed in the overall stress-strain curve located in Fig. 4. On the other hand, the maximum stress values are observed in the interior vertical struts which were added in this novel design. It demonstrates the effective load-bearing capacity of these struts and, thus the effectiveness of the novel design.

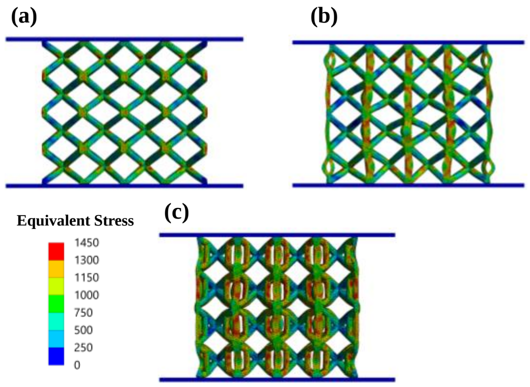

Fig.5 Collapse behavior of the (a) BCC, (b) BCCZ, (c) BCCZZ lattice structures under 10% compressive strain by presenting equivalent (von Mises) stress distribution

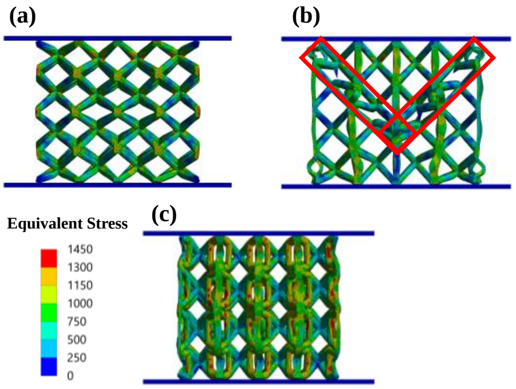

Fig. 6 Collapse behavior of the (a) BCC, (b) BCCZ, (c) BCCZZ lattice structures under 20% compressive strain by presenting equivalent (von Mises) stress distribution

IV. CONCLUSIONS

This study has shown the dynamic numerical response of the novel BCCZZ lattice structure by comparison with frequently used BCC and BCCZ structures. The outcomes include the following:

- BCCZZ structure exhibited the superior specific strength that proves the its potential load-bearing capacity for lightweight applications.
- Although local buckling is seen in BCCZZ structure, it is not as pronounced as observed in BCCZ lattice. BCC showed the most stable collapse behavior.
- Additional interior vertical struts in the novel design are exposed to highest stress values, while BCC and BCCZ exhibit the maximum stresses at the node intersections and vertical struts, respectively.

ACKNOWLEDGMENT

This study was supported by the Alexander von Humboldt (AvH) Foundation Return Fellowship program.

REFERENCES

[1] T. A. Schaedler, A. J. Jacobasen, A. Torrentleri and A. E. Sorensen, "Ultralight metallic microlattices," *Science (80-.).*, vol. 334, no. 6058, pp. 962–965, Nov. 2011.

[2] L. R. Tang, S. Das, and J. R. Greer, "Strong, lightweight, and recoverable three-dimensional ceramic nanolattices," *Science (80-.).*, vol. 345, no. 6202, pp. 1322–1326, Sep. 2014.

[3] M. S. Pham, C. Liu, I. Todd, and J. Lertthanasarn, "Damage-tolerant architected materials inspired by crystal microstructure," *Nat. 2019 5657739*, vol. 565, no. 7739, pp. 305–311, Jan. 2019.

[4] A A. Banerjee, D. Bernoulli, H. Zhang and M. F. Yuen, "Ultralarge elastic deformation of nanoscale diamond," *Science (80-.).*, vol. 360, no. 6386, pp. 300–302, Apr. 2018.

[5] S. L. Lu, M. Qian, H. P. Tang, M. Yan, J. Wang, and D. H. StJohn, "Massive transformation in Ti–6Al–4V additively manufactured by selective electron beam melting," *Acta Mater.*, vol. 104, pp. 303–311, Feb. 2016.

[6] J. A. Harris, R. E. Winter, and G. J. McShane, "Impact response of additively manufactured metallic hybrid lattice materials," *Int. J. Impact Eng.*, vol. 104, pp. 177–191, Jun. 2017.

[7] G. Campoli, M. S. Borleffs, S. Amin Yavari, R. Wauthle, H. Weinans, and A. A. Zadpoor, "Mechanical properties of open-cell metallic biomaterials manufactured using additive manufacturing," *Mater. Des.*, vol. 49, pp. 957–965, Aug. 2013.

[8] E. Chauvet, C. Tassin, J. J. Blandin, R. Dendievel, and G. Martin, "Producing Ni-base superalloys single crystal by selective electron beam melting," *Scr. Mater.*, vol. 152, pp. 15–19, Jul. 2018.

[9] W. J. Sames, F. A. List, S. Pannala, R. R. Dehoff, and S. S. Babu, "The metallurgy and processing science of metal additive manufacturing," vol. 61, no. 5, pp. 315–360, 2016.

[10] I. Ullah, M. Brandt, and S. Feih, "Failure and energy absorption characteristics of advanced 3D truss core structures," *Mater. Des.*, vol. 92, pp. 937–948, Feb. 2016.

[11] Z. Wang, K. Guan, M. Gao, X. Li, X. Chen, and X. Zeng, "The microstructure and mechanical properties of deposited-IN718 by selective laser melting," *J. Alloys Compd.*, vol. 513, pp. 518–523, Feb. 2012.

[12] A. P. Roberts, T. B. Sercombe, G. Graysan, V. J. Challis, L.C. Zhang, J.F. Grotowski and G. B. Schaffer, "Elastic moduli of sintered powders with application to components fabricated using selective laser melting," *Acta Mater.*, vol. 59, no. 13, pp. 5257–5265, Aug. 2011.

[13] J. H. Liu, W. J. Xie, W. Qingsong, and W. Li, "Progress on Investigation of Pores During Selective Laser Melting of Metal Powders and Future Work Discussion," *Adv. Mater. Res.*, vol. 291–294, pp. 3088–3094, 2011.

[14] L. Thijs, F. Verhaeghe, T. Craeghs, J. Van Humbeeck, and J. P. Kruth, "A study of the microstructural evolution during selective laser melting of Ti–6Al–4V," *Acta Mater.*, vol. 58, no. 9, pp. 3303–3312, May 2010.

[15] L. S. Bertol, W. K. Júnior, F. P. da Silva, and C. Aumund-Kopp, "Medical design: Direct metal laser sintering of Ti–6Al–4V," *Mater. Des.*, vol. 31, no. 8, pp. 3982–3988, Sep. 2010.

[16] A. A. Zadpoor and J. Malda, "Additive Manufacturing of Biomaterials, Tissues, and Organs," *Ann. Biomed. Eng.*, vol. 45, no. 1, pp. 1–11, Jan. 2017.

[17] S. A. Yavari, R. Wauthle, J. Van der Stok and A.C. Riemslag, "Fatigue behavior of porous biomaterials manufactured using selective laser melting," *Mater. Sci. Eng. C*, vol. 33, no. 8, pp. 4849–4858, Dec. 2013.

[18] R. Wauthle and J. V. Humbeeck, "Revival of pure titanium for dynamically loaded porous implants using additive manufacturing," *Mater. Sci. Eng. C*, vol. 54, pp. 94–100, Sep. 2015.

[19] Q. Feng, Q. Tang, Z. Liu, Y. Liu, and R. Setchi, "An investigation of the mechanical properties of metallic lattice structures fabricated using selective laser melting," *Proc. Inst. Mech. Eng. Part B J. Eng. Manuf.*, vol. 232, no. 10, pp. 1719–1730, Aug. 2018.

[20] X. Geng, L. Ma, C. Liu, C. Zhao, and Z. F. Yue, "A FEM study on mechanical behavior of cellular lattice materials based on combined elements," *Mater. Sci. Eng. A*, vol. 712, no. November 2017, pp. 188–198, 2018.

[21] R. Gümrük and R. A. W. Mines, "Compressive behaviour of stainless steel micro-lattice structures," *Int. J. Mech. Sci.*, vol. 68, pp. 125–139, Mar. 2013.

[22] H. Lei *et al.*, "Evaluation of compressive properties of SLM-fabricated multi-layer lattice structures by experimental test and μ-CT-based finite element analysis," *Mater. Des.*, vol. 169, May 2019.

[23] N. Jin, F. Wang, Y. Wang, B. Zhang, H. Cheng, and H. Zhang, "Failure and energy absorption characteristics of four lattice structures under dynamic loading," *Mater. Des.*, vol. 169, May 2019.

[24] R. Scazzosi, M. Giglio, and A. Manes, "Experimental and numerical investigation on the perforation resistance of double-layered metal shield under high-velocity impact of armor-piercing projectiles," *Materials (Basel)*, vol. 14, no. 3, pp. 1–20, 2021.

[25] N. Jin, Y. Wang, H. Cheng, X. Cheng, and H. Zhang, "Strain Rate and Structure Dependent Behavior of Lattice Structures of a Titanium Alloy Fabricated by Selective Laser Melting," *J. Dyn. Behav. Mater.*, vol. 8, no. 1, pp. 57–72, Mar. 2022.

[26] M. Smith, Z. Guan, and W. J. Cantwell, "Finite element modelling of the compressive response of lattice structures manufactured using the selective laser melting technique," *Int. J. Mech. Sci.*, vol. 67, pp. 28–41, 2013.

[27] T. Maconachie, M. Leary, P. Tran, J. Harris, Q. Liu, G. Lu, D. Ruan, O. Faruque and M. Brandt, "The effect of topology on the quasi-static and dynamic behaviour of SLM AlSi10Mg lattice structures," *Int. J. Adv. Manuf. Technol.*, vol. 118, pp. 4085–4104, Oct. 2021.

Effects of La addition to Mg-2Zn-1Mn alloys

Halil Ahmet Gören[*], Mehmet Ünal, Yunus Türen, Hayrettin Ahlatçı

[#] *Mechatronics Program, Sinop University, Sinop, Turkey, agoren@sinop.edu.tr*

Department of Manufacturing Engineering, Karabuk University, Karabuk, Turkey, munal@karabuk.edu.tr

Department of Metallurgical and Materials Engineering, Karabuk University, Karabuk, Turkey, (yturen@karabuk.edu.tr, hahlatci@karabuk.edu.tr)

***Abstract*—In this study, 0.5% by weight Lanthanum element was added to Mg-2Zn-1Mn alloy. The effect of this element on the microstructure and mechanical properties of the alloys was investigated. The alloys was cast into a metal mold with a graphite crucible in an induction furnace. Casting, homogenization and then rolling were done. MgZn, $MgZn_2$, $MgZn_3$, $MnZn_3$ phases were detected in the alloys. With the addition of 0.5La, $LaZn_2$ and $LaMg_3$ phases were formed. Intermetallic phases increased with the addition of La in the microstructure. The hardness increased with the addition of La and rolling. Addition of La as casting reduced the strength properties. Strength increased with rolling.**

***Keywords*— Magnesium, Mg-2Zn-1Mn, Casting, La, Rolling**

I. INTRODUCTION

Mg alloys are widely preferred by aerospace, automotive, electronics and various other industries due to their light weight and high specific strength [1]. Magnesium is a very effective material due to its superior properties such as strength and machinability, and it has good castability under controlled atmosphere [2].

Recently, Mg-Zn series alloys containing non-toxic elements and therefore not requiring surface treatment have shown great potential as implant materials. However, the addition of large amounts of alloying elements significantly reduces corrosion resistance. especially when the Zn content is greater than 3% by weight [3].

Among magnesium alloys, Mg-Zn based alloys are one of the most widely used magnesium alloys [4,5]. The addition of Zn plays a role in solution hardening. Ying et al. investigated the thermal properties of Mg-Zn alloys in their study and found that the thermal conductivity of the alloys decreased significantly with increasing Zn composition [6].

There are few studies in the literature on Mg-2Zn-1Mn alloy with the addition of lanthanum. However, there are studies on different alloys with the addition of La [7]. In this paper, samples of cast, homogenized and rolled Mg-2Zn-1Mn alloys were prepared. Microstructure and mechanical properties have been studied.

II. EXPERIMENTAL STUDİES

Alloys were poured into a metal mold at 250°C with a graphite crucible in an induction furnace at 750°C using shielding gases Argon and CO_2+$1SF_6$. Then, a part of the cast part was homogenized at 400°C, 16h [8]. It was then rolled with a rolling ratio of 80%, a rolling speed of 4.7, and a constant degree of deformation of (φ= 0.2).

Prior to the OM and SEM observations, mechanically ground and polished samples were etched with a mixture of 6 g picric acid, 5 ml acetic acid, 10 ml distilled water and 100 ml ethanol. Microstructure observations were then performed by a Nikon optical microscope (OM). (SEM), (XRD), (XRF) tests were performed.

The chemical compositions of the produced alloys after casting were determined by XRF (X-Ray Fluorescence) method using a Rigaku ZSX Primus II brand device.

In the Vickers hardness test, it was kept under a 0.3 kg load with a pyramid-shaped penetrating tip for 15 seconds and the hardness values were determined by measuring the trace diameters. Tensile tests on the samples were carried out on a Zwick/Roell Z600 tensile device, at a tensile speed of 1.67x10-3 s-1 and at room temperature. At least 3 samples were prepared for the tensile test from all alloys.

III. EXPERIMENTAL RESULTS

A. XRF Results

In this method, the weight % ratios of alloying elements were determined by making use of secondary radiations with different wavelengths specific to each element, called fluorescence. The chemical compositions of the alloys were obtained as a result of the XRF tests applied to the samples after casting and are presented in Table 1.

TABLE I. Cemical composition of alloys

Alloys	**Cemical Compositions (% Weight)**				
	Zn	**Mn**	**La**	**Al**	**Mg**
Mg-2Zn-1Mn	**2.05**	**1.05**	**-**	**0.02**	**Bal.**
Mg-2Zn-1Mn-0.5La	**2.02**	**1.14**	**0,67**	**0.01**	**Bal.**

B. XRD Results

The results of the XRD test performed on the samples taken as cast from Mg-2Zn-1Mn alloys are given in Figure 3. The presence of MgZn, $MgZn_2$, $MgZn_3$, $MnZn_3$, $LaZn_2$, $LaMg_3$ binary phases was determined in the microstructure of the alloys.

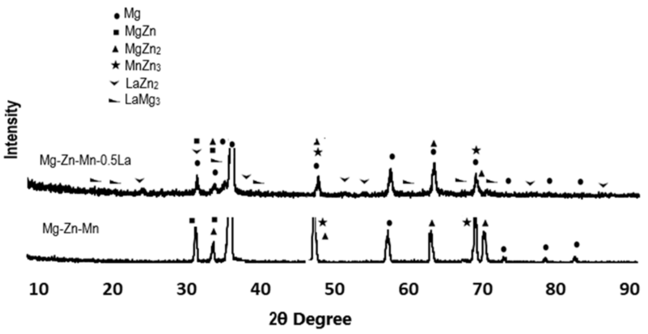

Fig. 1 XRD results of Mg-2Zn-1Mn-alloys

C. *Microstructure Results*

When the microstructure of the cast Mg-2Zn-1Mn alloy is examined in Figure 2, it is seen that the α-Mg phase turns into a finer grain structure with the effect of recrystallization formed by rolling.

When the microstructure of the Mg-Zn-Mn-La alloy seen in Figure 3 is examined, $LaZn_2$, $LaMg_3$ phases were formed in addition to the previous phases.

While a coarser grain structure is observed in the La added alloy as casting, it is seen to have a finer grain structure as rolling.

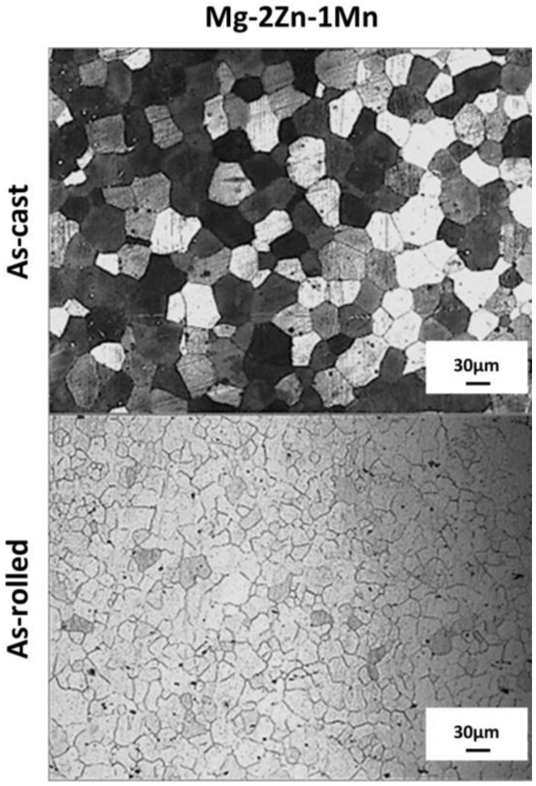

Fig. 2 Microstructure images of Mg-2Zn-1Mn alloys

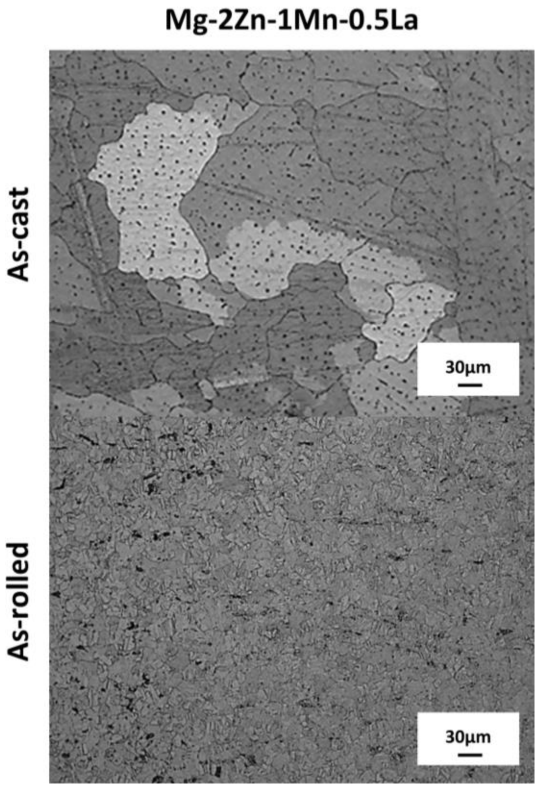

Fig. 3 Microstructure images of Mg-2Zn-1Mn-0.5La alloys

D. *SEM Results*

When the SEM images of the Mg-2Zn-1Mn alloy seen in Figure 4 are examined as casting and rolling, it is seen that intermetallic phases such as MgZn, $MgZn_2$, $MgZn_3$, $MnZn_3$ are distributed along the grain boundaries.

When the images in Figure 5 are examined, $LaZn_2$, $LaMg_3$ intermetallic phases are formed with the addition of La.

It has been observed that the phases formed in the grain boundaries and matrix elongate along the rolling direction with the effect of recrystallization.

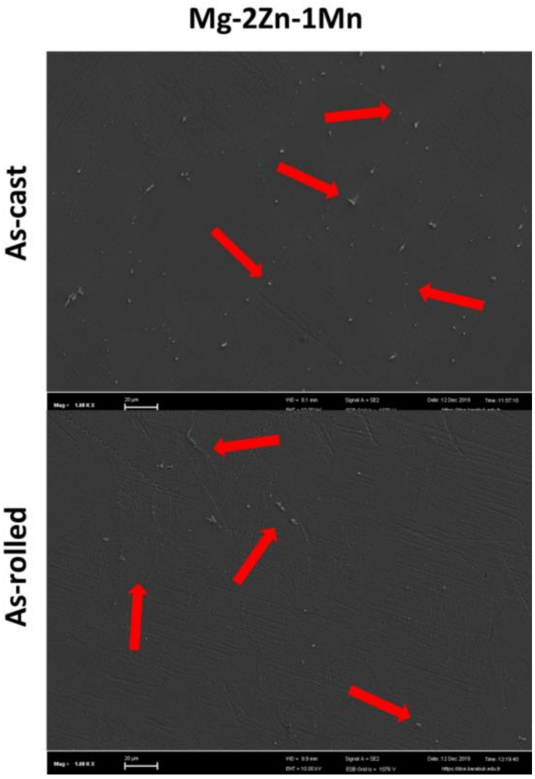

Fig. 4 SEM images of Mg-2Zn-1Mn alloys

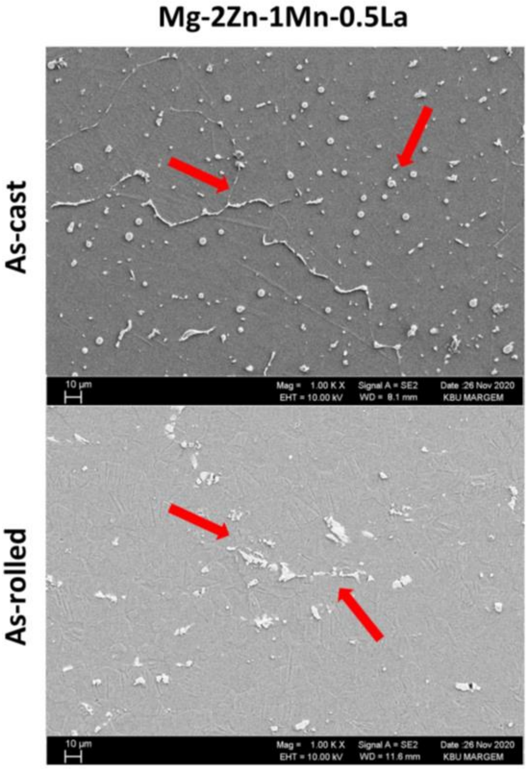

Fig. 5 SEM images of Mg-2Zn-1Mn-0.5La alloys

E. *Hardness Test Results*

Vickers hardness (HV) values of the alloys are given in Figure 6 below. It was observed that the hardness increased at each stage with the addition of La. It was also observed that refining the grain size with the effect of recrystallization by rolling increased the hardness.

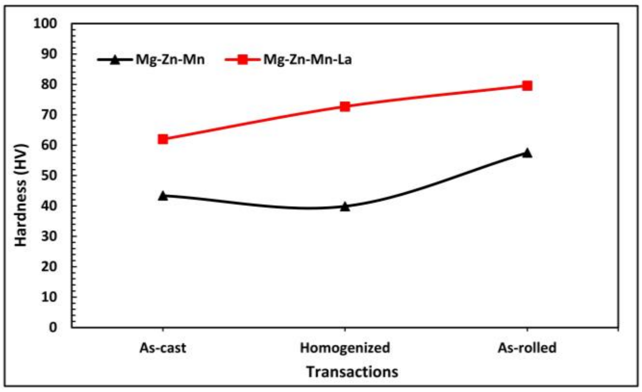

Fig. 6 Hardness (HV) results of alloys

F. *Tensile Test Results*

When the tensile test results are examined, the addition of 0.5% La to the Mg-2Zn-1Mn alloy as casting in Figure 7 shows that the Tensile test decreased by 21.76%, the yield strength decreased by 30.72%, and the Elongation decreased by 36.23%.

The Tensile value of the Rolled Mg-2Zn-1Mn alloy in Figure 8 increased by 58.82% compared to Figure 7. It was observed that the Tensile strength value of the rolled Mg-2Zn-1Mn-0.5La alloy in Figure 8 increased by 96.99% compared to Figure 7.

With the addition of La to the rolled Mg-2Zn-1Mn alloy in Figure 8, the Tensile Strength decreased by 3%, the yield strength increased by 7.14% and the Elongation value decreased by 36.23%.

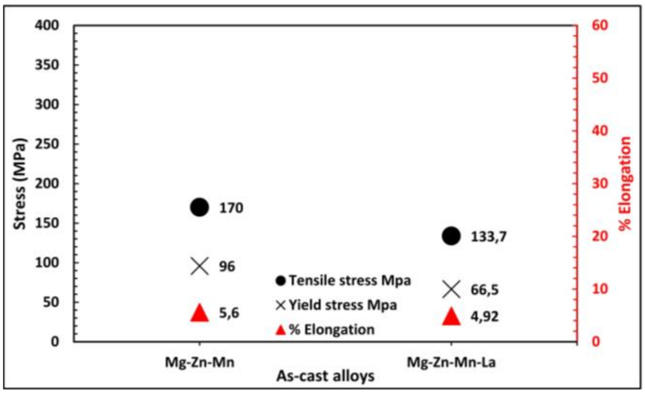

Fig. 7 Tensile stress (Mpa), Yield stress (Mpa), % Elongation results of as-cast alloys

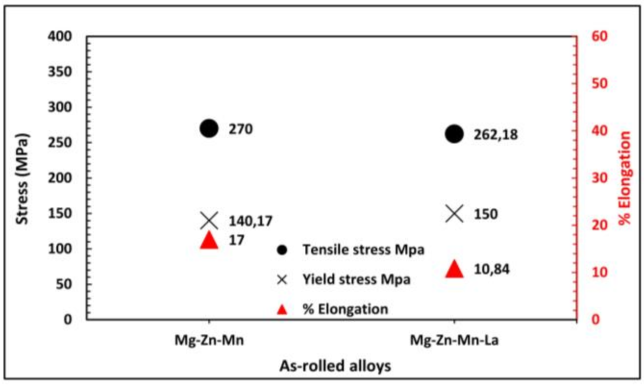

Fig. 8 Tensile stress (Mpa), Yield stress (Mpa), % Elongation results of as-rolled alloys

IV. CONCLUSIONS

MgZn, $MgZn_2$, $MgZn_3$, $MnZn_3$ phases were detected in Mg-2Zn-1Zn alloy and additional $LaZn_2$, $LaMg_3$ phases were formed in Mg-2Zn-1Zn-0.5La alloy.

When the microstructure was examined, it was observed that the intermetallic phases increased with La addition and the grain structure was refined as a result of recrystallization by rolling.

The hardness increased with the addition of La and rolling. With the addition of La as casting, Tensile strength, Yield strength, % Elongation values have decreased. As rolled Tensile strength, % Elongation values decreased and Yield strength increased.

ACKNOWLEDGMENT

This research is supported by Karabuk University Scientific Research Projects (BAP) with the project number KBU-BAP Project no: (FDK-2019-2103).

REFERENCES

[1] H. A. Gören, M. Ünal, E. Koç, ''A Comparative Study on Microstructure Properties of AZ91 Magnesium Alloy with Silicon Addition Using Ceramic Mold,'' *Acta Physica Polonica A.*, vol.135, 5, pp. 884-887, 2019.

[2] B. L. Mordike, T. Ebert, ''Magnesium: properties application-potential,'' *Mater. Sci. Eng.*, vol. 302, pp. 37-45, 2001.

[3] E. Zhang, D. Yin, L. Xu, L. Yang, K. Yang, ''Microstructure, mechanical and corrosion properties and biocompatibility of Mg–Zn–Mn alloys for biomedical application,'' *Mater. Sci. Eng. C.*, 29, pp. 987–993, 2009.

[4] X. Gao, J. F. Nie, ''Characterization of strengthening precipitate phases in a Mg-Zn alloy,'' *Scripta Materialia.*, 56, 8, pp. 645- 648, 2007.

[5] Gao X., J. F. Nie, ''Structure and thermal stability of primary intermetallic particles in an Mg-Zn casting alloy,'' *Scripta Materialia.*, 57, 7, pp. 655- 658, 2007.

[6] T. Ying, M. Y. Zheng, Z. T. Li, X.G. Qiao, S. W. Xu, ''Thermal conductivity of as-cast and as-extruded binary Mg-Zn alloys,'' *Journal of Alloys and Compounds*, 621, pp. 250-255, 2015.

[7] H. Zengin, Y. Türen, ''Effect of La content and extrusion temperature on microstructure, texture and mechanical properties of Mg-Zn-Zr magnesium alloy'', *Materials Chemistry and Physics.*, 214, pp. 421-430, 2018.

[8] M. Thirumurugan, S. Kumaran, S. Suwas, T. S. Rao, ''Effect of rolling temperature and reduction in thickness on microstructure and mechanical properties of ZM21 magnesium alloy and its subsequent annealing treatment,'' *Materials Science and Engineering: A.*, Vol. 528, 29–30, pp. 8460-8468, 15 Nov. 2011.

Investigation of Stress Distribution and Deformation Zones in Composite Sleepers by Finite Element Method

Mustafa Dursunlar*, Musa Yılmaz*, Ozan Yazar*, İsmail Aykut Karamanlı*

mustafa.dursunlar@yobu.edu.tr
*Yozgat Bozok University, Turkey

***Abstract*—In this study, the stress distribution and deformation regions of the composite sleepers was investigated using the finite element method. The composite sleepers in the study was computer-aided modeled with different matrix, fiber and tilt angle combinations. The loads applied to the composite sleepers was examined in terms of total deformation and stress with the help of ANSYS program. According to the results of the analysis, the stress values occur only in and around the load-applied parts of the composite sleepers. The most deformed regions are the upper layers, and the deformation decreases as one goes to the lower layers. The stress and deformation values in the middle and edge regions of the sleepers is close to zero, and these values are concentrated in the contact surface region of the rail and the sleepers. Finally, it is more appropriate to work on improving the design of the composite sleepers and increasing its lifespan, in areas where there are fasteners at the contact points of the rail and the sleepers.**

***Keywords*—Composite, Sleepers, Stress Analysis, Total Deformation, Finite Element Method**

I. INTRODUCTION

Railway sleepers, described as beams that run under the tracks and support the road, are traditionally made of wood, steel and concrete. The main functions of the sleepers is to transfer the load from the wheels from the rails to the subfloor with track ballast and to hold the rails at the correct height [1].

Due to the fact that railways play an important role in transport systems, the demand for sleepers is growing day by day. The premature failure of even perfectly ballasted sleepers has become a source of great interest in the last two decades. Wood, concrete and steel have been used as materials for sleepers for many years, with expected lifetimes of 20, 50 and 50 years respectively. It is estimated that there are currently about 3 billion sleepers on the world's rail networks. Over 400 million of these sleepers is made of concrete and 2-5% of them need to be replaced every year due to premature failure [2].

The ability of a sleepers to resist cracking, oxidation, chemical degradation, delamination and abrasion for a certain period of time under appropriate loading conditions and certain environmental conditions is critical. That's why new research and innovation is focused on the durability of sleepers [3].

An accurate study of the causes of premature failure of sleepers is necessary to minimize the cost of maintaining roads and increase their efficiency. The Australian Railways (ROA) studied 2,200 wooden sleepers on Queensland railway tracks to understand the causes and patterns of damage to wooden sleepers and analyzed 2,200 wooden sleepers for damage to the sleepers such as fungal rot, split ends, termites, stagnant sapwood, bombardment, cutting rails, weather conditions, studding and various causes found, including knots [4]. Of these types of damage, fungal rot (53%) [5], top splitting (10%) [6] and termite attacks (7%) [7] were identified as the main causes of sleepers damage.

The many advantages of concrete technology led to its use for sleepers in the 1950s. Today, about 500 million railway sleepers is made from prestressed concrete in the world's railway networks, and the demand for them annually accounts for more than 50% of the total demand [2]. According to the results of researchers from all over the world, the most common causes of concrete sleepers failures are; rail saddle deformation, center damage, derailment and impact damage [8], [9], [10] [11]. However, these types of failures can vary from country to country as the geometry and methods of operation differ.

Several studies have been carried out on damage to steel sleepers. The risk of corrosion, high electrical conductivity, fatigue cracking in the rail saddle area and the difficulty of filling with ballast make steel a less preferred material for sleepers [12], [13].

Investigation of the potential causes of the aforementioned failures of railway sleepers has shown that conventional materials do not meet the requirements of resistance to mechanical, biological and chemical degradation [14]. For this reason, researchers have focused on the research and development of new and efficient alternative sleepers technologies for the railway industry.

Today, the global market for composites is growing rapidly due to many advantages such as high strength-to-weight ratio, excellent resistance to corrosion, moisture and insects, and thermal conductivity [15]. This material can be developed according to the specific requirements of railway sleepers. Therefore, it is believed that composite railway sleepers may be a suitable alternative to existing concrete, steel and especially wood sleepers on both mainline and heavy-duty railway networks [16]. There are various classifications based on the number, length and direction of fibers in composite railroad sleepers which include technologies that are available or still under research and development [17, 18].

This study investigates the changes in stress magnitudes and strain magnitudes resulting from changes in matrix materials and fibers of different strengths and fiber laying angles in composite railroad sleepers that has been developed and widely used due to recent research. This is the guiding study for fatigue analysis and design improvements to be carried out later by determining the highest and lowest points of stress and strain.

II. MATERIAL AND METHODS

In the study, composite sleepers was obtained by combining 2 different epoxy matrices with 230 GPa and 395 GPa modulus of elasticity and 3 different carbon fibers with 230, 290 and 395 GPa modulus of elasticity at different tilt angles. These angle values for each combination are 150, 300 and 450. The sleepers created has the dimensions of 2135mmx230mmx115mm in accordance with the original [19]. The sleepers is designed as 10 layers with each layer thickness of 11.5 mm. The 2021 Academic version of the ANSYS Workbench program was used in the design.

Railway standards were taken into account while creating the loads. According to the standards, the maximum axle load of the rail vehicles used in the railways in our country is 22.5 tons [20]. Accordingly, since an axle is connected to two wheels, the maximum force acting on the sleepers from a railway wheel is divided by half of the axle load and can be accepted as 110,258 kN. It is also known that there is an angle of 1:40 between the contact surface of the rail and the sleepers [21]. This angle causes a shear force in the tavern. The forces acting on the sleepers is shown in Table I. In addition, the forces acting on the sleepers is schematically expressed in Figure 1.

Table I Forces acting on the sleepers

Force Direction	Force Direction	Force Dimension (kN)
X-axis	-X/+X	4.814
Y-axis	-Y	110.258

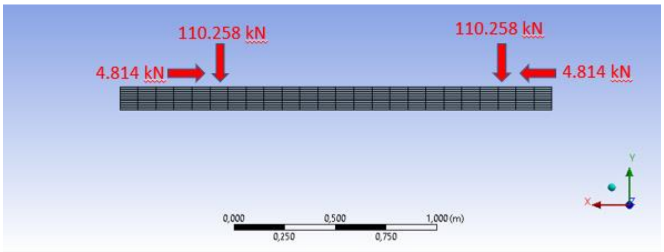

Fig. I Forces acting on the sleepers

In the analyses, the forces were acted on the surfaces where the rail contacted the sleepers. These surfaces are shown in Figure 2. Stress and total deformation analyzes were performed.

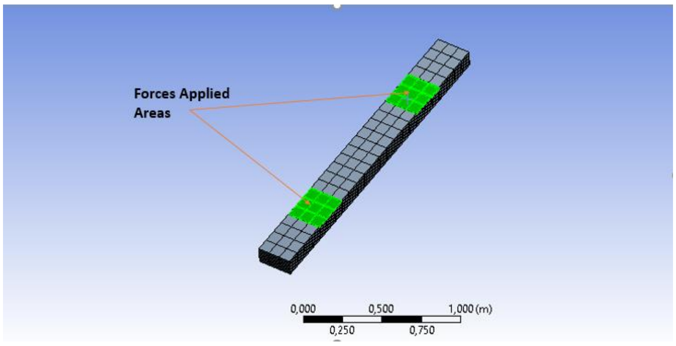

Fig. 2 Force application areas

III. IRESULTS

The maximum stress and total deformation values obtained as a result of the analyzes are shown in Table II.

Table II Maximum stress and total deformation values obtained as a result of the analyzes

EPOXY ELASTICITY MODULE (GPA)	**FIBER ELASTICITY MODULE (GPA)**	**ANGLE OF TILT (DEGREES)**	**MAX STRESS (MPA)**	**MAX TOTAL DEFORMATION (mm)**
230	230	15	0,77893	0,0014949
230	230	30	0,76991	0,0016031
230	230	45	0,63079	0,001707
230	290	15	0,78023	0,0014688
230	290	30	0,65246	0,0015936
230	290	45	0,65329	0,0017029
230	395	15	0,85601	0,004798
230	395	30	0,82007	0,0049783
230	395	45	0,90085	0,0055778
395	230	15	0,63681	0,0015077
395	230	30	0,63652	0,0017034
395	230	45	0,63149	0,001707
395	290	15	0,74896	0,0015224
395	290	30	0,64687	0,0016049
395	290	45	0,64784	0,0017026
395	395	15	0,85601	0,004798
395	395	30	0,82007	0,0049183
395	395	45	0,84197	0,0053135

Figure 3 and Figure 4 show the stress values and distribution obtained as a result of the analyzes performed on the sleepers. Accordingly, while the highest stress values are observed in the upper layers of the regions where the force is affected, the stress values decrease as one descends to the lower layers and moves away from the force effect region.

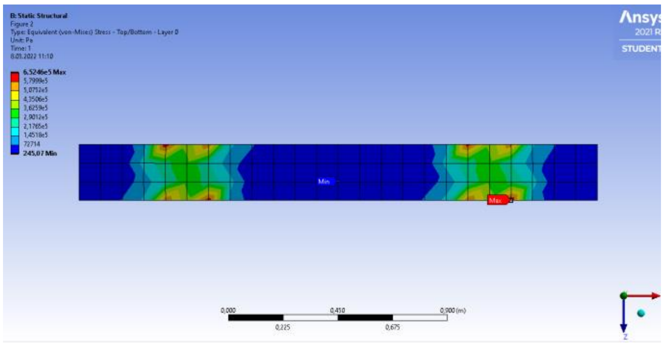

Fig. 3 Tension values and distribution of the sleepers, whose top view is given

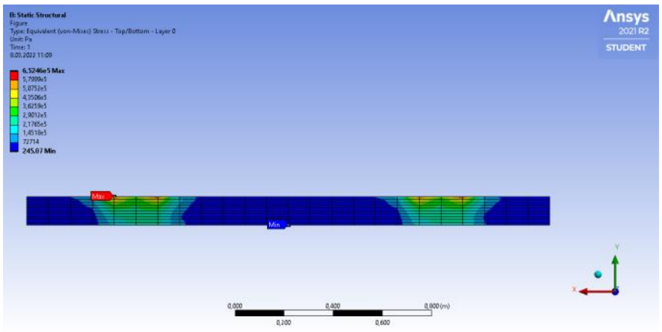

Fig. 4 Tension values and distribution of the sleepers, whose side view is given

Parallel to the stress value, the deformations are more intense in the force-affected regions of the sleepers and in the upper layers of these regions. As you move away from the mentioned regions and go down to the lower layers, the total deformation value also decreases. Total deformation values and distribution are shown in Figure 5 and Figure 6.

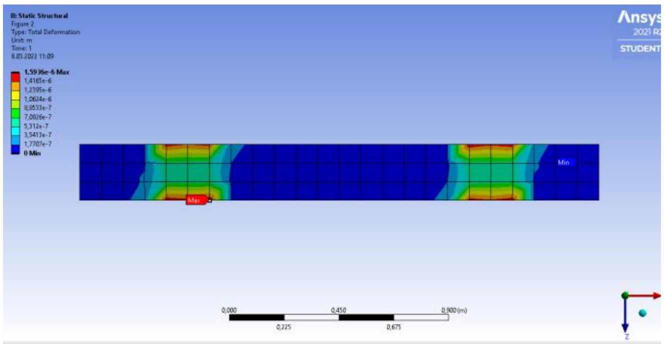

Fig. 5 The deformation values and distribution of the sleepers, whose top view is given

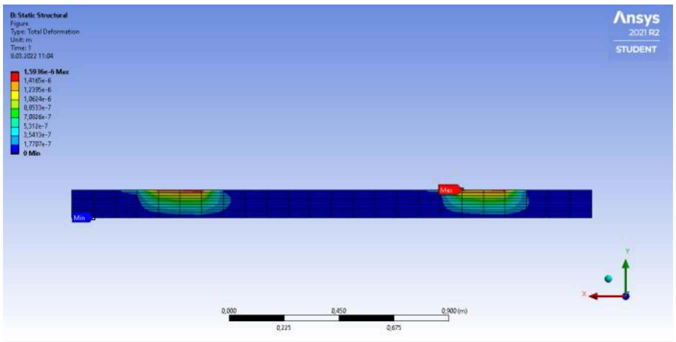

Fig. 6 Deformation values and distribution of the sleepers, which is given a side view

IV. CONCLUSIONS

In this study, composite sleepers was created with 2 different matrices, 3 different carbon fiber fibers and 3 different tilt angles. A total of 18 analyzes were made. As a result of the analysis;

- There is no tension in the edges and middle parts of the sleepers. The stresses are only seen in and around the areas where the load is applied. This means that in future studies to increase parameters such as strength and life; shows that it is necessary to concentrate on the regions and their surroundings where the load affects.
- Deformation values remained at acceptable levels in all analyses.
- While the stress created by the loading is most visible in the top layer, this effect decreases as you go to the lower layers and reaches negligible values. This shows that improvement works should be concentrated in the upper layers.
- As the elasticity modulus of the fiber fibers increases, the deformation and stress values also increase.

In this study, the stress and deformation values of a composite sleepers under load was investigated. The data obtained as a result of the study show parallelism with similar studies in the literature. In addition, this study will be a stepping stone for further improvement studies.

REFERENCES

[1] E.T. Selig and J.M. Waters, *Track geotechnology and substructure management*. 1994: Thomas Telford.

[2] Palomo, À., et al., *Railway sleepers made of alkali activated fly ash concrete.* 2007.

[3] Y. Zhang, M. Murray and L. Ferreria, *Track degradation prediction: criteria, methodology and models. 21st Australasian Transport Research Forum.* Adelaide, South Australia, 1997: p. 391-05.

[4] B. Hagaman and R. McAlpine, *ROA timber sleeper development project*. in *Conference on railway engineering: demand management of assets. ACT, Barton, Australia: Institution of Engineers*. 1991.

[5] J. Singh, *Dry rot and other wood-destroying fungi: their occurrence, biology, pathology and control.* Indoor and Built Environment, 1999. 8(1): p. 3-20.

[6] A. Manalo, et al., *A review of alternative materials for replacing existing timber sleepers.* Composite Structures, 2010. **92**(3): p. 603-611.

[7] M.A. Horwood and R. Eldridge, *Termites in New South Wales*. 2005: Forests NSW.

[8] J.C. Zeman, et al., *Failure mode and effect analysis of concrete ties in North America*. in *Proc. of the 9th International Heavy Haul Conference*. 2009.

[9] C. González-Nicieza, et al., *Failure analysis of concrete sleepers in heavy haul railway tracks.* Engineering Failure Analysis, 2008. **15**(1-2): p. 90-117.

[10] J.A. Zakeri and F.H. Rezvani, *Failures of railway concrete sleepers during service life.* International Journal of Construction Engineering and Management, 2012. **1**(1): p. 1-5.

[11] S. Kaewunruen and A.M. Remennikov, *Impact capacity of railway prestressed concrete sleepers.* Engineering Failure Analysis, 2009. **16**(5): p. 1520-1532.

[12] G. Zi, et al., *Investigation of a concrete railway sleeper failed by ice expansion.* Engineering Failure Analysis, 2012. **26**: p. 151-163.

[13] W.F. Langman, *Steel railroad sleeper*. 1983, Google Patents.

[14] W. Ferdous and A. Manalo, *Failures of mainline railway sleepers and suggested remedies–review of current practice.* Engineering Failure Analysis, 2014. **44**: p. 17-35.

[15] H.V. GangaRao, N. Taly and P. Vijay, *Reinforced concrete design with FRP composites*. 2006: CRC press.

[16] V. Gerard and M. Mckay, *Recent Australian developments in fibre composite railway sleepers.* Electronic Journal of Structural Engineering, 2013. **13**(1): p. 62-66.

[17] W. Ferdous, et al., *Composite railway sleepers–Recent developments, challenges, and future prospects.* Composite Structures, 2015. **134**: p. 158-168.

[18] A. Manalo and T. Aravinthan, *Behavior of full-scale railway turnout sleepers from glue-laminated fiber composite sandwich structures.* Journal of composites for construction, 2012. **16**(6): p. 724-736.

[19] W. Ferdous, et al., *Evaluation of an innovative composite railway sleeper for a narrow-gauge track under static load*. Journal of composites for construction, 2018. 22(2): p. 04017050.

[20] A. Andreas, *Load capacity assessment and strengthening of a railway arch bridge with backfill*, IABSE Spring Conference, 2013, p. 3-10.

[21] M.S. Sichani, R. Enblom and M. Berg, *Non-elliptic wheel-rail contact modelling in vehicle dynamics simulation*. Int J Railw Technol, 2014. 3: p. 77-96.

Cryogenic treatment effect on the mechanical and corrosion properties of 2024 aluminum alloy

Kamil Burak GÖÇMEN[1], Mustafa Özgür ÖTEYAKA[2]

[1]*Eskişehir Osmangazi University, Institute of science, Department of Aviation Science and Technology, Eskişehir/Turkiye*

kamilburakgocmen@gmail.com

[2]*Eskişehir Osmangazi University, Eskisehir Vocational School, Department of Electronic and Automation, Program of Mechatronic, 26140, Eskişehir/ Turkiye*

moteyaka@gmail.com

***Abstract*---Aluminum alloy was widely employed in aviation because of its lightweight, good mechanical properties, and corrosion resistance. In this study, deep cryogenic treatment with different treatment times was used to enhance the mechanical properties and corrosion resistance of 2024 aluminum alloy. For this purpose, tensile test, and electrochemical tests such as open circuit potential, potentiodynamic, and electrochemical impedance spectroscopy were performed on cryogenically treated samples. The findings showed an improvement of 8.3 % after 24 h of cryogenic treatment on the hardness of 2024- T3. However, the hardness decreased by 8.6 % for the sample 2024-T0 after a similar treatment. Regarding strength, the ultimate strength slightly increased for both samples following a cryogenic treatment of 8 h. On the other hand, the elongation was higher for the sample 2024-T0 for 8 h of cryogenic treatment. The free corrosion potential of untreated alloys performed more anodic behavior compared to treated alloy after 1 h of immersion in the 3.5 wt. % NaCl. The impedance resistance of the cryogenically treated sample was better compared to the untreated sample for both samples. The resistance of the oxide layer was improved after treatment of 8 h and 24 h for 2024-T0 and 2024-T3 alloys, respectively.**

***Keywords*---Aluminum alloy, 2024 alloy, tensile test, corrosion.**

Design and Manufacture of Dual Asymmetric Centrifuge Homogenizer

Fatih Huzeyfe Öztürk*, Özkan Öz

Industrial Design Engineering Department, Karabük University
Karabük, Turkey
fhozturk@karabuk.edu.tr
ooz@karabuk.edu.tr

***Abstract*— Proper mixing of particles is an essential requirement especially for medical laboratories and composite industry. Asymmetric centrifuge homogenizers were used to meet this requirement. In this study, unlike the similar devices in the market, a dual asymmetric centrifuge homogenizer with an independent mixing bowl speed was designed and manufactured. The efficiency of this new designed homogenizer was determined through mixing two component paste epoxy adhesive and carbon black. Two different mixing speed ratio and six different mixing bowl speed were considered in the mixing processes. As a result, the most proper mixing was achieved for the ratio of 1:-2 with mixing bowl speed of 800 rpm.**

***Keywords*— Homogenizer, asymmetric centrifuge, mixing**

I. INTRODUCTION

Mixing of materials is an important process step in a wide variety of industrial applications such as ceramics, metallurgy, chemistry, food, cosmetics, composites and pharmaceuticals [1-2]. In the mixing process, the mechanism of the mixer, properties of the mixed materials, mixing parameters and mixing principle are important for the quality of the final products [3].

In this study, a dual asymmetric centrifuge homogenizer was designed and manufactured for mixing or separation of particles. Compared to existing devices, the most important advantage of this device is that the rotation of the mixing bowl can be changed or stopped. This feature will allow the device to be used both as a homogenizer and a separator. Two component paste-like epoxy adhesive and carbon black were chosen as the materials to be mixed. Optimum mixing parameters were determined by visually examining the mixtures.

II. MATERIAL AND DESIGN

A. *Design and Manufacturing*

Within the scope of the study, a dual asymmetric centrifuge device was designed and manufactured to mix the materials which have different physical properties. The device performs rotational motion based on centrifugal motion. The basic principle of mixing and separation in this device depends on the rotation of the mixing bowl. This new design device can be used as a separator by stopping the rotation of the mixing bowls, or it can be used as a homogenizer if the mixing bowls are rotated. Proper mixing parameters can be obtained by adjusting the rotational speed of the main shaft and mixing bowls. To the best of our knowledge, asymmetric centrifuge homogenizers are not produced in Turkey and are supplied from abroad at very high costs. In addition, the mixing bowl speed of the existing devices cannot be changed. In existing devices, the rotational movement of the mixing bowl is provided by a gear wheel or pulley system connected to the main shaft. Unlike its counterparts, this new design can perform both mixing and separation processes and the mixing bowl speed can be controlled. Fig. 1 shows the dual asymmetric centrifuge homogenizer that was designed in Autodesk Fusion 360 program.

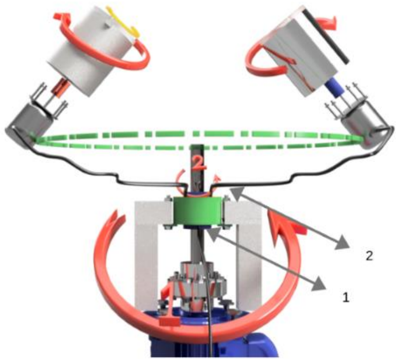

Fig. 1 Design of dual asymmetric centrifuge homogenizer

As shown in Fig. 1, mixing bowls with an angle of 45 degrees rotate around their own axis at speed ranges controlled by a driver. Mixing bowls and main shaft speeds can be independently controlled by the drives. The collector ring was fixed to the main body with bolts from the right and left sides with L profiles as shown as number 1 in Fig. 1. The inner part of the ring (number 2) rotates at a maximum speed of 2000 rpm. During the rotation of the main shaft, the lower part of the ring and the main cable that moves the mixing bowl motors connected to the lower part remain motionless.

The produced dual asymmetric centrifugal homogenizer is shown in Fig. 2.

Fig. 2 Dual asymmetric centrifugal homogenizer

B. *Preparation of Samples*

Structural two-component paste-like epoxy adhesive Araldite AV138 M-1 (Huntsman, Salt Lake, USA) and Monarch® 580 (Cabot Corporation Boston, USA) carbon black were used as raw materials. The properties of the adhesive and carbon black are given in Table I and Table II.

TABLE I
PROPERTIES OF ADHESIVE [4]

Property	AV 138 M-1 (Resin)	HV 998-1 (Hardener)	Mixed adhesive
Color (visual)	beige	grey	grey
Specific gravity	ca. 1.7	ca. 1.6	ca. 1.7
Viscosity (Pas)	thixotropic	thixotropic	thixotropic
Mix ratio (parts by weight)	100	40	-

TABLE III
PROPERTIES OF CARBON BLACK [5]

Density g/cm^3	Color	Specific weight g/cm^3
1.7-1.9	Black	0.02- 0.38

In mixing processes, adhesive mixture was prepared using mixing bowls of the dual asymmetric centrifugal homogenizer as shown in Fig.3. The total weight of the mixture was 50 gr. Weight of adhesive and carbon black is 45 gr. and 5 gr., respectively.

Fig. 3 Mixing process

Table III shows the mixing parameters of the homogenizer. The mixing times were kept constant as 5 min for all samples. The speed of mixing bowls and speed ratio were taken as a variable. In Table III, the speed ratio indicates the ratio between the rotational speed of the main shaft and mixing bowls.

TABLE IIII
MIXING PARAMETERS

Samples	Speed ratio	Mixing bowl speed (rpm)	Time (min)
A	1:-1	300	5
B	1:-1	600	5
C	1:-1	1200	5
D	1:-2	200	5
E	1:-2	400	5
F	1:-2	800	5

(-) sign in speed ratios indicates that the bowl rotation direction is opposite to the main shaft rotation

III. RESULT

Fig. 4 shows the samples which was mixed at the ratio of 1:1.

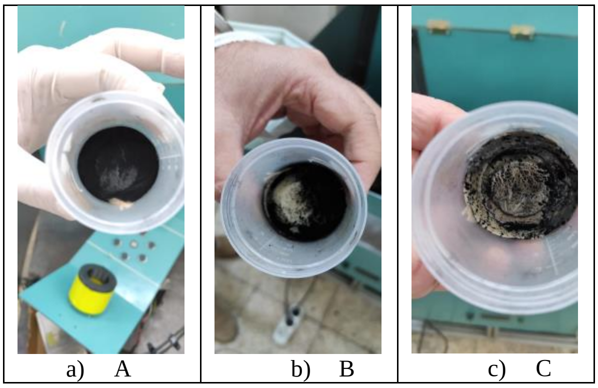

a) A b) B c) C

Fig. 4 A, B and C samples after mixing

For the speed ratio of 1:-1, grey and beige colors were observed in the mixtures. It can be concluded that the speed ratio of 1:-1 was not sufficient in the mixing of adhesive and carbon black. As the engine speed increased, it was observed that separation was more pronounced in samples B and C. These results showed that a speed ratio of 1:-1 could not be used in the mixing process.

Fig. 5 shows the samples which was mixed at the ratio of 1:-2.

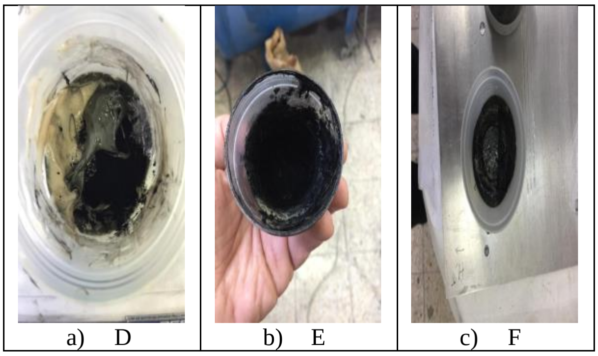
a) D b) E c) F

Fig. 5 D, E and F samples after mixing

For the ratio of 1:2, it was observed that the sample D did not mix properly. In the case of Sample E, carbon black was visually observed in the mixture. This observation indicated that the proper mixing was not achieved for the sample E. Sample F mixed with the speed ratio of 1:-2 and bowl speed of 800 rpm gave the most proper mixing among all the samples mixed. The grey colored homogeneous appearance obtained for sample F is the evidence of the proper mixing.

IV. CONCLUSION

In this study, a low-cost double asymmetric centrifugal homogenizer device based on the centrifugal movement principle, which provides homogeneous mixing and separation of materials, was designed, and produced. The efficiency of this new designed homogenizer was determined through mixing two component paste-like epoxy adhesive and carbon black. Two different mixing speed ratio and six different mixing bowl speed were considered in mixing processes. As a result, the most proper mixing was achieved for the ratio of 1:-2 with a mixing speed of 800 rpm.

ACKNOWLEDGMENT

This study was supported by TUBITAK 2209-B program.

REFERENCES

[1] Marigo, M., Cairns, D. L., Davies, M., Ingram, A., Stitt, E. H. 2012. A numerical comparison of mixing efficiencies of solids in a cylindrical vessel subject to a range of motions. Powder technology, Cilt. 217, s. 540-547, DOI: 10.1016/j.powtec.2011.11.016.

[2] Bellon, C., Truffer, C., Steiner, A., Moreillon, A., Nicolay, L. 2013. Mixing effectiveness of a new pneumatic PTS-Batchmixer® with an in-line sampling device. Advanced Powder Technology, Cilt. 24(1), s. 43-50, DOI: 10.1016/j.apt.2012.01.008.

[3] Mayer-Laigle, C., Gatumel, C., Berthiaux, H. 2015. Mixing dynamics for easy flowing powders in a lab scale Turbula® mixer. Chemical Engineering Research and Design, Cilt. 95, s. 248-261, DOI: 10.1016/j.cherd.2014.11.003.

[4] (2022) HUNTSMAN. MONARCH® 580 Specialty Carbon Black. http://www.cabotcorp.jp/~/media/files/product-datasheets/datasheet-monarch-580pdf.pdf. Accessed 3 March 2022.

[5] (2022) CABOT. Araldite® AV 138M-1 / Hardener HV 998-1. https://vitrochem.com/wordpress/wp-content/uploads/2021/04/Araldite-AV-138M-1-Hardener-HV-998-1_TDS.pdf. Accessed 3 March 2022.

Comparative Microstructure of Additively Manufactured Ti-6Al-4V Alloy by Electron Beam Melting and Selective Laser Melting

Yusuf Atilla SADIKOĞLU[1], Şeyma KÜÇÜK[1], Ozkan GOKCEKAYA[2], Takayoshi NAKANO[2], Hakan YILMAZER[1,*]

[1]Department of Metallurgical and Materials Engineering, Yildiz Technical University, 34220-Istanbul Turkey
[2]Division of Materials and Manufacturing Science, Graduate School of Engineering, Osaka University, 2-1, Yamadaoka, Suita, Osaka 565-0871, Japan
*Corresponding Author: hakanyil@yildiz.edu.tr

Abstract— **Additive manufacturing (3D printing) has many advantages over traditional production methods. Thanks to additive manufacturing, complex parts can be produced with low buy-to-fly rates. In this study, the optimization of production parameters and microstructure analysis of Ti-6Al-4V alloy produced by powder bed printing techniques, such as Electron Beam Melting (EBM) and Selective Laser Melting (SLM) methods were investigated. In both techniques, the pores can be reduced by optimizing the production parameters. When these techniques are compared, it is seen that the relative densities of the parts produced with SLM are higher than those produced with EBM, besides microstructure of SLMed parts is more needle-like. The microstructure analyses were carried out by optic microscope and scanning electron microscope investigations. Archimedes test was applied for relative density measurement.**

***Keywords*—Additive Manufacturing, Powder Bed Fusion (PBF), Electron Beam Melting (EBM), Selective Laser Melting (SLM), Ti-6Al-4V alloy**

I. INTRODUCTION

Additive Manufacturing (AM) has significant advantages in comparison to traditional manufacturing (TM) methods. AM provides the ability to manufacture complicated parts with unique shapes and structures and developing functional materials to alter the characteristics of a single part in strategic locations. In addition to the manufacture of materials with more than two pieces, AM can integrate two similar or dissimilar metals in one piece [1]. AM is a more cost-effective strategy that produces less waste material than TM. The unused powders from AM can be reused [2] and the raw material/part weight (buy-to-fly ratio) is low, while the buy-to-fly ratio varies between 10-20 in TM. This value can drop to 1 in parts produced with AM. It can be listed as not requiring any mold for the production of parts, thus saving time and cost [3].

Ti-6Al-4V is a titanium alloy containing 6 wt.% Al and 4 wt.% V in pure Ti matrix. The addition of an α stabilizer (Al) and β stabilizer (V) allows Ti-6Al-4V to keep dual-phase α+β at ambient temperature. However, the phase change of Ti64 is highly dependent on the temperature history and cooling rates generated by the manufacturing process. In manufacturing procedures that involve complete melting and solidification, Ti64 may experience the liquid→β→α+β or liquid→β→α'. The α+β dual phase exists only during a slow solidification process with a diffusional phase transformation. Rapid cooling via diffusionless transformation results in the creation of the α' martensite phase [1].

Selective Laser Melting, an powder bed AM process, is one of the most favored ways for producing Ti64 parts due to its superior performance compared to other techniques, good surface quality, and ability to work in argon atmosphere [1]. SLM is controlled by four basic parameters such as laser power, scanning speed, hatch space, and layer thickness [4]. Another powder bed AM process is electron beam melting (EBM). This procedure is carried out in a vacuum of around 10^{-4} mbar. It uses the same additive manufacturing steps as SLM. However, the temperature of the build chamber is higher (500-800°C) than in SLM technology. EBM technology is employed in the manufacturing of high-value-added metals with dimensionally small to medium volumes [5].

In EBM technology, electrons accelerated between 0.1 and 0.4 times the speed of light are used as an energy source. The tungsten filament in the electron gun generates these electrons [6].

The microstructure of Ti64 parts produced by AM methods such as SLM and EBM is much finer than the microstructures obtained by conventional manufacturing. While the microstructure of Ti64 parts produced by conventional production is uniform, the microstructure of the parts produced by additive manufacturing is needle form. The typical microstructure of additive manufactured Ti64 consists of columnar prior beta grains that grow epitaxially, across several layers. When cooling below the β transus temperature α phase starts to form, first at the β grain boundaries and then, depending on cooling rate, the α phase grows along the β grain boundaries or into the β grains in a platelet form followed by the formation of the Widmanstätten alfa plates. The Widmanstätten α can nucleate in packets of similarly arranged platelets called colonies or as basketweave structures. The extent of alpha phase at the prior β grain boundaries as well as the size and distribution of α laths inside the prior β grains depend on cooling rate. Little or no α phase formation can be seen at the grain boundaries of the prior β phase under rapid cooling conditions. Ratio (length/thickness) of individual α laths decreases with increasing cooling rate [7]. Regarding the cooling rate, the completeness of α′ martensite formation depends on specific cooling rate ranges. Cooling rates above 410 °C/s^{-1} will create a full α′ martensite morphology, while cooling rates between 410°C/s^{-1} and 20°C/s^{-1} will lead to a partial α′ morphology, and cooling rates below 20 °C/s^{-1} will not develop α′ structures [1].

II. PROCEDURES

A. Sample preparation

Commercial Ti64 alloy powders which is fabricated for AM by gas atomization. The Microstructure investigation was performed on Ti64 samples powder bed melting samples with a dimension of 10x10x20 mm was fabricated by SLM and EBM 3D printer, with energy density of 12.5, 25, and 37.5 (J/mm^3).

Hereafter, the EBMed Ti64 samples are EBM-1, EBM-2, and EBM-3 for EBM in order of 12.5, 25, and 37.5 (J/mm^3), while the SLM process parameters were design to have energy density of 20.8, 41.7, and 62.5 J/mm$^{3.}$ However, due to the expected 60% efficiency of laser process, it is design in this energy range to be comparable to EBM process. So, 60% of 20.8, 41.7, and 62.5 J/mm^3 is equal to 12.5, 25, and 37,5 J/mm^3.

B. Characterizations

The specimens for the optic microscope (OM) analysis were mechanically polished and then etched in a Kroll's reagent consisting of 2 vol. % HF, 6 vol. % HNO_3, and 92 vol. % H2O.

Microstructure investigations have been carried out by (OM) and scanning electron microscope (SEM). Archimedes methods have been applied to measure the relative density of the samples.

III.RESULTS AND DISCUSSION

In theory, AM techniques can generate full-density structures, but porosity occurs in the structure due to inappropriate process parameters and the powder generation process [3], [7], [12],[14]. There are three types of porosity: spherical gas pores, gas pores with filled molten powder, and irregularly shaped pores generated by lack of fusion.

Figure 1 shows optical microscope images of EBM-1, EBM-2, and EBM-3 samples after polishing at 10X magnification. It showed when the energy volume increases, the number and size of the pores decrease.

EBM technique, the energy volume depends on the applied current value. Also, much finer grains and much denser parts are produced with an increase in the current value. In parts produced with

EBM, the thermal history takes place in a more complex way. Because PBF is produced in layer by layer, a molten layer is formed on solidified layer. This causes the formation of different heat zones on the part.

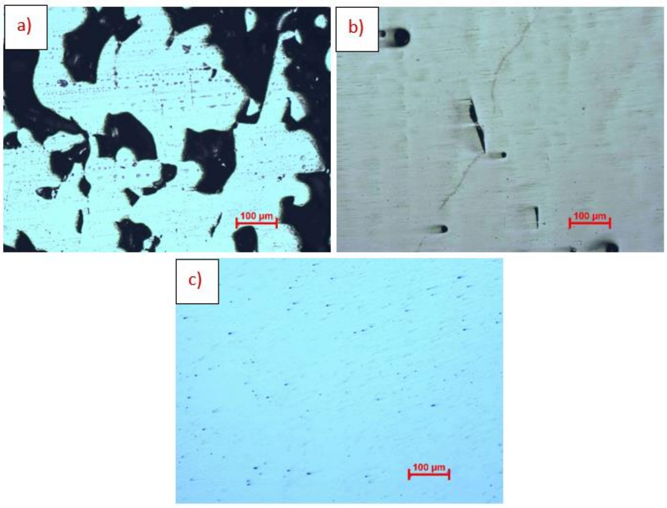

Figure 1: After polishing, optical microscope images at x10 magnification of A) EBM-1, B) EBM-2, and C) EBM-3 samples

The same is available for SLM-produced parts. Figure 2 shows optical microscope pictures of SLM-1, SLM-2, and SLM-3 samples after polishing at x10 magnification. Pores in the SLM-1 and SLM-2 are caused by improper process parameters and trapped gas. When compared to SLM-1 and SLM-2, SLM-3 had smaller gas holes. In SLM-3 did not show irregular gas pores. It showed that a combination of high laser power and low scanning speed would result in a denser part. SLM technique, the energy volume depends on the laser power and scan speed. Also, much denser parts are produced with an increase in the energy power. The combination of high scanning speed and low laser power in the SLM technique causes a faster cooling. Sample produced with SLM have the highest relative density. In the SLM technique, the best results were obtained from the sample using low scanning speed and high laser power (SLM-3).

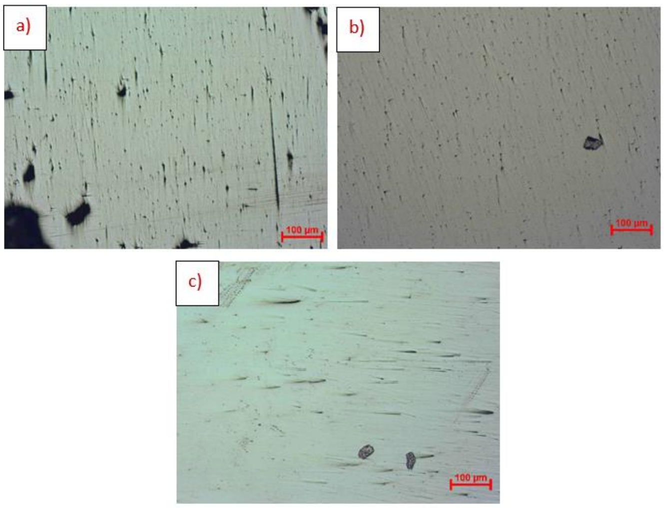

Figure 2: After polishing, optical microscope images at x10 magnification of A) SLM-1, B) SLM-2, and C) SLM-3 samples

In order to show the effect of the pores on the sample density, the relative densities of the samples were calculated as a percentage using the Archimedean technique. It is seen in Figure 3. In both techniques, denser parts can be produced by increasing the energy volume value. At the same energy volume values, parts produced with SLM have a much higher relative density than parts produced with EBM.

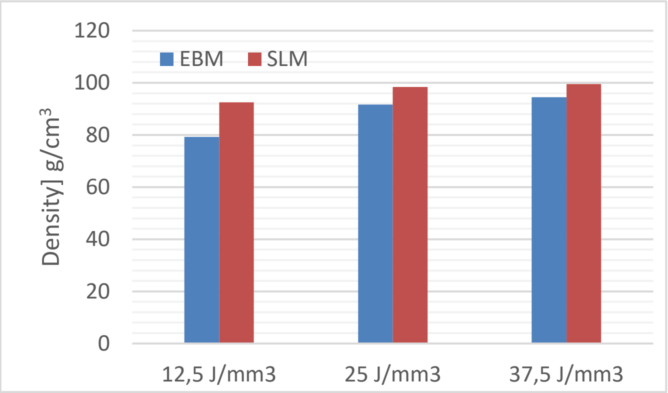

Figure 3: Measured density of the sample fabricated by EBM and SLM

The thermal history of Ti64 samples produced with EBM can be summarized in three stages. In the first stage, diffusionless transformation occurs due to high-speed cooling from the molten state from about 1900°C to the building chamber temperature of 650°C. For this reason, α' martensite structure is formed because of rapid cooling. Due to the cooling rate is faster than 410°C/sec for first stage. In the second stage, between 650-750°C, α' martensite turns into α+β phase as a result of slow cooling. In the third step, the build platform is slowly cooled from the chamber temperature to room temperature. Since this cooling rate is slower than 20 °C/sec, the α+β phase remains in the structure without any transformation at room temperature. These three cooling stages determine the microstructures obtained by the EBM process. [11].

The thermal history of the Ti64 part produced with the SLM technique during the production phase consists of 5 cycles. The first and second cycles are cooling above the liquidus temperature, the third cycle is the cooling between the solidus temperature and the β transformation temperature, the fourth cycle is the cooling between the β transformation temperature and the martensite initial temperature, and the fifth last cycle is the cooling below the martensitic initial temperature. Each thermal cycle affects the phase transformations in the microstructure of the part [1].

Figure 4 shows the images of the Ti64 sample produced with EBM and SLM, taken with an optical microscope at 100X magnifications. α platelets are more needle-like in the SLM technique, as a faster cooling occurs compared to the EBM. While there is a partial conversion to α grains at the grain boundaries of the prior β grain boundaries in the EBM technique, α phase formation is not seen at the grain boundaries in the SLM technique, the grain boundaries consist of the prior β phase. This situation is seen in figure 4.

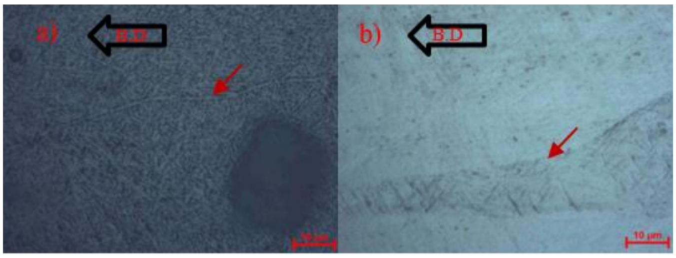

Figure 4: a) EBM, b) SLM OM pictures x100 magnifications

IV. CONCLUSIONS

1. The microstructure of as-built Ti-6Al-4V by EBM consist of columnar prior β grains delineated by wavy grain boundary α and transformed α/β structures with both colony and basket-wave morphology as well as numerous singular α platelets within the prior β grains.
2. The microstructure of as-built Ti-6Al-4V by SLM is dominated by columnar β grains and α' martensite laths because of high cooling rate.
3. Sample produced with EBM have the lowest relative density (EBM-1).
4. Sample produced with SLM have the highest relative density (SLM-3).

ACKNOWLEDGMENT

This study was funded by the Scientific and Technological Research Council of Turkey (TUBITAK) BIDEB 2209B Grant No: 1139B412100784

REFERENCES

[1] D. K. Do, "Microstructure characterizing and mechanical properties of selective laser melted ti-6al-4v alloys," University of Glasgow, 2021.

[2] S. Liu and Y. C. Shin, "Additive manufacturing of Ti6Al4V alloy: A review," *Mater. Des.*, vol. 164, p. 107552, 2019, doi: 10.1016/j.matdes.2018.107552.

[3] S. Temel, "Katm anlı İmalatla Üretilen Ti6Al4V Parçalarının Mekanik Özellikleri," pp. 27–37, 2017.

[4] L. Xiao, W. Song, M. Hu, and P. Li, "Materials Science & Engineering A Compressive properties and micro-structural characteristics of Ti – 6Al – 4V fabricated by electron beam melting and selective laser melting," *Mater. Sci. Eng. A*, vol. 764, no. March, p. 138204, 2019, doi: 10.1016/j.msea.2019.138204.

[5] P. Wang *et al.*, "Recent progress of additive manufactured Ti-6Al-4V by electron beam melting," *Solid Free. Fabr. 2016 Proc. 27th Annu. Int. Solid Free. Fabr. Symp. - An Addit. Manuf. Conf. SFF 2016*, pp. 691–704, 2016.

[6] H. Gong, K. Rafi, T. Starr, and B. Stucker, "The effects of processing parameters on defect regularity in Ti-6Al-4V parts fabricated by Selective Laser Melting and Electron Beam Melting," *24th Int. SFF Symp. - An Addit. Manuf. Conf. SFF 2013*, no. August, pp. 424–439, 2013.

[7] M. Neikter, P. Åkerfeldt, R. Pederson, and M. L. Antti, "Microstructure characterisation of Ti-6Al-4V from different additive manufacturing processes," *IOP Conf. Ser. Mater. Sci. Eng.*, vol. 258, no. 1, 2017, doi: 10.1088/1757-899X/258/1/012007.

[8] A. Safdar, *A Study on Electron Beam Melted Ti-6Al-4V Adnan Safdar Division of Solid Mechanics Department of Construction Sciences*. 2012.

[9] M. K. Kolamroudi, M. Asmael, M. Ilkan, and N. Kordani, "Developments on Electron Beam Melting (EBM) of Ti – 6Al – 4V :," *Trans. Indian Inst. Met.*, vol. 74, no. 4, pp. 783–790, 2021, doi: 10.1007/s12666-021-02230-9.

[10] Y. Kok, X. Tan, S. B. Tor, and C. K. Chua, "Fabrication and microstructural characterisation of additive manufactured Ti-6Al-4V parts by electron beam melting: This paper reports that the microstructure and micro-hardness of an EMB part is thickness dependent," *Virtual Phys. Prototyp.*, vol. 10, no. 1, pp. 13–21, 2015, doi: 10.1080/17452759.2015.1008643.

[11] H. Galarraga, R. J. Warren, D. A. Lados, R. R. Dehoff, M. M. Kirka, and P. Nandwana, "Effects of heat treatments on microstructure and properties of Ti-6Al-4V ELI alloy fabricated by electron beam melting (EBM)," *Mater. Sci. Eng. A*, vol. 685, pp. 417–428, 2017, doi: 10.1016/j.msea.2017.01.019.

A Review for Weight Reduction in Automobiles: Lightening the Center Floor Panel

[1]Ali Karafakıoğlu, [2]Fevzi Bedir, [1]Mustafa Kocaman, [3]Burak Dikici, [1]Sevil İnan Öz

[1]Ho-Won Otomotiv Sanayi Tic. A.Ş. 41010 Kartepe/Kocaeli-Turkiye
arge@howon.com.tr
[2]Gebze Technical University, Dept of Mechanical Eng. 41400 Gebze/Kocaeli-Turkiye
fevzibedir@gtu.edu.tr
[3]Atatürk University, Dept. Metallurgy and Materials Eng. 25240 Erzurum-Turkiye
burakdikici@atauni.edu.tr

***Abstract*—Aluminum alloys have a crucial role in replacing auto parts in the near future. Its material properties give it some advantages and pioneer the way for new applications in the automotive industry. Besides the most important of these light materials is their use in automobile body applications. Car bodies consist of nearly 25% of the total weight of a car. In this study, the center floor panel, which is a dash panel connected to the front part and a rear panel to the rear part, are installed on the center floor driver's seat and passenger seat. While driving a vehicle, the center floor panel protects both passengers by absorbing shock in the event of a side collision and supports vehicle rigidity, and prevents the noise and outdoor foreign substances from entering the vehicle.**

***Keywords*—Weight Reduction, Center Floor Panel, Automotive industry, Aluminum alloy, manufacturing.**

I. INTRODUCTION

In the transportation sector, it is very important to improve fuel efficiency to reduce environmental pollution. Lightening studies in vehicles is an important technology [1]. There has been a trend towards electric vehicles to reduce fuel consumption and exhaust emissions. Many engineers are researching how to increase the battery capacity to increase vehicle mileage. However, the electric vehicle has an extraordinary problem in use, because the car is very heavy due to the battery weight and body structure and therefore the electric vehicle mileage is reduced. Unfortunately, how to reduce weight is a topic that has been studied for a long time [2]-[5].

Car bodies contribute approximately 25% of the total weight and a suitable solution is required to break this cycle. Light metals and composite hybrid structures are seen as a promising opportunity for the stable lightening of the Body in White. The increasing use of metals such as aluminum and magnesium in the automotive industry shows that they still exist. Estimates come from aluminum's contribution to total vehicle weight from 6% to over 10% after turning [6]. This study aims to develop a mixed-use center floor module for heterogeneous materials for SUVs, which has a weight reduction of more than 25% and equivalent rigidity compared to existing parts.

II. DESIGN PROPOSAL

The center floor is a dash panel connected to the front part and a rear panel to the rear part, as shown in Fig. 1. The floor module is connected. The driver's seat and passenger seat are installed on the center floor, and when driving a vehicle, it protects passengers by absorbing shock in the event of a side collision and supports vehicle rigidity.

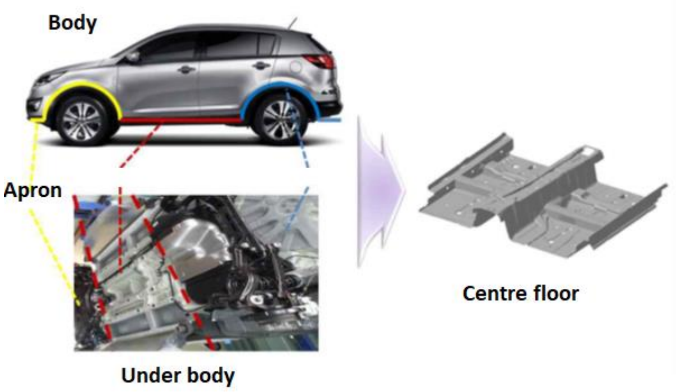

Fig. 1 Center Floor Module

Existing material center floor modules are center floor panels, center floor reinforcements, and side sill inners. The center floor panel has a tunnel part that protrudes in an inverted U shape so that the exhaust system can pass to the center. The seat cross member is provided on both sides of the tunnel part of the center floor panel to allow the vehicle seat to be mounted and to reduce the impact force generated in the side collision. The reinforcement is reinforced on the upper part of the tunnel part of the center floor panel to improve the vehicle front collision characteristics. The lower part of the center floor panel is provided with the tunnel part of the panel and the center floor side members at the left and right ends of the center floor panel. To secure the structure.

After molding, it is assembled by joining parts with multiple spot welding. Recently, as the weight reduction of body parts is accelerating due to tightening regulations on the automobile environment and fuel economy, the development and sales of SUVs that have increased fuel efficiency and convenience are increasing. Lightweight materials that are currently being researched in place of the existing mild steel materials include high-strength/ultrahigh-strength steel materials, non-ferrous metal materials such as Al/Mg, and polymer materials.

The energy consumption of a vehicle during use is the sum of the fuel consumption for travel and the energy spent for gasoline production. According to statistics, the annual mileage is 10,057 km and the average usage is 9.12 years, resulting in total mileage of 91,720 km. As shown in Fig. 2, it was calculated a relationship between vehicle weight and actual fuel efficiency using automobile catalogs and studies.

Here;
$Y=1/(6E\text{-}5*X+0.0174)$
X: Vehicle weight (kg),
Y: Real fuel efficiency (km/l)

A steel vehicle weighing 1,380 kg had a fuel efficiency of 9.98 km/l and a CFRP vehicle weighing 881 kg had a fuel efficiency of 14.23 km/l. Lifetime gasoline consumption is 9,190 liters and 6,446 liters, respectively [1].

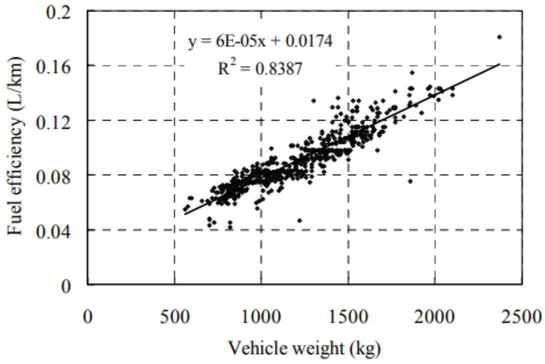

Fig. 2 Relation between vehicle weight and real fuel efficiency

In recent years, research on the application of multi-materials to use in the right place according to the properties required for parts by taking advantage of lightweight materials has been conducted. In addition, it is necessary to study various production technologies such as forming and joining parts to solve the difficulty formation and the difficulty bonding, which are common characteristics of lightweight materials by mixing different materials. The center floor module, which is currently being developed in domestic and overseas markets, is expanding the application of high tensile steel with the high tensile strength to increase strength, rigidity, and lightweight. However, there is a limit to breakthrough weight reduction, as shown in Fig 3.

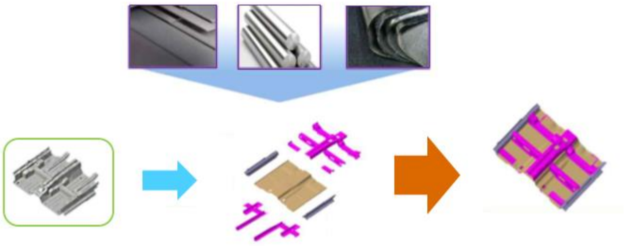

Fig. 3 Schematic diagram of the development center floor module

This project aims to develop a mixed-use center floor module for heterogeneous materials for SUVs, which has a weight reduction of more than 25% and equivalent rigidity compared to existing parts. The development center floor module consists of an integrated center floor panel with CFRP made of UD / Fabric material and high-strength steel applied parts of 7xxx series aluminum / 590 ~ 900MPa class. The goal is to develop a center floor module that has less than the amount of deflection and torsion of the existing center floor module, as shown in Fig. 4.

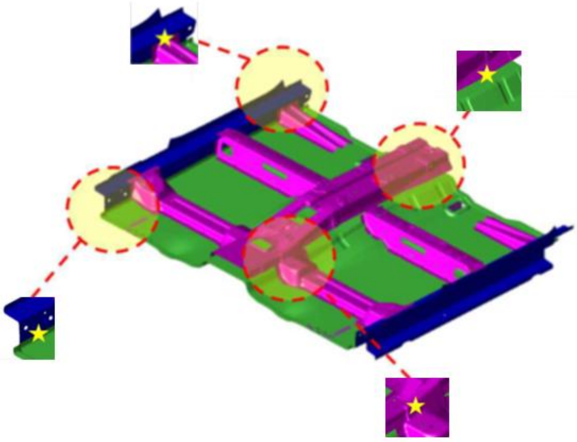

Fig. 4 Development material and bonding method

Key technologies in design are as follows;

- Structural Design Analysis of Mixed Material Center Floor Module,
- Development of part molding technology for different material types,
- Development of high strength bonding technology between different materials (CFRP + Al, CFRP + Steel, Steel + Al),

To secure structural optimization design analysis technology by mixing various lightweight materials in the center floor module;

- As it uses various lightweight materials, it is necessary to build basic property data for structural design and analysis, because each material has different physical properties and different deformation behavior, it is necessary to optimize structural shape design and precise analysis technology by using different materials to secure optimal performance.

To develop molding technology for center floor module components applied to lightweight materials;

- To secure CFRP high-efficiency part molding technology.
- Aluminum parts are to be molded by applying the extrusion method. Expected to have Extrusion has the advantage of speeding up the production of products by continuously producing some types of parts such as bumper back beams
- High-strength steel parts are manufactured by press molding, and they want to realize precise parts molding while minimizing spring back, as shown in Fig. 5.

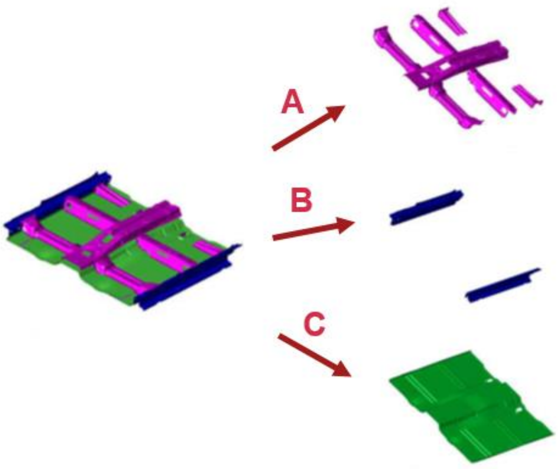

Fig. 5 Example of development of molding technology for parts with lightweight materials

To develop high strength dissimilar material joining technology by mixing various lightweight materials;

- CFRP / aluminum / tensile steel is different from each other in melting point, solidification point, structure, etc. Applying adhesive application technology that can have excellent bonding strength between metal and nonmetal and riveting which is a kind of mechanical bonding, we developed high strength bonding technology for Al + high tensile steel, Al + CFRP, CFRP + high tensile steel materials.

This ultra-light center floor module technology for SUVs through the use of heterogeneous materials is a leading technology with insufficient development of related technologies in Turkey.

III. CONCLUSIONS

Weight reduction of body parts is very important for CO_2 emission regulations on the automobile industry and fuel economy. Lightweight materials that are currently being researched in place of the existing mild steel materials include high-strength/ultrahigh-strength steel materials, non-ferrous metal materials such as Al/Mg, and polymer materials. The energy consumption of a vehicle during use is the sum of the fuel consumption for travel and the energy spent for gasoline production. The center floor module, which is currently being developed in domestic and overseas markets, is expanding the application of high tensile steel with the high tensile strength to increase strength, rigidity, and lightweight. The center floor module for heterogeneous materials has a weight reduction of more than 25% and equivalent rigidity compared to existing parts. The development center floor module consists of an integrated center floor panel with CFRP made of UD / Fabric material and high-strength steel applied parts of 7xxx series aluminum/590 ~ 900MPa class. The goal is to develop a center floor module that has the same mechanical strength with a new design and less weight to compare with the existing center floor module.

REFERENCES

[1] Tetsuya Suzuki, Jun Takahashi, LCA of lightweight vehicles by using cfrp for mass-produced vehicles, Conference: 15th International Conference on Composite Materials (ICCM-15) At: South Africa June 2005.

[2] Sun Wenlong , Chen Xiaokai , Wang Lu, Analysis of Energy Saving and Emission Reduction of Vehicles Using Light Weight Materials, Energy Procedia 88 (2016) 889 – 893.

[3] Yasuhiro Kan, Ryusuke Shida, Jun Takahashi and Kiyoshi Uzawa, Energy saving effect of light-weight electric vehicle using cfrp on transportation sector, 10th Japan International SAMPE Symposium & Exhibition (JISSE-10) November 27-30, 2007, Tokyo Big Sight, Tokyo, Japan.

[4] Savkin Alexey Nikolaevich , Andronik Artem Valerievich , Gorunov Andrey Igorevich, Sedov Alexander Alexandrovich , Sukhanov Mikhail Alexandrovich, Advanced materials of automobile bodies in volume production, European Transport \ Trasporti Europei (2014) Issue 56, Paper n° 10, ISSN 1825-3997.

[5] Daniel Carle, Gordon Blount, The suitability of aluminium as an alternative material for car bodies, Materials and Design 20 (1999) 267-272.

[6] Michio Takita and Akinori Maruta, Trend toward Weight Reduction of Automobile Body in Japan, Seoul 2000 FISITA World Automotive Congress F2000G339 June 12-15, 2000, Seoul, Korea.

Investigation of nano hydroxyapatite composite doped with nano zinc oxide in terms of bioactivity and mechanical properties

Busranur Yildirim*, Nermin Demirkol+

**Faculty of Technology, Biomedical Engineering Department, Kocaeli University,Turkey*
busranur.iyildiz@gmail.com

+ Faculty of Fine Arts, Ceramic Department, Kocaeli University,Turkey
nermin.demirkol@kocaeli.edu.tr

Though most of the cases the purpose of using nano-biomaterials is to reinforce and improve the structural stability. Hydroxyapatite (HA) is commonly used as an efficient biomaterial owing to its well-documented ability for defective bone treatment. This work was aiming to produce novel hot pressed biocomposite material based on nano hydroxyapatite and nano zinc oxide. 90 wt.% nano hydroxyapatite and 10 wt. % nano zinc oxide mechanically alloyed for 4 hours. XRD and particle size analyses were carried out to determine mixture properties. Then the mixture was subjected to sintering by hot pressing. Sintering was carried out at 760ºC for 30 minutes. Mean density was obtained as 2,94 g/cm^3. The phase analyses of the samples obtained after sintering were determined by XRD and their microstructures were examined with SEM. Strength and hardness values were determined by mechanical tests. The bioactivity property was determined by in vitro bioactivity test. The results were compared with the literature.

Key Words: Nano, hydroxyapatite, zinc oxide, composite, bioactivity, mechanical properties.

The next presentation was made as a poster.

2nd International Symposium on
Light Alloys and
Composite Materials

OPTICAL PROPERTIES OF COMPOSITE WINDSHIELD TRANSPARENCIES

Damla KÖROĞLU, Rıfat YAPICI, Özlem EKER
damla@volo.com.tr, rifat@volo.com.tr, ozlem@volo.com.tr

ABSTRACT

In this study, lamination of different type of helicopter transparencies which are polycarbonate (PC) and acrylic (PMMA) with thermoplastic polyurethane (TPU) and their individuals are inspected in terms of light transmittance and mechanical properties. Light transmittance values of transparencies made of PC, PMMA and their combination have been measured for different wavelengths in wide spectrum. In addition to that, important aviation mechanical properties which are impact toughness, crack propagation resistance and abrasion resistance of PC, PMMA and their combination are compared.

Keywords: Acrylic, Polycarbonate, Thermoplastic Polyurethane, Composite, Lamination

1. INTRODUCTION

PC and PMMA materials are used for manufacturing of windshields, windows and canopies in today's aviation industry. Energy toughness and crack propagation resistance properties of PC materials are significantly more considerable than PMMA materials. On the other hand; when light transmittance and abrasion resistance properties are taken into consideration, PMMA materials is better choice than PC materials. Acrylic and polycarbonate materials have different superior properties compared to each other. Therefore, composite material which is combination of these two materials with aid of TPU interlayer material fulfils the requirement helicopter transparencies.

2. EXPERIMENTAL PROCEDURES

First of all, 50mm x 50mm samples are prepared from PC and PMMA materials which are identical in terms of thickness, 3mm. Afterwards, light transmittance values are measured between 250nm and 850nm wavelengths for each sample according to the ASTM D1003 standard. . This measurement is performed with PerkinElmer Lambda 850 spectrophotometer device and taken data are processed with a suitable software. For mechanical properties of these materials are taken and inspected from *Helicopter Transparent Enclosures – Volume I – Design Handbook – Bruce F. Kay – January 1979.*

3. EXPERIMENTAL RESULTS AND DISCUSSION

Light transmittance measurement of clear polycarbonate material is presented in the following figure.

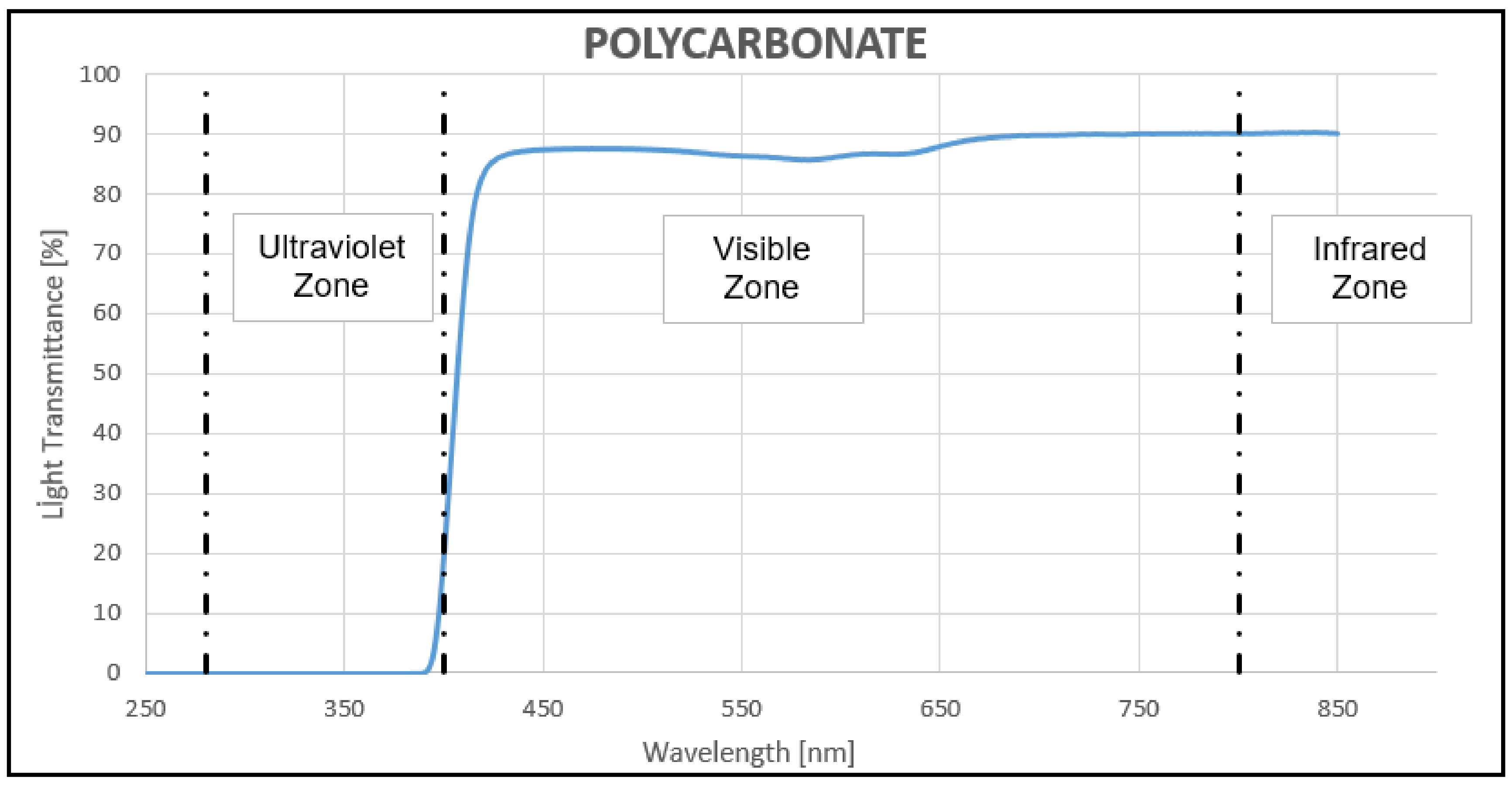

Light transmittance measurement of clear acrylic material is presented in the following figure.

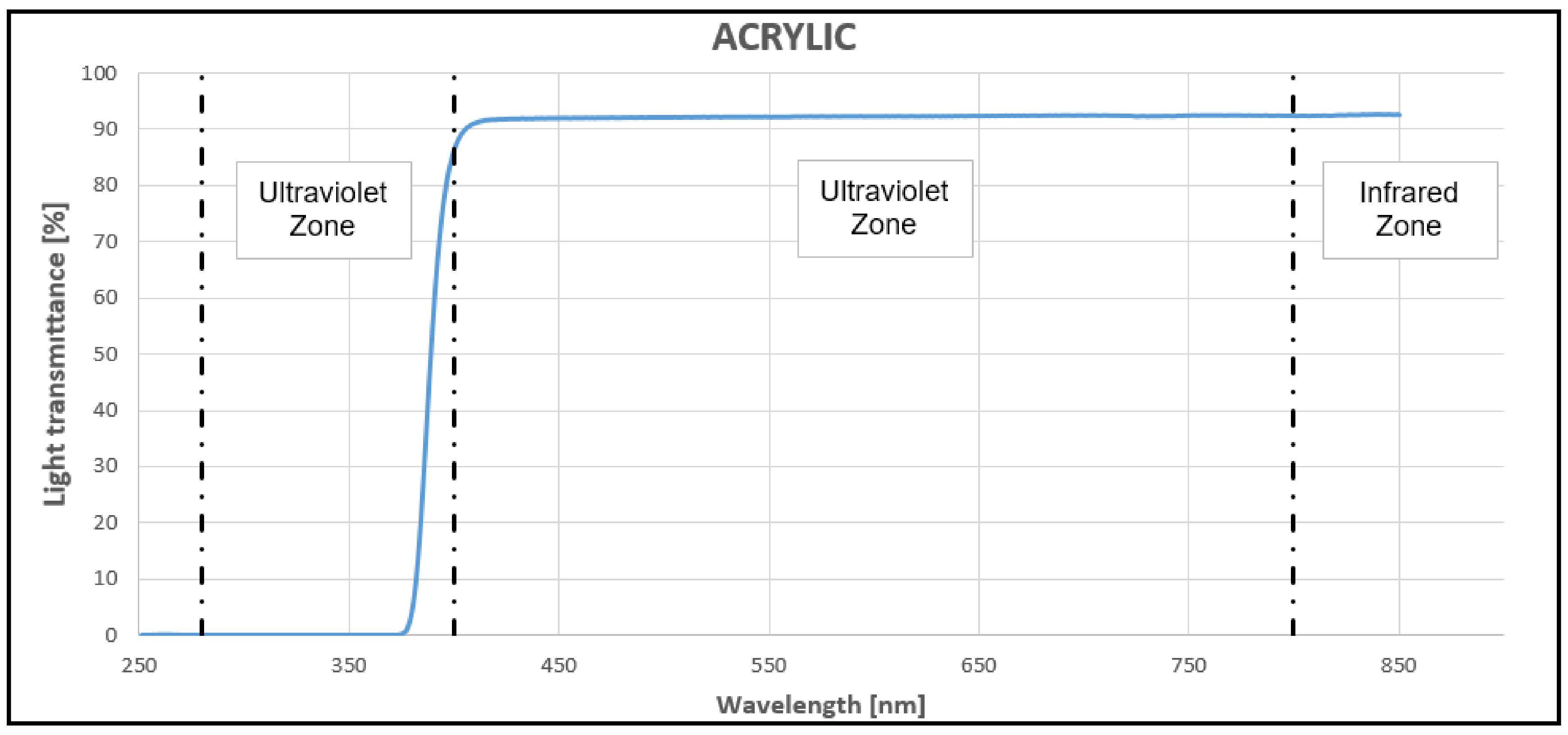

Light transmittance measurement of clear PMMA and clear PC composite material is presented in the following figure.

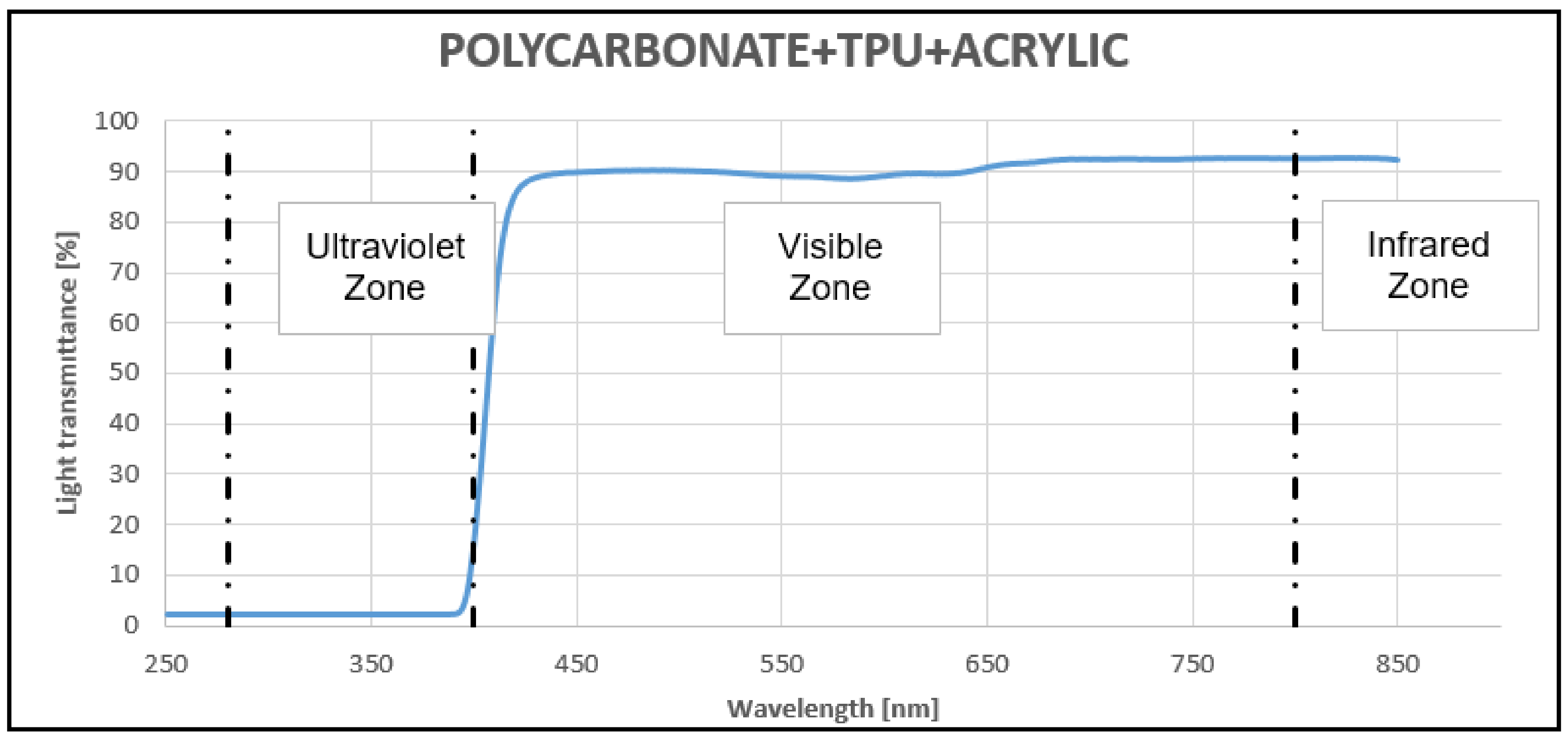

Comparison of these three is presented in the following figure.

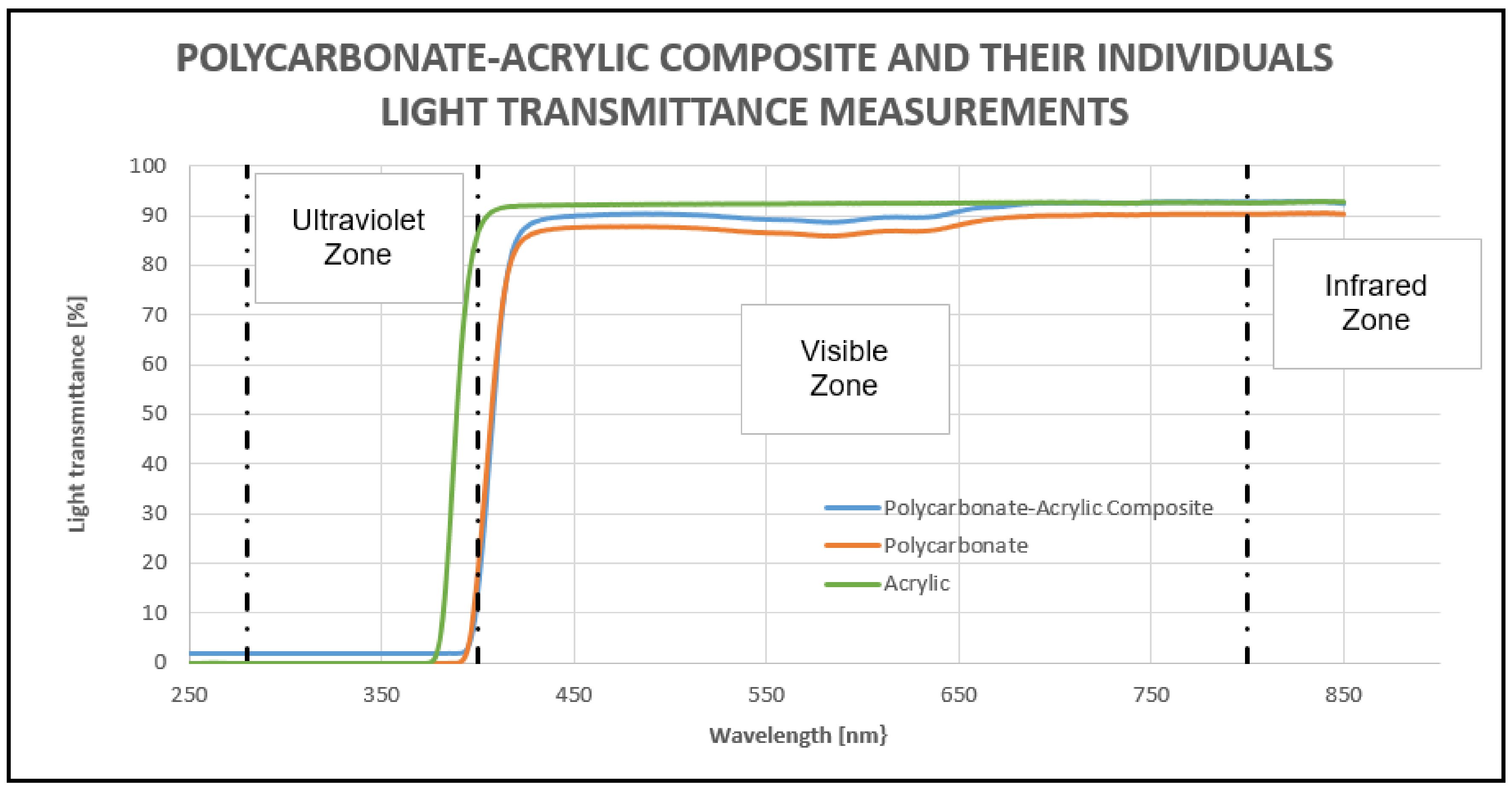

4. CONCLUSION

PC and PMMA materials are widely used in the aviation industry as aircraft transparencies because of their optical and mechanical properties. Design parameters of these are selected according to aircraft requirements. Although optical properties of composite helicopter transparencies are lower than monolayer PMMA material, composite helicopter transparencies are preferred nearly all helicopter windshields because of windshields violent requirements. Generally, these requirements are anti-icing and de-fogging function, bird strike compatibility, in other words high impact toughness, anti-spall and light transmittance value higher than 65% in the visible region.

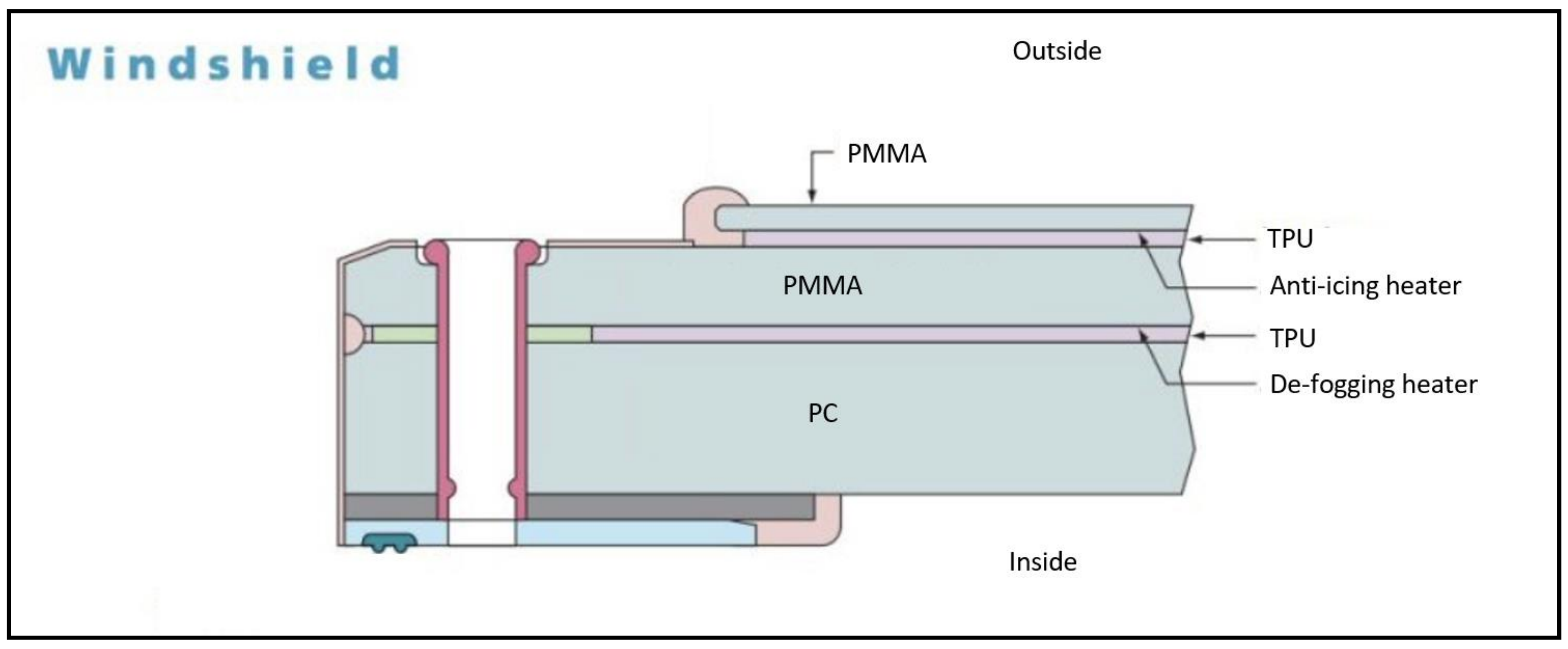

Anti-icing and de-fogging functions of transparencies can only be achieved by conductive coating or resistance wires. These heater materials must not be exposed to air. In order to achieve that composite transparencies are used and these heater materials are applied between PC and PMMA plies by the aid of TPU.

General configuration for a front windshield of a helicopter is PC+TPU+PMMA. PC material is in the inside of the helicopter. PC material is a ductile and PMMA material is a brittle material. Laminating PMMA with PC by TPU increases the anti-spall function of the composite due to the ductility of PC and TPU when a bird strike case occurs.

REFERENCES

[1] M. Turan, R. Yapıcı and Ö. Eker, "Solar Radiation Effect of Tinted and Clear Polycarbonate Transparencies Inside the Cockpit", ULIBTK'21 Uluslararası Katılımlı 23. Isı Bilimi ve Tekniği Kongresi, Gaziantep,September 2021

[2] *R. E. Moore* , "Method of Making Acrylic-Policarbonate Laminate", U.S. Patent 3681167, July 13,1970.

[3] A. Rühl, On the Time and Temperature Dependent Behaviour of Laminated Amorphous Polymers Subjected to Low Velocity Impact,Band 47, Institute of Mechanics and Materials, Germany:Springer-Band 47,2017

[4] D. L. Voss, W. A. Miller, R. D. Hermasen, "Transparent Formable Polyurethane Polycarbonate Lamination", U.S. 4045269,Aug. 1977

[5] E. K. Welhart, D.L. Voss, J.F. Harrell, "Transparent Laminate", U.S. Patent 3810815, May 14,1974

[6] *C.A. Harper,* "Handbook of Plastics, Elastomers and Composites", University of Massachusetts Lowell, Plastics Engineering Department, Massachusetts

INVESTIGATION ON THE EFFECT OF LEATHER SAWDUST ON MECHANICAL PROPERTIES OF EPOXY MATRIX COMPOSITES

Abdullah DAĞDEVİREN, Muhammet Mevlüt KARACA, Yasin AKGÜL

Iron and Steel Institute, Karabük University, TURKEY

This study aims to investigate the effect of different weight fractions (1%, 3%, and 5%) of Leather Sawdust (LS) on the mechanical properties of epoxy matrix composites. The samples were fabricated using the hand lay-up method. To investigate the mechanical properties of pure epoxy and composites (Epoxy-LS), tensile, 3-point bending, and impact tests were conducted. The result of this study reveals that the flexural strength and yield strength of epoxy-based composite with 1 wt. % LS were higher than the pure epoxy nearly by 30% and 50%, respectively. However, When the reinforcement ratio was increased from 1% to 5%, the mentioned properties decreased below the values of pure epoxy. Also, the tensile and impact absorbing properties of the epoxy decreased with the LS reinforcement. Therefore, it can be said that using Leather Sawdust at lower ratios (up to 1%) is effective for epoxy matrix composites.

Keywords: Leather Sawdust, Polymer Composites , Mechanical Properties

Influence of Tool Travel Speed on The Mechanical Characterization of Friction Stir Welded 6061 T6 Sheets

Emir Tabanlıoğlu*, Emre Yiğitoğlu*, Mehtap Hıdıroğlu*

**Coşkunöz Kalıp Makina Sanayi ve Ticaret Anonim Şirketi, R&D Center, Bursa, Turkey*

etabanlıoglu@coskunoz.com.tr

eyigitoglu@coskunoz.com.tr , mhidiroglu@coskunoz.com.tr

***Abstract*— In recent years, friction stir welding (FSW) demand has become a viable manufacturing technology for the structural assembly of plate materials due to its light weight and thermal properties in many industrial applications as automotive sector. In this study, the effect of tool travel rate on the welding quality of 4mm thick friction stir welded 6061 series aluminium sheets was investigated. The effect of the test matrix formed with different tool travel rates on the mechanical performance and interface properties of the joint was evaluated with the help of macro/micro interface optic examinations and tensile test results. A friction welding machine with pressure control function was preferred in order to prevent the effect of plate thickness changes caused by extruded plate production and fixture/equipment deformation during the welding process. The effects of 3 different travel speed parameter values on the tensile test results investigated.**

***Keywords*— Fricton stir welding, 6061 T6, Mechanical characterization.**

I. INTRODUCTION

Friction stir welding (FSW) is a solid-state joining process. The advantage of this method is joining of the metals is achieved without melting [1]-[4]. Among the benefits of this method are no weld solidification effects as porosity, shrinkage, hot cracking, weld fume, reducing distortion with low heat input, low energy consumption and have fine grain microstructure.

The advantages of solid-state FSW processes also include better mechanical properties, low residual stress and deformation, weight, and reduced defects [5]. In particular, FSW has been widely used in recent years for joining non-ferrous metals foremost Al. FSW is also preferred because haven't been affect the heat transfer in the battery housing components and cooling plates of electric vehicles as much as in the fusion welding zones.

Currently, the FSW study has mainly focused on joining Al alloy plate, which has the greatest demand in various industries compared to conventional welding processes [6].

In this study, T6 heat treated Al 6061 material was welded by friction stir welding method and the effects of welding travel speed parameters on the mechanical properties of the joint were investigated.

II. MATERIAL AND METHOD

The composition of the chemical alloy Al6061-T6 can be seen in table 1. Al 6061-T6 plate with dimensions of 300mm x 300mm x 4mm. Welding parameters are shown in Table 2.

TABLE I
CHEMICAL COMPOSITION OF 6061-T6 ALUMINIUM ALLOY.

% (wt)	**Al**	**Cr**	**Cu**	**Fe**	**Ga**	**Mg**	**Mn**	**Si**
AA-6061-T6	97.8	0.19	0.24	0.44	0.015	0.92	0.05	0.56

TABLE 2
WELDING PARAMETERS USED IN THE STUDY.

SAMPLE	**Rotation Speed (rpm)**	**Weld Speed (mm/min)**	**Force (kN)**	**Tilt angle (o)**
N1	2000	400	8	3
N2		600		
N3		800		

Fig. 1 FSW tool used in the study.

The plates were joined with a butt joint configuration with the tool seen Fig.1. The rotating pin (pin Ø = 5 mm) was y pushed into the Al-6061-T6 sheets until the pin tip entered (tool offset) 0.1 mm into the plates. The shoulder diameter of the tool used was12 mm. A friction welding machine with pressure control function was preferred in order to prevent the effect of plate thickness changes and fixture/equipment deformation during the welding process. Welded samples were taken from the FSW machine manufactured by Bejing FSW Technology Co., Ltd, model LM-BL20-2D.

III. Results and Discussion

A. *Macro and Microstructures analysis and results*

Macro images of the weld seams are given in Figure 2.

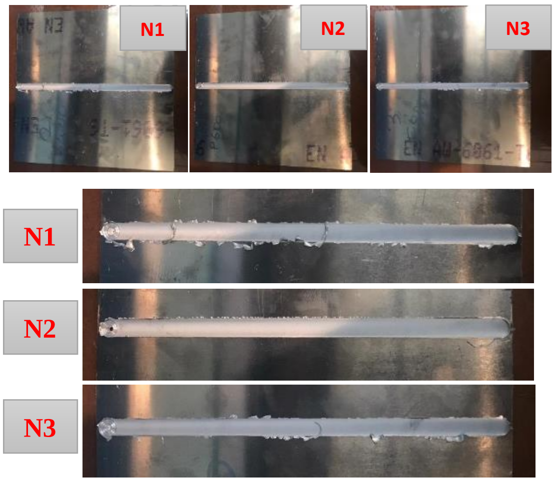

Fig. 2 Macro view of welded plates.

Welded samples were first visually inspected within the scope of the following 4 items.

1. Whether or not any macro-scale surface defects are encountered in the weld seams
2. Whether burrs and corrugations are formed on the retraction side of the weld seams in the produced welded plates.
3. Whether or not there is a tunnel defect in the root parts.
4. Whether or not there is an open crack on the surface.

When the samples seen in Figure 2 were visually examined within the scope of these 4 items, no macro weld defects were found.

Specimens were mechanically polished first with 600, 800, 1200 grit and 2500 grit SiC paper and then with 3 mm and 1 mm diamond paste. The final polishing of these specimens was accomplished using colloidal silica. After polishing, specimens were etched in a nitric Keller’s solution (150 ml H_2O, 3 ml HNO_3, 6 ml HF) at 273 K. After these treatments, they were prepared for optical microscopic observation. Sample surfaces were examined with a Nikon Epiphot 200 Inverted model optical microscope and macro-micro images were taken. The macro section images taken from the samples of all welded plates (produced with 3 different travel speed parameters) are given in Figure 3. A typical optical cross-sections have seen for all samples with four weld zone as the stir zone (SZ), thermo mechanically affected zone (TMAZ), heat affected zone (HAZ) and base material (BM).

Figure 4 shows the base metal microstructure. In Figure 5, the weld metal microstructures of samples N1, N2 and N3 can be seen.

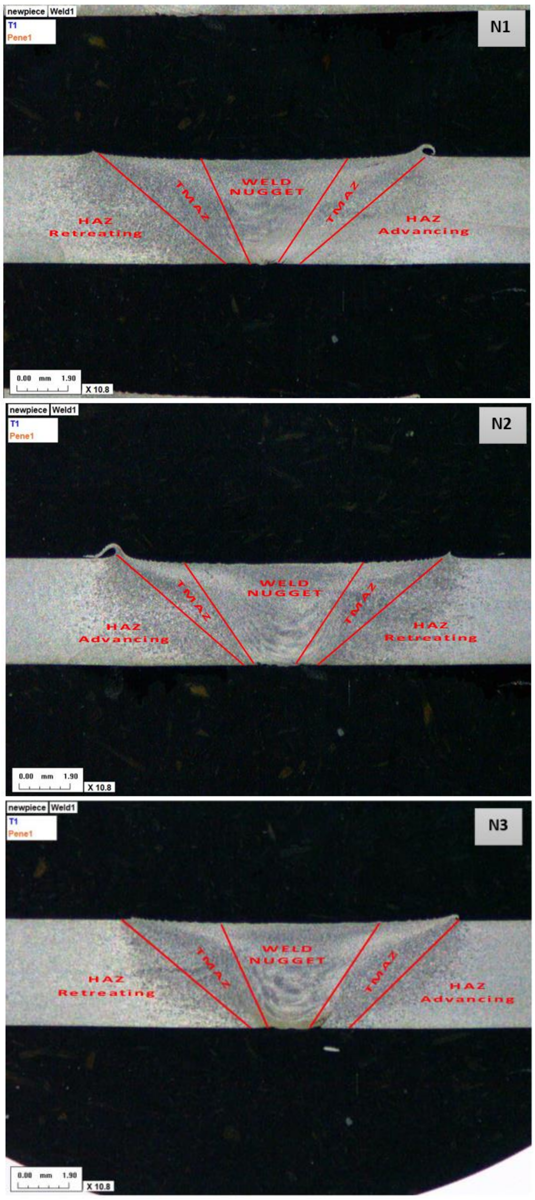

Fig. 3 Macro view section of joints.

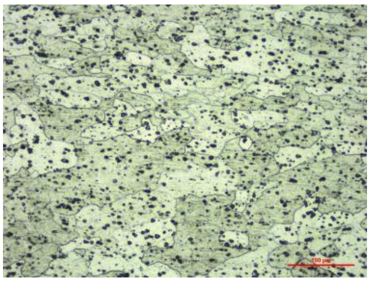

Fig. 4 Microstructure of base metal.

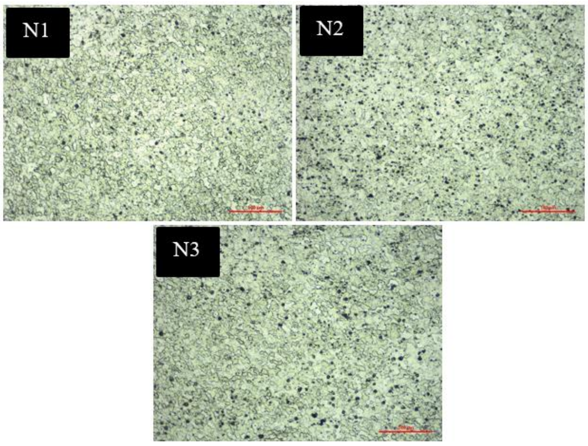

Fig. 5 Microstructure of weld metals.

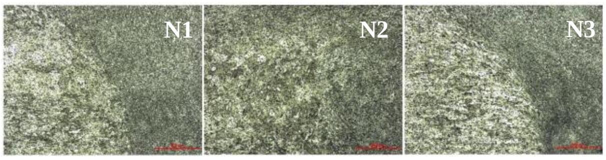

Fig. 6 Microstructure of weld metals.

Fig. 6 shows that grain refining took place in the recrystallized region of AA6061-T6 plates. However, grain refining shows that when a higher travel speed (800 mm/min) is used, a finer grained microstructure is formed due to lower heat input.

B. *Hardness Test and Results*

HV5 hardness measurements were carried out with the QNESS brand Q01450812 model hardness device. The hardness traces taken in Fig.7 are numbered. Hardness measurement results of HAZ, SZ and BM are given in Table 3.

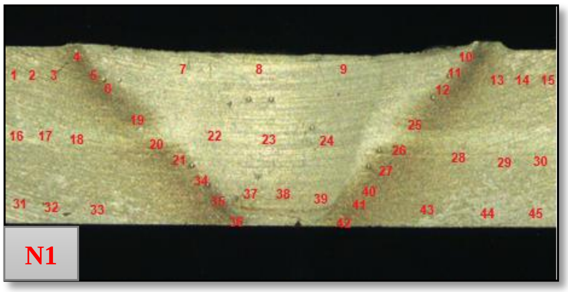

Fig. 7 Hardness test specimen "N1".

TABLE III
HARDNESS TEST RESULTS

	HAZ	Stir Zone (Weld Nugget)	Base Metal
N1	60,8	71,4	105
N2	63,4	73,2	102,8
N3	67,1	76,6	103,7

C. *Tensile Test and Results*

The test results of friction stir welded tensile specimens are shown in figure 7 and table IV. Average tensile strength values were calculated by cutting at least 3 test specimens from each welded plate. Tensile tests were performed on Instron brand 5989 L3619 model tensile device at 3Mpa/min tensile test speed in accordance with TS EN ISO 6892-1 standard.

TABLE IV
CHEMICAL COMPOSITION OF 6061-T6 ALUMINIUM ALLOY.

Sample Code	Maximum Load (kN)	Tensile stress at maximum Load (Mpa)	Tensile stress at yield (offset 0.2%) (Mpa)	Tensile strain at Break (standard) (%)	Average of Tensile stress at maximum Load (Mpa)
N1a	22,64	228,11	175,29	3,9	227,33
N1b	22,52	227,39	168,12	3,2	
N1c	22,71	226,49	181,91	3,08	
N2a	23,07	229,47	178,73	3,46	231,05
N2b	23,14	231,17	175,42	3,58	
N2c	23,03	232,53	188,84	3,34	
N3a	22,24	225,12	180,56	2,81	220,9
N3b	22,33	223,24	190,08	2,74	
N3c	21,3	214,29	187,04	2,27	

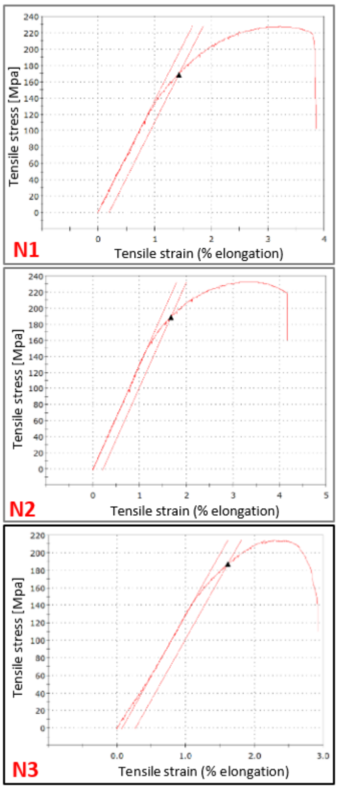

Fig. 7 One example of tensile test result graph of each parameters.

The average tensile strength of the sample N1 was measured as 227.33 Mpa, while the N2 numbered sample was 231.05 Mpa and N3 was 220.09 Mpa. As seen in Figure 8, fracture occurred in HAZ in all of the tensile test specimens. (Fracture occurred at the edge of the weld seam) The tensile results and the hardness measurements given in Figure Y are compatible with each other.

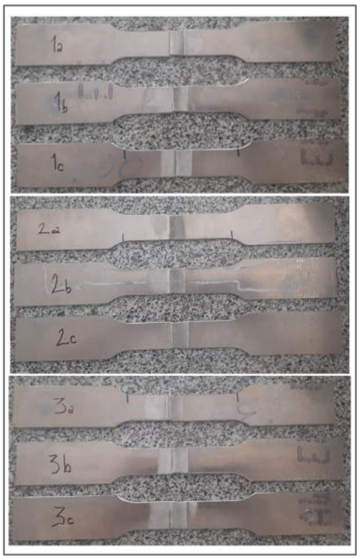

Fig. 8 The tensile test results show the fractures occurred in the HAZ region at the edge of the weld seam.

D. *Conclusions*

In this study, 6061-T6 sheets were successfully joined by the FSW method using the appropriate mixer tool. Welding faults were not found in all of the welded joints obtained.

Grain refining (fine grain structure formation) resulting from dynamic recrystallization was observed in the weld seam of all welded joints. Minimum hardness values in all welded specimens were observed in the HAZ with excessive aging.

The tensile strength of the base material is 292.26 Mpa. In N1, N2 and N3 welded samples, 78%, 80%, and 76% joint strength were obtained, respectively.

REFERENCES

[1] Flores OV, Kennedy C, Murr LE, Brown D, et al, "Microstructure issues in a friction-stir-welded aluminium alloy", *Scripta Mater*1998;38(5):703-708

[2] Murr LE, Liu G, et al, "A TEM study of precipitation and related microstructure in friction stir welded 6061 aluminium" , *J MaterSci* 1998;33(5):1243-1251

[3] Y.C.Chen, J.C. Feng, H.J. Liu, "Precipitate evolution in friction stir welding of 2219-T6 aluminium alloys", *MaterialsCharacterization* 2009; 60;476-481.

[4] Olivier Lorrian, Veronique Favier, et al, "Understanding the material flow path of friction stir welding process using unthreaded tools", *J Materials Process Technology* 2010;210;603-309

[5] J.-T. Yoo, J.-H. Yoon, K.-J. Min, and H.-S. Lee, "Effect of Friction Stir Welding Process Parameters on Mechanical Properties and Macro Structure of Al-Li Alloy", *Procedia Manufacturing*, vol. 2, pp. 325-330, 2015/01/01/ 2015.

[6] W. H. Jiang, R. Kovacevic, "Feasibility study of friction stir welding of 6061 – T6 aluminium alloy with AISI 1018 steel", *Proc. Isntn Mech. Engrs.Vol. 218 Part B: J. Engineering Manufacture*, 2004, pp. 1323 – 1331.

Experimental Investigations on the Mechanical Properties, Wear analysis and Microstructure of CuAlNi/B4C Composites Synthesized Using Powder Metallurgy Route

Berhan ŞAHİN[1], Tayfun ÇETİN[2],, M. Emre TURAN[1],Mustafa YAŞAR[1]

[1]University of Karabuk
Kılavuzlar Mah. Öte Karşı Üniversite Kampüsü Merkez Karabük
{ myasar@karabuk.edu.tr, memreturan@karabuk.edu.tr,
[2] University of Hakkari
Merzan Mah. Küçük Sanayi Sitesi Arkası 433. Sok. No: 51 Merkez/Hakkari
tayfuncetin@hakkari.edu.tr

This paper presents the investigation of synthesizing CuAlNi/ (B4C) composite by powder metallurgy route. Four various weight percentages of B4C (2.5, 5, 7.5 & 10) were reinforced with CuAlNi matrix (Cu-20 %Al-4 %Ni). The prepared powders were mixed with the TURBULA device for 1 hour. After the mixing process, the powders were pressed with a hot press. This compact was prepared at 850 °C 5 minutes waiting in a vacuum atmosphere using a PLC controlled hot press machine. The effect of B4C on hardness and wear resistance was analyzed. Optical microscope and scanning electron microscope (SEM-EDS) were used to determine the microstructures of the produced samples, X-ray diffraction method (XRD) and X-ray fluorescence (XRF) were used to determine the phases formed in the internal structures. From the microstructure results, it was determined that the B4C particles were homogeneously dispersed in the structure. Microhardness (HV5) was taken to determine the effect of B4C particles on hardness. The hardness values of the produced samples increased due to the increasing amount of B4C. In addition, as a result of the experiments, the highest hardness value was measured as 303.3 HV5 in the sample with 10% B4C added. When the wear results were examined, it was observed that the wear rate of the B4C reinforced composite was lower than that of the pure CuAlNi alloy.

Powder Metallurgy, Wear Resistance, B_4C, CuAlNi

Introduction

Composites have been used in a wide variety of applications as they have a number of necessary and variable properties such as high hardness, high-temperature flexibility, increased wear resistance, and low coefficient of thermal expansion. Metal matrix composite (MMC) is a composite type that has a metal matrix and reinforcement material. Matrix and reinforcement are combined in order to improve mechanical, thermal, and physical properties [1]. Various techniques are used for the production of composite depend upon reinforcement, such as compo casting [2], liquid phase infiltration [3], squeeze casting, and spray co-deposition [4]. The Shape Memory Effect, which is the phenomenon of some alloys changing their shape with the effect of temperature change and strain, and regaining their original shape by reverse transformation, is widely used in today's industry [5, 6]. Powder metallurgy (PM) is a suitable method for composite production because of the uniform distribution of reinforcement in the matrix, homogeneous matrix structure, and less adverse reaction between matrix and reinforcement at high temperature compared to casting [7, 8].

Composite materials with high mechanical properties are produced with Cu-Al-Ni alloys, which are successful in terms of lightness and strength. Cu-Al-Ni alloys are preferred as high engineering alloys for aerospace, automotive, and biomedical applications due to their excellent heat resistance, corrosion resistance, toughness, and strength [9-14]. In addition, these materials are used in industrial and medical applications as well as advanced applications, such as electronic devices, spacecraft, and many products that facilitate daily life, such as super-elastic eyeglass frames and telephone antennas [15,16]. However, when Cu-Al-Ni alloys are used in industry, their mechanical and wear properties are insufficient [17].

In this study, composite material with better mechanical and wear properties was produced by reinforcing B4C particles to Cu-Al-Ni alloy. This paper also analyses the effect of boron carbide, and the composites were also subjected to SEM and EDS analysis.

Materials and methods

Synthesis of B_4C reinforced Cu-Al-Ni composite

Copper-Aluminum-Nickel (Cu-84%, Al-12%, Ni-4%) powder was used for matrix material, and boron carbide (B_4C) was used for reinforcement. Four different weight percentages of boron carbide (2.5, 5, 7.5 & 10 wt.%) are reinforced with copper, aluminum, and nickel powders using the powder metallurgy. The required weight percentage of Cu-84 %Al-12 % Ni-4% and B_4C were mixed with a TURBULA brand mixer for 1 hour. In order to bulk up mixed powders, they were kept at 850 centigrade degrees for 5 minutes by using a graphite rectangular prism mold in PLC controlled and vacuum atmospheres hot press machine. Produced samples and hot press machine are shown in Figure 1a and Figure 1b.

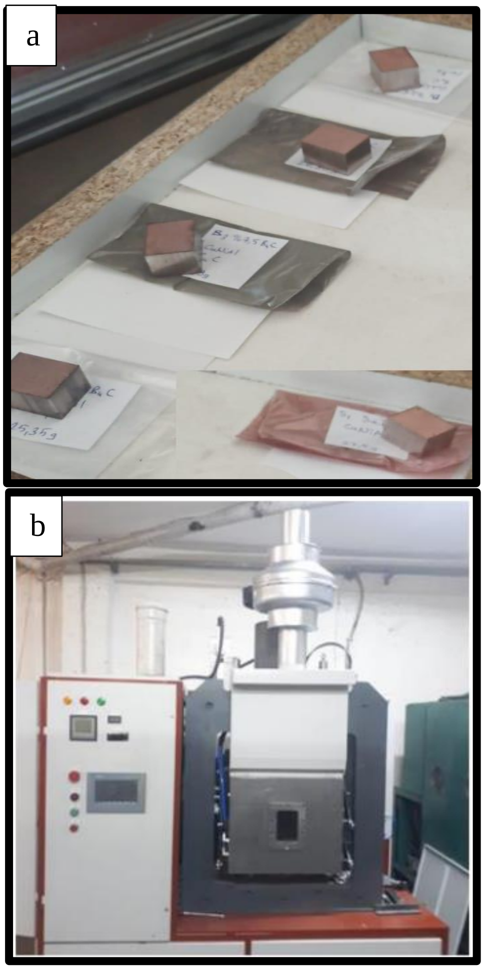

Fig. 1a. Produced Samples and Figure 1b. Hot Press Machine.

Results and Discussions

SEM Analysis of The Produced Composite

Figure 2 shows the SEM analysis result and macro image of the pure CuAlNi alloy sample. Figure 3-6 are show the SEM analysis results and macro images of weight percentages of B_4C 2.5, 5, 7.5, and 10, respectively. Copper, aluminum, nickel and B4C powders of 325 mesh size were used to synthesize composites. The purity values of powders; Cu and Al = %99.99, Ni and B4C=%99.95.

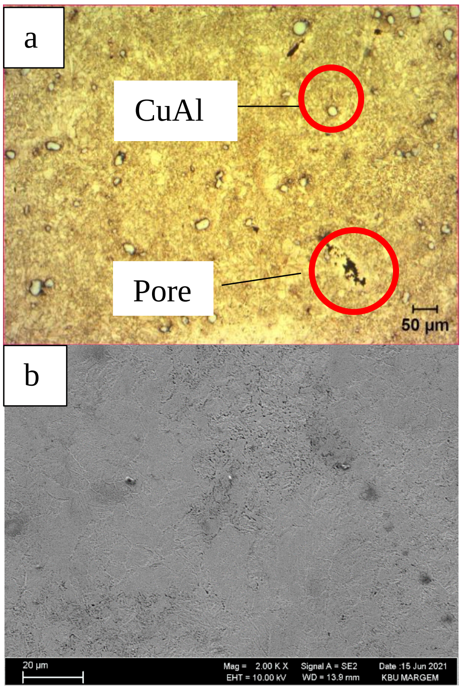

Fig. 2. Pure CuAlNi alloy a) Optical microscope and b) SEM images

The CuAlNi matrix structure is clearly seen from the optical microscope and SEM image in Figure 2. Partially cracks and pores may be observed due to the powder metallurgy production method in the samples produced.

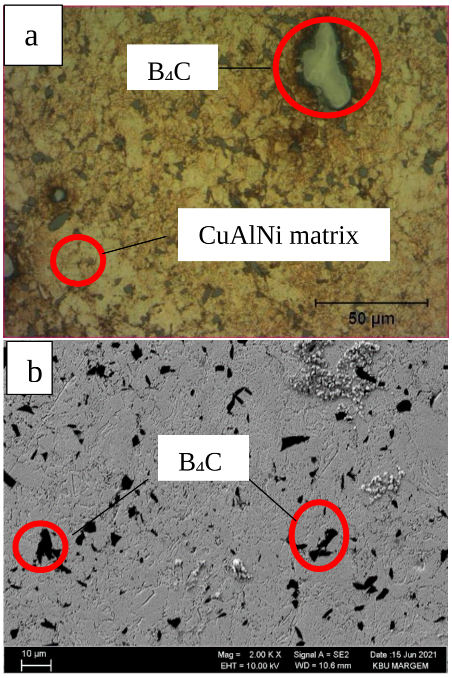

Fig. 3. CuAlNi reinforced with 2,5% B_4C composite a) Optical microscope and b) SEM images

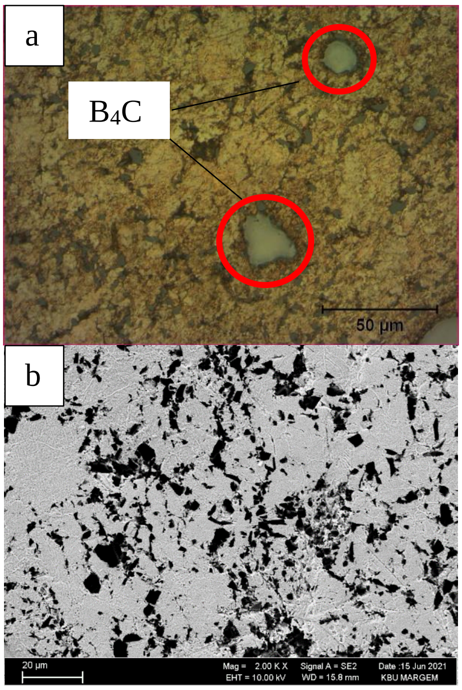

Fig. 4. CuAlNi reinforced with 5% B_4C composite a) Optical microscope and b) SEM images

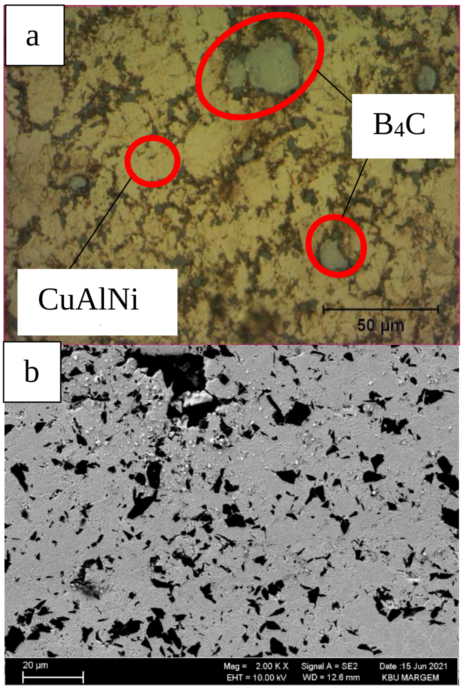

Fig. 5. CuAlNi reinforced with 7,5% B_4C composite a) Optical microscope and b) SEM images

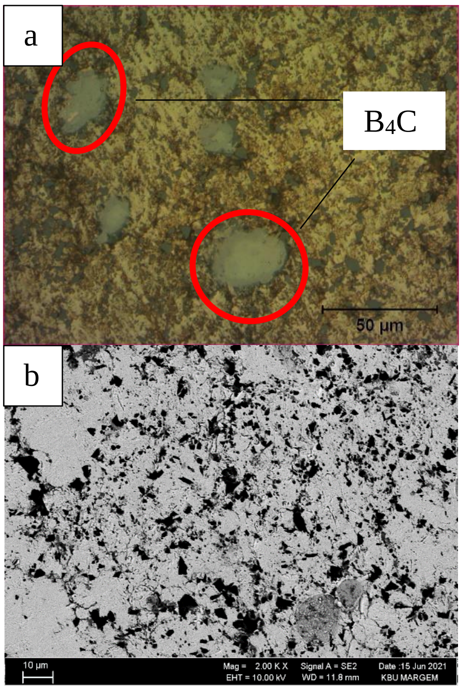

Fig. 6. CuAlNi reinforced with 10% B_4C composite a) Optical microscope and b) SEM images

When the given optical microscope and SEM images are examined, it is clearly seen that as the percentage of B_4C in the matrix increases, the amount also increases. It is thought that the homogeneous distribution of CuAlNi and B_4C in the internal structure is caused by 3 dimensional mixer and hot sintering. SEM-EDS analysis results of the samples are shown in Figure 7-11. When the SEM-EDS analysis results of the samples are examined, it is observed that there is no contamination in the composition. The EDS analysis result supports the chemical composition of the produced sample.

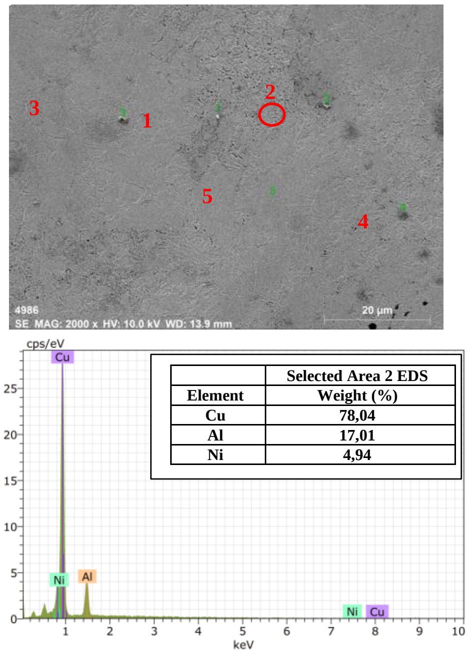

	Selected Area 2 EDS
Element	**Weight (%)**
Cu	**78,04**
Al	**17,01**
Ni	**4,94**

Figure 7. Pure CuAlNi alloy SEM-EDS analysis result

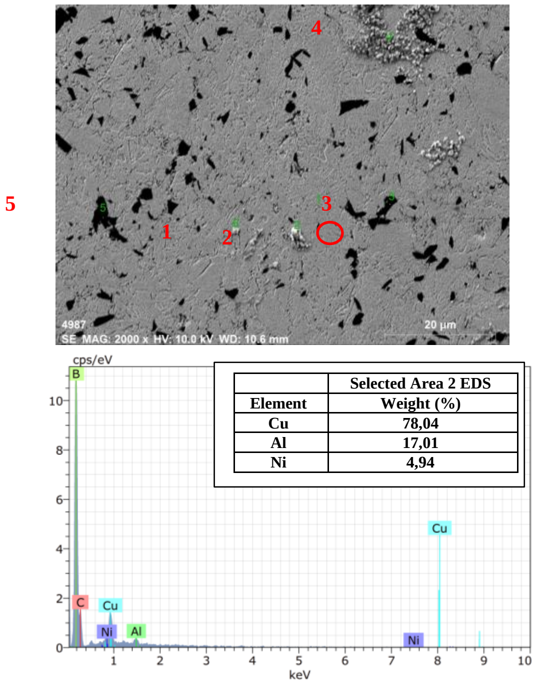

Element	Selected Area 2 EDS Weight (%)
Cu	78,04
Al	17,01
Ni	4,94

Fig. 8. CuAlNi-2,5% B_4C composite SEM-EDS analysis result

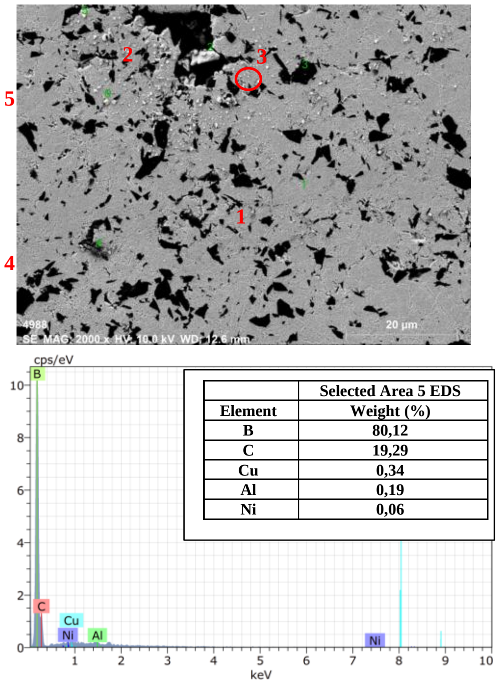

Element	Selected Area 5 EDS Weight (%)
B	80,12
C	19,29
Cu	0,34
Al	0,19
Ni	0,06

Fig. 9. CuAlNi-5% B_4C composite SEM-EDS analysis result

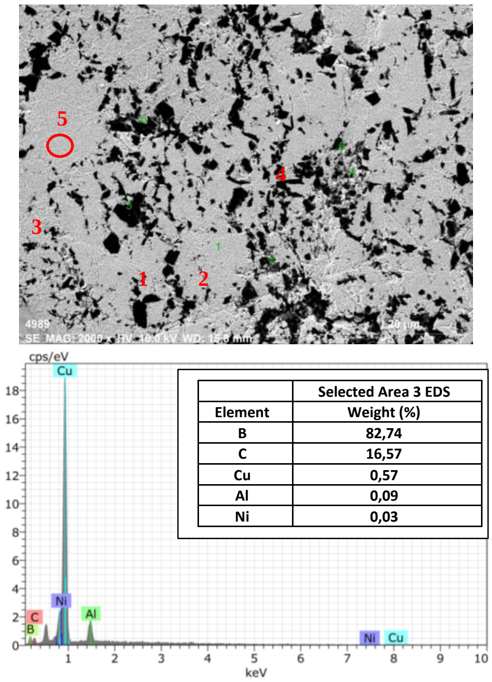

Element	Selected Area 3 EDS Weight (%)
B	82,74
C	16,57
Cu	0,57
Al	0,09
Ni	0,03

Fig. 10. CuAlNi-7,5% B_4C composite SEM-EDS analysis result

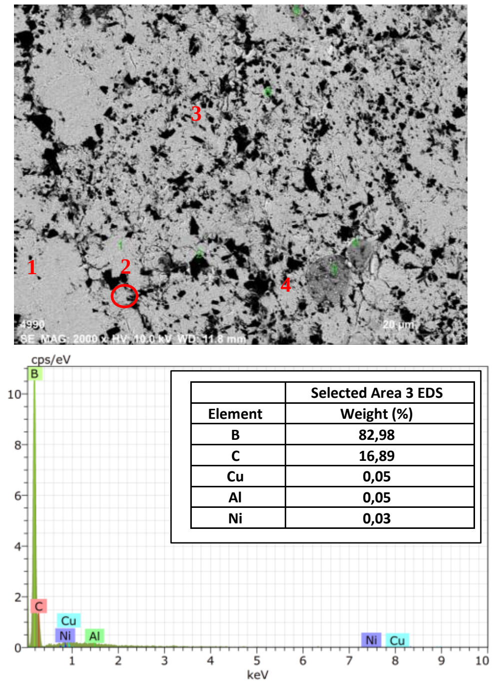

Element	Selected Area 3 EDS Weight (%)
B	82,98
C	16,89
Cu	0,05
Al	0,05
Ni	0,03

Fig. 11. CuAlNi- 10% B_4C composite SEM-EDS analysis result

XRF results of CuAlNi-B_4C reinforced samples produced by the powder metallurgy method are given in Table 1. B_4C could not be detected in the structure, as B and C were difficult elements to detect in XRF analysis, but B_4C was observed in XRD and EDS analyses.

Table1. XRF analysis results

	Cu (%)	Al (%)	Ni (%)	Si (%)	Fe (%)
CuAlNi	67,628	29,123	3,247	-	-
CuAlNi-B4C	62,762	33,383	2,825	0,859	0,171

XRD analysis results of CuAlNi and CuAlNi-B_4C reinforced samples produced by the powder metallurgy method are given in Figure 12.

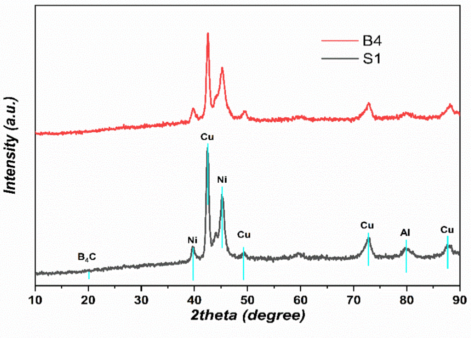

Fig. 12. XRD results

When the XRD graphs given in Figure 12 were examined, it was determined that CuAlNi and similar phases were also formed, as well as B_4C phases. In addition, it is clearly seen that the Cu-Al phase is dominant. During the sintering process, Cu_4Al, Cu_9Al_{44}, Cu_3Al intermetallic phases were formed between CuAlNi and B_4C particles. In general, when the given XRD graphs were examined, it was determined that the intensity of the formed intermetallic phases increased as the amount of B_4C increased.

Microhardness Analysis

The microhardness graphs of the samples are shown in Figure 13. Microhardness measurements of the produced samples were taken from the sample surface along a line at 100 µm intervals.

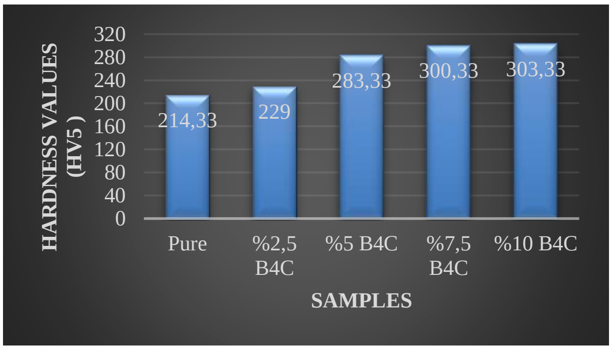

Fig. 13. The microhardness of the samples

CuAlNi produced by the method of powder metallurgy, and %2,5, %5, %7,5, %10 Micro hardness graphs of B_4C reinforced CuAlNi samples are given in Figure 5.11. Microhardness measurements of the produced samples were taken from the sample surface along a line at 100 µm intervals. The hardness of the CuAlNi sample, which we define as pure, is on average 214 hv5. The hardness values of the samples reinforced with 2.5% B_4C, 5% B_4C, 7.5% B_4C and 10% B_4C were determined as 229 HV_5, 283.3 HV_5, 300.3 HV_5 and 303.3 HV_5, respectively. The hardness of B_4C reinforced samples is higher than that of non-reinforced sample. This increase is associated with the presence of carbide, which increases by % in volume, and the resulting hard phases.

Wear Analysis

The graph of the wear results of CuAlNi and 5% and 10% B_4C reinforced CuAlNi samples produced by powder metallurgy method by applying 20 and 40 N loads is given in Figure 5.12. Parameters such as sliding speed, applied load, sliding distance and reinforcement element ratio are effective on the wear behavior of composite materials. In the abrasion tests AISI 52100 ball with 6 mm diameter and 62 HRC hardness was used as abrasive material.

Table 2. Wear analysis results

	Wear Depth (mm)	Wear Volume Loss (mm^3)	Wear Rate (mm^3/m)
CuNiAl-20N	0,14	1,12	0,00448
%5B_4C-20N	0,085	0,885	0,00354
%10B_4C-20N	0,03	0,65	0,0026
CuNiAl-40N	0,18	1,77	0,00708
%5B_4C-40N	0,1385	1,305	0,00522
%10B_4C-40N	0,097	0,84	0,00336

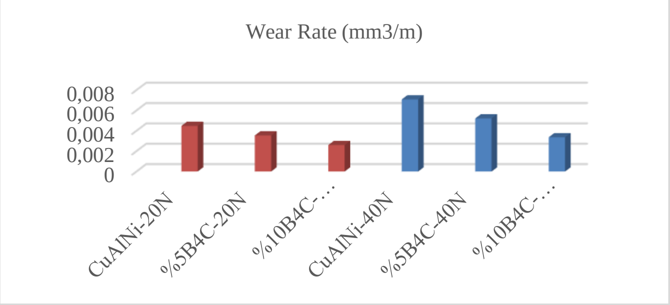

Fig. 14 The wear rates of the samples

When the wear results were examined, it was observed that the wear rates of B4C reinforced composites were lower than that of pure CuAlNi composite. The hardness value of boron carbide is higher than other elements (Cu, Al, Ni) in the composite. Looking at the microhardness results, the hardness values of 5% and 10% B4C reinforced composites were measured as 283 HV5 and 303 HV5, respectively. When the wear rate results are examined, it is seen that the samples with high hardness value are more resistant to abrasion. When the wear graph is examined, it is seen that the wear rates increase in direct proportion to the increasing load. As a result of the literature review, it is known that the relationship between hardness and wear resistance is directly proportional.

Conclusion

In this study, CuAlNi and CuAlNi-B4C composites were successfully produced by powder metallurgy (TM) method. Optical microscope, scanning electron microscope (SEM-EDS), X-ray diffractogram (XRD), X-ray fluorescence (XRF) microhardness test and wear test were successfully applied to the produced samples. The report of the experimental results can be summarized as follows.

In this study, CuAlNi and CuAlNi-B4C composites were successfully produced by powder metallurgy (TM) method. Optical microscope, scanning electron microscope (SEM-EDS), X-ray diffractogram (XRD), X-ray fluorescence (XRF) microhardness test and wear test were successfully applied to the produced samples. The report of the experimental results can be summarized as follows.

- It has been reported that the B4C particles are uniformly distributed in the optical microscope and SEM images taken from the samples.

- In the EDS analysis results, the chemical compositions of the produced samples were supported and FR was found that there are different ratios of Cu, Al, Ni, B and C in the internal structures of the samples.

- When the XRD graph was examined, peaks belonging to Cu, Al, Ni, B_4C and Cu_4Al, Cu_9Al_{44}, Cu_3Al intermetallics were detected.

- As a result of the microhardness test, it was found that the hardness of B_4C reinforced samples was higher than that of the non-reinforced sample. There has been an increase in hardness values due to the increased amount of B_4C. The best microhardness value was measured as 303.3 HV_5 in the sample to which 10% B_4C was added.

- In the wear analysis results, it was found that the wear rate of a 10% B_4C reinforced sample was less than that of non-reinforced and 5% reinforced sample. There has been a decrease in the wear rate values due to the increased amount of B_4C. Considering the results of micro-hardness, the hardness values of 5% and 10% B_4C reinforced composites were measured as 283 HV_5 and 303 HV_5, respectively. As a result of literature reviews, it is known that the relationship between hardness and wear resistance is directly proportional.

REFERENCES

[1] Azaath, L. M., Natarajan, U., Veerappan, G., Ravichandran, M., & Marichamy, S. (2021). Experimental Investigations on the Mechanical Properties, Microstructure and Corrosion Effect of Cu-20Al-4Ni/SiC Composites Synthesized Using Powder metallurgy Route. Silicon, 1-10. https://doi.org/10.1007/s12633-021-01363-2.

[2] Seo Y, Kang C (1999) Effects of hot extrusion through a curved die on the mechanical properties of SiCp/Al composites fabricated by melt-stirring. Combust Sci Technol 59(5):643–654. https://doi.org/10.1016/s0266-3538(98)00123-7.

[3] Xu Y, Chung DDL (1998) Low-volume-fraction particulate preforms for making metal-matrix composites by liquid metal infiltration. J Mater Sci 33:4707–4709. https://doi.org/10.1023/A:1004480819365,

[4] Seo YH, Kang CG (1995) The effect of applied pressure on particle-dispersion characteristics and mechanical properties in melt-stirring squeeze-cast SiCp/Al composites. J Mater Process Technol 55(3–4):370–379. https://doi.org/10.1016/0924-0136(95)02033-0.

[5] Recarte, V., Perez-Landazabal, J. I., Rodrıguez, P. P., Bocanegra, E. H., No, M. L. and San Juan, J., "Thermodinamics of thermally ınduced martensitic transformations in Cu-Al-Ni shape memory alloys", Acta Materialia, 52: 3941-3948 (2004).

[6] Taulor, P. M., Moser, A. and Creed, A., "A sixty-four element tactile display using shape memory alloy wires", Displays, 18: 163-168. (1998).

[7] Izadi H, Nolting A, Munro C, Bishop D, Plucknett K, Gerlich A (2013) Friction stir processing of Al/SiC composites fabricated by powder metallurgy. J Mater Process Technol 213(11):1900–1907. https://doi.org/10.1016/j.jmatprotec.2013.05.012.

[8] Cavdar U, Atik E, Akgul MB (2014) Magnetic-thermal analysis and rapid consolidation of FE–3 wt.%CUpowder metal compacts sintered by medium-frequency induction-heated system. Powder Metall Met Ceram 53(3–4):191–198. https://doi.org/10.1007/s11106-014-9603-5,

[9] Wang, W., Guo, E., Chen, Z., Kang, H., Chen, Z., Zou, C., ... and Wang, T., "Correlation between microstructures and mechanical properties of cryorolled CuNiSi alloys with Cr and Zr alloying", Materials Characterization, 144: 532-546 (2018).

[10] Lei, Q., Li, S., Zhu, J., Xiao, Z., Zhang, F., and Li, Z., "Microstructural evolution, phase transition, and physics properties of a high strength Cu–Ni–Si–Al Alloy", Materials Characterization, 147: 315-323 (2019).

[11] Kim, H., Ahn, J. H., Han, S. Z., Jo, J., Baik, H., Han, H. N., and Kim, M., "Microstructural characterization of cold-drawn Cu-Ni-Si alloy having high strength and high conductivity", Social Science Research Network, (2019).

[12] Gholami, M., Vesely, J., Altenberger, I., Kuhn, H. A., Janecek, M., Wollmann, M., and Wagner, L. "Effects of microstructure on mechanical properties of CuNiSi alloys", Journal of Alloys and Compounds, 696: 201-212 (2017)

[13] Lei, Q., Li, Z., Wang, M. P., Zhang, L., Gong, S., Xiao, Z., and Pan, Z. Y., "Phase transformations behavior in a Cu–8.0 Ni–1.8 Si Alloy", Journal of alloys and compounds, 509(8): 3617-3622 (2011).

[14] Semboshi, S., Sato, S., Iwase, A., and Takasugi, T. "Discontinuous precipitates in age-hardening CuNiSi alloys", Materials Characterization, 115: 39-45 (2016).

[15] Atapek, Ş. H., Pantelakis, S., Polat, Ş., Chamos, A., and Çelik, G. A., "Fatigue behavior of precipitation strengthened Cu–Ni–Si alloy modified by Cr and Zr addition" International Journal of Structural Integrity, (2020).

[16] Wu, R., Zhou, K., Yang, Z., Qian, X., Wei, J., Liu, L., ... and Wang, L., "Molten-salt-mediated synthesis of SiC nanowires for microwave absorption applications", CrystEngComm, 15(3): 570-576, (2013).

[17] Dash, A., Sohn, Y. J., Vaßen, R., Guillon, O., and Gonzalez-Julian, J., "Synthesis of Ti3SiC2 MAX phase powder by a molten salt shielded synthesis (MS3) method in air", Journal of the European Ceramic Society, 39(13): 3651-3659, (2019).

Theoretical modelling of the Mg-Dia interface with nitride compounds for high thermal conductivity

Safa Polat*, Muwafaq Mashrah+

+ Materials Research and Development Centre, Karabuk University, Turkey

+ Department of Metallurgy and Materials, Karabuk University, Turkey

safapolat@karabuk.edu.tr, mashrahmuwafaq8@gmail.com

***Abstract*—** High thermal conductivity (TC) materials are needed in electronic devices developed in recent years. For this purpose, traditional metal alloys such as copper, aluminium and magnesium and synthetic diamond particles with very high thermal conductivity (1800 W/mK) are widely used. However, poor wettability between diamond and metals poses a significant problem. So, it is necessary to experiment by adding different components at the interface, which is a disadvantage in terms of time and cost. However, in this context, TC values of such composites can be examined theoretically with accepted models. In this study, the presence of nitride compounds of different thicknesses at the magnesium and diamond interface was investigated. Acoustic mismatch model (AMM), extended diffusion mismatch model (DMM) and differential effect medium scheme (DEM) were used to calculate the TC value of the composites. While AlN, Si_3N_4 and TiN are used as interface components, their thicknesses were adjusted to increase from 10 nm to 2000 nm. According to the calculated results, while the TC value of Mg-Dia was expected to be 488 W/mK if there was no interfacial wettability problem, it was calculated that AlN, Si_3N_4 and TiN would be 516, 515 and 517 W/mK, respectively, at 10 nm thickness. However, when the thickness of these components increased to 250 nm, the TC values decreased to 501, 440, and 474 W/mK, respectively. The component that was least affected by the thickness increase was determined as AlN and could remain above the Mg-Dia TC limit up to about 500 nm. For this reason, for the Mg-Dia interface, if the interface thickness can be controlled, Si_3N_4 and TiN can be used, but if the thickness sensitivity cannot be achieved, the use of AlN can be recommended.

***Keywords*— Diamond, Magnesium, Nitrides, Thermal conductivity**

INVESTIGATION OF HYDROXYAPATITE COATED MAGNESIUM AND TITANIUM ALLOYS BY SOL-GEL METHOD

Ece DURAN[1], Hasan DURMAZ[1], Esma KESKİN[1], Bengü AKIN[1], Hayreddin BOZTAŞ[1], Aysun IŞIKGÜL[2], Hayrettin AHLATCI[1], İsmail ESEN[1], Yunus TÜREN[1]

[1] Karabuk University, Faculty of Engineering, Metallurgical and Materials Engineering

[2] Kardemir A.Ş., R&D Center

Abstract— In recent years, it has been aimed to prevent increasing environmental pollution by using limited energy resources efficiently and to provide an economic advantage in sectors such as production, labor and transportation. In the studies carried out for this purpose; It is seen that light metals (Al, Ti, Mg) with a wide range of use are used. The main reason why light metals and their alloys are so popular can be defined as their very good mechanical properties, good castability, easy processing, possible recovery and ease of use. However, with these advantages, the low corrosion and wear resistance of light metals and alloys limit the life of the parts. In order to make this disadvantage more innovative, different coating methods are applied to the surface. Sol-gel, which is one of the most effective and advanced technology coating methods, enables the production of thin films consisting of a wide variety of organic, inorganic, hybrid and nanocomposite materials developed in the 1800s. Among the reasons why this process is preferred, there are low cost, ease of processing, low application temperature, high purity of the product, physical and chemical homogeneity, submicron thickness, controllability of the composition and enabling the coating of all complex shaped substrates. Due to these advantages, it is superior to conventional coating methods. In this method, the solution is prepared and then the solvent in the gelled solution is removed from the system and glass-ceramic, ceramic, glass or composite materials can be produced. The general steps of the method are described as gel formation, aging, drying and sintering. Hydroxyapatite (HA) coating material is widely used for repairing bone defects and improving the coating for the use of dental and orthopedic implants. Hydroxyapatite (HA, (Ca10(PO4)6(OH)2) is a calcium phosphate found naturally in bones and teeth, mainly containing calcium (Ca) and phosphorus (P) elements in a stoichiometric ratio of 1.67. AZ91, Ti6Al4V, Mg and Ti are among the light metals and alloys used in bone, dental and orthopedic implant applications and whose properties have been improved by the sol-gel coating method. The decrease in the corrosion rate of AZ91 alloy coated with Hydroxyapatite with the sol-gel method is based on the decrease in the distance between cracks and the crack area with the increase in the coating thickness of the cracks formed during the coating. The deterioration of the corrosion resistance of materials with Hydroxyapatite (HAP) coating was found to depend on the pH value of the solution, the composition of the Ringer solution (high Cl content and absence of phosphate and carbonate ions), and low HAP layer thickness.

Keywords— AZ91, Ti6Al4V, Ti, Mg, Sol-gel, Hydroxyapatite (HAP), Corrosion.